Chapter 1
Introduction to Laser Micro-to-Nano Manufacturing

Anming Hu, Ruozhou Li, Shi Bai, Yongchao Yu, Weiping Zhou, Denzel Bridges, Yangbao Deng, and Lingyue Zhang

Abstract Laser-based micro-to-nanomanufacturing becomes attractive in surface engineering, precising machining and 2D and 3D microprinting. This chapter introduces the fundamental of light-nanomaterial interaction, the size effect and scaling of nanomaterials and the surface plasmonic excitation of nanomaterials. We focus on the unique features of energy and mass transporting at a nanoscale under photonic excitation. For photonic manufacturing, we mainly compare the photothermal effect induced by long pulse (long than 1 picosecond) or continue wave laser to the nonthermal effect induced by an ultrafast pulsed laser (shorter than 1 picoseconds). We review various laser-based processing, such as, photonic reduction, sintering, laser direct writing and laser carbonization. Subsequently we reviewed two kinds of key techniques for micro-to-nanomanufacturing: various micro-to-nano manipulations and nanojoining. On the basis of these reviews, we introduce latest progresses on innovative molecular devices, near-field manufacturing and super-resolution manufacturing.

A. Hu (✉) · Y. Yu · D. Bridges · L. Zhang
Department of Mechanical, Aerospace and Biomedical Engineering, University of Tennessee Knoxville, 1512 Middle Drive, Knoxville, TN 37996, USA
e-mail: a2hu@uwaterloo.ca

R. Li
College of Electronic and Optical Engineering & College Microelectronics, Nanjing University of Post and Telecommunications, Nanjing 210023, China

S. Bai
Advanced Laser Processing Research Team, RIKEN Center for Advanced Photonics, RIKEN, 2-1 Hirosawa, Wako, Saitama 351-0198, Japan

W. Zhou
School of Physics and Electronic Science, Hunan University of Science and Technology, Xiang'tan 411201, China

Y. Deng
All-Solid-State Energy Storage Materials and Devices Key Laboratory of Hunan Province, College of Information and Electronic Engineering, Hunan City University, Yiyang 413000, China

A. Hu (ed.), *Laser Micro-Nano-Manufacturing and 3D Microprinting*, Springer Series in Materials Science 309, https://doi.org/10.1007/978-3-030-59313-1_1

1.1 Introduction

Laser has become a powerful and versatile tool for manufacturing various mechanical, energy, optoelectronic and biomedical devices with a precision down to a micro- and nano-size [1–3]. To enable a precise engineering and manufacturing it is a linchpin to understand the fundamentals of laser-matter interaction, specially at a small scale [4–6]. Due to the scaling law and the size effect, many materials will behave quite different from their bulk counterparts. Meanwhile, the principles of micro-optics and nanophotonics, which govern the propagation and further manipulation of light and laser (i.e., high single color, extremely strong and aligned light) and the optics at a macro scale are fundamentally disparate. This point has to be considered for micro-to-nano manufacturing. Due to the blooming development of both nanotechnology and nanophotonics, micro- and nanomanufacturing based on laser technology is demonstrating the bright perspective for the extensive application in emerging consumable electronics, flexible, portable and wearable electronics, big data, Internet of things (IoTs).

Traditionally, a pulse period shorter than a nanosecond (10^{-9} s) is named as ultrafast laser. Since the invention of chirped pulse amplification, femtosecond (10^{-15} s) lased laser has attracted extensive interests for precision machining [7]. It has found that limited heating diffusion on the surrounding region of the processed area is one of pronounced features of ultrafast laser processing [8, 9]. By employing a femtosecond ultraviolet laser, polymethyl methacrylate was ablated without the formation of a heat-affect zone [10, 11]. Comparing to the ablation with a nanosecond pulsed laser, the ablation threshold using a femtosecond and or a picosecond laser was also reduced significantly. These features encourage the high-precision manufacturing using various materials, such as biological tissues, semiconductors and other dialectical materials [12]. For an ultrafast interaction, the absorption of photons stimulates the carriers within hundred femtoseconds (fs), which is too short to disturb lattice since the electron-phonon coupling typically occurs in range of 1-100 ps [13, 14]. Meanwhile, an ultrafast pulse width is less than 1 ps. Thus, in an ideal case, ultrafast excitation only occurs within the focal spot. However, for a laser pulse with duration of nanoseconds or longer, the thermal diffusion cannot be neglectable [15]. On the other hand, the nonlinear multiphoton absorption is another important aspect of ultrafast laser processing. The probability of multiphoton absorption can be significantly increased with the extremely high laser peak intensity of tightly focused ultrashort laser pulses since the probability is a power function of the peak intensity [16, 17]. The highly localized nonlinear effect of ultrashort laser may lead to a super-resolution processing beyond the optical diffraction limit and thereby strong absorption can even occur in a transparent material [18, 19]. This multiphoton absorption of ultrafast laser not only permits the surface processing, but also permits the internal microfabrication of transparent materials, such as glass and polymer [20, 21]. Due to the unique multiphoton excitation and the aforementioned highly localized thermal processing, ultrafast laser is found unprecedent application for precise micro-to-nanomanufacturing.

This chapter is organized as follows: starting from the absorption, ionization and surface plasmonic excitation we will briefly review the fundamentals of laser-matter interaction based on a electron-hole plasma frame. We will specially discuss the differences of two kinds of laser, ultrafast pulsed laser and long pulsed or continuous-wave laser interacting with a dielectric material and metal. Based on these physical pictures, we will introduce unique electromagnetic properties of nanomaterials through the scaling law, and then we will briefly overview nanophotonics and plasmonics. In the Sect. 1.4, we will focus on the unique thermal and nonthermal phenomena dominantly induced by long laser pulses and short pulses, separately. In the following two sections, we can review two key fields for micro-to-nanomanufacturing, i.e., nanomanipulation and nanojoining. At last, we will review the latest progress on the nanomanufacturing overcoming the optical diffraction limit.

1.2 Laser-Matter Interaction: Absorption and Ionization

Light-matter interaction is based on the photonic energy is reflected (and/or scattered) by the surface and the absorption of molecules. According to the Lambert-Beer law, the transmittance T can be expressed as (1.1.1)

$$T = I/I_0 = e^{-\alpha x} \tag{1.1.1}$$

where, x is the width of media, I_0, I and I' stand for incident, transmitted and reflected light intensities, respectively. Thus, the interaction only happens in the surface layer (the penetration layer) $L \sim 1/\alpha$ for a non-transparent material. Figure 1.1 shows a light transmitting material with absorption coefficient, α. For graphite, this depth is about 30 nm for 620 nm light [22]. For aluminum, the penetration depth is about 15 nm at 308 nm [23] (Palik 1985). The conventional absorption spectroscopy measures the absorbance $A = Ln(I_0/I) = \alpha x$.

The primary laser-matter interaction process thus involves the excitation of electrons from their equilibrium states to higher energy levels by photo-absorption. Since the light is an electromagnetic wave, the physics of interaction can be described in a better picture by electromagnetic theory. We suppose that a material fills half-space at $x > 0$, overlapped by the skin depth (optical penetration depth) $l = \frac{c}{\omega\kappa}$, where k is the imaginary part of the refractive index and ω the light frequency. At a low laser

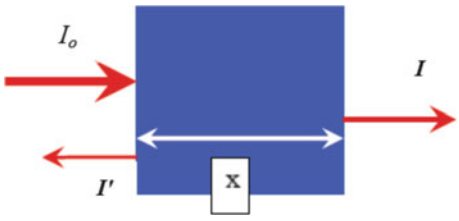

Fig. 1.1 Absorption, transmission and reflection in a planar sample

power (i.e., the laser power lower than the ablation threshold) for a visible to infrared light (at this band, the intra-band absorption can be neglect. For a ultraviolet wavelength, the Loranz-Drude approximation is needed [24, 25] for electron excitation due to the intra-band absorption), the material state can be described by a dielectric function in the Drude approximation

$$\varepsilon = 1 - n_e \frac{\langle \sigma \rangle}{\omega}(i + \omega\tau_m) = 1 - \frac{\omega^2 p_e}{\omega(\omega + i v_m)}$$
$$\varepsilon^{1/2} = n + ik \tag{1.1.2}$$

Here n_e is the electron density, ω_{pe} is the frequency of electron plasma under excitation, $\omega_{pe} = (4\pi e^2 n_e/m)^{1/2}$, v_m is an effective collision frequency of electrons with the lattice (ions). The corresponding absorbance, reflection coefficient, and transmittance, A, R, and T, are given by

$$R = \left|\frac{1 - \sqrt{\varepsilon}}{1 + \sqrt{\varepsilon}}\right| = \frac{4\mathrm{Re}\sqrt{\varepsilon}}{\left|1 + \sqrt{\varepsilon}\right|^2}$$
$$T = \left|\frac{2\mathrm{Re}\sqrt{\omega}}{1 + \sqrt{\omega}}\right|$$

and $A = 1 - R \approx 4\mathrm{Re}\left(\frac{\sqrt{\varepsilon}}{|\varepsilon|}\right) \approx 2\frac{v}{\omega}\left(\frac{n_e}{n_e}\right)^{1/2}$ here $n_e = \pi mc^2/(e^2\lambda^2)$ is the critical density.

We will further consider the surface plasmonic excitation (ω_{pe}) in details in the Sect. 1.3.2. Here, let us first consider photonic-induced ionization at a short light wavelength or a high laser power. For a conventional photoelectron effect, the electron energy is linear dependent on the photonic energy when the photonic energy is higher than a threshold potential. For a transparent dielectric material, there is limited absorption when the photon energy is smaller than the energy gap E_g of dielectric material. Nonlinear absorption mechanism allows photonic-induced ionization. According to the laser intensity and the wavelength, there are three mechanisms for ionization, i.e., tunneling ionization [26], multiphoton ionization [27] and avalanche ionization induced by inverse Bremsstrahlung [28]. Shown in Fig. 1.2, the boundary for the first two cases is described by the Kelddysh parameter [29].

$$\gamma = \frac{\omega}{e}\sqrt{\frac{m_e c n \varepsilon_0 E_g}{I}} \tag{1.1.3}$$

where e is the electron charge, m_e is the effective electron mass and c is the light velocity. When the laser intensity is high and thereby lowers the potential barrier while at a low photon energy (light frequency is low) the electron can pass through the potential barrier through quantum tunneling. As the laser wavelength is short, the electron is more easily excited through a multiphoton absorption. The study displayed that $\boldsymbol{\gamma} \ll 1$, a tunnel ionization is dominant meanwhile the multiphoton absorption

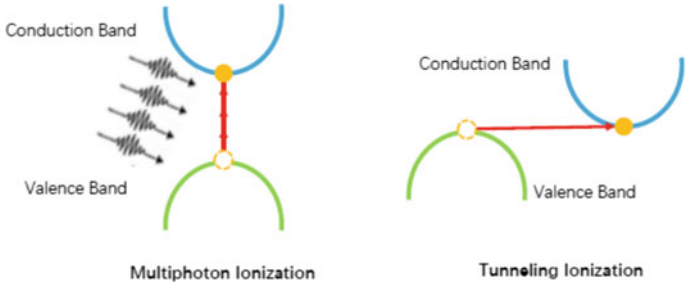

Fig. 1.2 Multiphoton ionization and tunneling ionization

is governed at $\boldsymbol{\gamma} \gg 1$. When $\boldsymbol{\gamma}$ is approximated near 1, two mechanisms may occur simultaneously [29]. Besides, the non-resonant nth order multiphoton ionization rate [30] is

$$P_i = \sigma_n \left(\frac{I}{\hbar\omega} \right)^n \tag{1.1.4}$$

where σ_n is the generalized nth order cross section and I is the peak laser intensity. Therefore, at a long light wavelength, the multiphoton ionization rate can be improved at an extremely high laser intensity.

Electrons at the conduction band can also absorb photon energy through an inverse Bremsstrahlung. When the electrons are enough hot (the kinetic energy is higher the energy gap), they can excite the electrons from the valent band to the conductive band through impaction and then generate two free electrons at the bottom of conductive band (Fig. 1.3). If the intensive laser field constant presents, this excitation of the initial electrons will be repeated and result in a large amount of free electrons. This impact-induced ionization is called the avalanche ionization [31]. And the initial

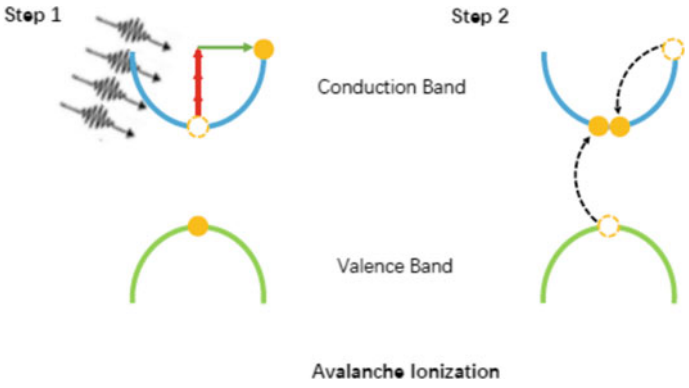

Fig. 1.3 Avalanche ionization through inverse Bremsstrahlung excitation

excited electrons can originate from the thermal excitation of impurity and/or from tunneling and multiphoton ionization. The avalanche ionization causes the significant increase of free electron density. Meanwhile, the laser heat enhances the plasma frequency ω_{pe} approaching the laser frequency. This subsequently yields a stronger resonant absorption and improves the free electron density to a critical value $n_e = \pi mc^2/(e^2\lambda^2)(\sim 10^{22}\ \mathrm{cm}^3)$.

For a practical photonic excitation with a high laser power, these ionizations may synergically exist. For example, with a 100 fs pulse excitation, multiphoton ionization creates a substantial amount of free electrons. When the electron density approaches $10^{17}\ \mathrm{cm}^{-3}$, the collisional ionization rate begins to exceed the multiphoton ionization rate [31]. When this electron density approaches $10^{22}\ \mathrm{cm}^{-3}$, a critical electron density, the reflectivity dramatically increases [32]. The maximum density was thus limited to $10^{22}\ \mathrm{cm}^{-3}$, which corresponds to approximately 10% of the total valence-band population [32].

A lattice softening has been theoretically expected when 10% of the valence electrons are excited into the conduction band [33, 34]. This lattice softening eventually leads to lattice melting, as predicted by ab initio molecular-dynamic calculation [35, 36] and observed experimentally by time-resolved reflectivity [37]. Such melting is an ultrafast phenomenon and is not a consequence of conventional thermal heat transfer.

1.3 Laser-Nanomaterial Interaction

1.3.1 Scaling Law

Nanomanufacturing is further based on the laser-nanomaterials interaction. When the size decreases from a macroscale to a nanoscale, some negligible properties at a macroscopic world become dominant. Although some macroscopic principles are still valid at a microsize, nanomaterials behave very unique. Specially, the quantum effect is critical at an interatomic range or very close to the surface, i.e., within a few nanometers distance. At this size range, a tiny nanoparticle is conventionally named as a quantum dot. The scaling law is a useful method to observe nanoworld based on our knowledge of the macroworld. The scaling law displaying the relation between physical quantities, allows to investigate physical principles and variations in the macro-, micro- and nanoworlds [38].

Size-Effect For a solid material, it is well known that surface atoms have fewer bonds than internal atoms. Less energy is thus needed for them to leave the surface. Considering n balls with an even diameter of R closely compacted in a 2D plane, it is easily to calculated that the total volume is $4n/3\mathrm{R}^3$, while the surface area is $n\,R^2$. The surface/volume ratio is $3/(4R)$, which will significantly increases when R decreases. For a rough estimation, there are about 0.3% atoms presented at the surface for a 1 Â µm particle. However, 87.5% atoms will occupy the surface state in a 2 nm

particle! According to thermodynamics estimation, a large surface/volume leads to a size depression effect of the particle melting temperature [39, 40]. Accordingly to classical Gibbs-Thomson equation, the melting point of particles ($T_m(d)$) can be expressed as follows [41]

$$T_m(d) = T(\infty)\left(1 - \frac{4\sigma_{sl}}{H_f \rho_s d}\right) \tag{1.1.5}$$

where d stands for the particle diameter, $T(\infty)$ is the bulk melting point, σ_{sl} is the solid-liquid interface energy, H_f is the bulk heat of fusion, ρ_s density of solid and d is the particle size. In a practical situation, particle surfaces have a high concentration of defects [40]. As a result, the surface atomic mobility is higher than the inner atoms. Nanoparticles can even demonstrate more activated behaviors at a temperature lower than its melting temperatures. Shi et al. indiced a surface melting model to describe the thermal stability of nanoparticles and/or a 2D system [42],

$$T_m(d) = T_m(\infty)\exp\left[-\frac{\alpha - 1}{\frac{d}{3h} - 1}\right] \tag{1.1.6}$$

where h is the monolayer height of the surface atoms, r is the particle diameter, α is a material constant, relevant to the surface vibration energy. Considering a surface diffusion is a thermally activated, thus $D(d, T)$ can be written in the Arrhenius law

$$D(d, T) = D_o(d)\exp\left[-\frac{E(d)}{RT}\right] \tag{1.1.7}$$

where D_0 is the intrinsic diffusion coefficient, R is the ideal gas constant. $E(d)$ is the diffusion barrier. Assuming $D_0(d) \sim D_0(\infty)$ and

$$\frac{E(d)}{E(\infty)} \approx \frac{T_m(d)}{T_m(\infty)}$$

Combining with the Arrhenius law, one can obtain the thermally activated diffusion coefficient as a function of particle diameter [43]

$$D(d, T) = D_0(d)\exp\left[-\frac{E(\infty)}{RT}\exp\left[-\frac{\alpha - 1}{\frac{d}{3h} - 1}\right]\right] \tag{1.1.8}$$

This indicates the diffusion is remarkably enhanced at a nanoscale. Equations (1.1.5) and (1.1.8) will significantly influence the nanomanufacturing. In brief, (1.1.5) indicates a the nanomanufacturing does not require a high energy. For example, compared to a welding at the macroscale is a Kilo Joule to Mega Joule procedure, a nanojoining only needs a nanojoule energy [44]. Soldering or even brazing at a nanoscale can be even realize by a innovative self-heating procedure

Table 1.1 Displays the typical forces as a scale of L [50]

Force type	Scaling
Surface tension	l^1
Electrostatic force	l^2
Fluid force	l^2
Weight/inertia	l^3
Electromagnetic force (for constant current density)	l^4
Van de Waal's force	l^1

[44–46]. Equation (1.1.8) further indicates numerical involving mass transporting occurs at a lower temperature, even at a room temperature [47]. Therefore, it is understood that a joining of nanowire does not need any heat at room temperature [47, 48]. Furthermore, (1.1.8) demonstrates the nanomanufacturing is a surface engineering with a size range less than 100 nm [5, 6, 16]. It is notable that compared to (1.1.5) successfully explain lots of experiment, (1.1.8) has not well established by experimentally investigation [49].

Scaling Laws of Mechanics Let us consider mechanical properties varying with a typical linear dimension L. It is obvious that the geometric area S is proportional to L^2 and the volume V varies with L^3. For a weight which is dependent on the volume, thus the weight varies with L^3. The buoyancy force is dependent on the surface and proportional to L^2. The S/V is 10^{-4}/mm for an elephant while this value is 10^{-1}/mm for a dragonfly. This can explain why the dragonfly can fly while an elephant cannot (Table 1.1).

This scaling behavior will significantly influence the nanomanufacturing. It is well known that robotic arms are extensively used in a modern automation assembly line. As shown in Fig. 1.4, this operation cannot be realized in a nanomanufacturing since the robotic arm cannot grasp and then release a nanoscale building block. For a nanoparticle, its weight is pretty smaller than the tension force with the surface of robotic arm. This means that once the particle absorbs by the robotic fingers due to the surface it will sticks on the arm. The gravity cannot separate it from the fingers. A robotic manipulation cannot be completed. Thus, a manipulation has to be addressed for nanomanufacturing. We will discuss this in Sect. 1.5.

Scaling Laws of Fluidics are important for inkjet based 3D printing, sensing in liquid and biomedical applications. When a body with a diameter of d falls into a viscous liquid, the friction force and the gravity will make the body falling in a constant velocity, v_c, $v_c = 4\rho g d^2/18\eta d\ v_c$, where η is the viscosity of the liquid and ρ is the density of liquid.

$$v_c \sim L^2$$

$$\tau \sim L^2$$

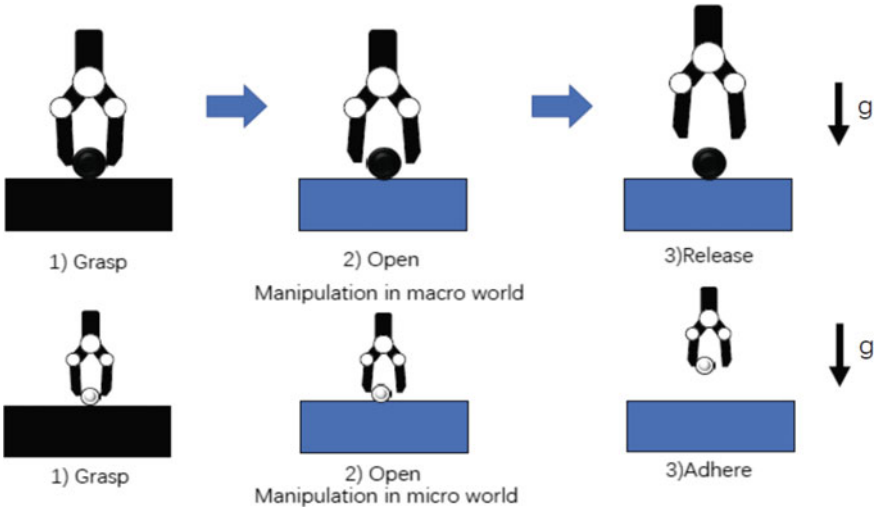

Fig. 1.4 Manipulation difference in a macroworld and a nanoworld

where τ is the transient time. The flux mode can be identified by the Reynold number R_e, $R_e = \rho v L/\eta$. If $v \sim L$, then

$$R_e \sim L^2$$

For a particle travels a distance L by diffusion in a diffusion time $\tau_d = \alpha D$, where α is a geometrical constant and D is the diffusion constant. One can obtain,

$$\tau_d \sim L^2$$

For liquid passes through a needle with a diameter of α, if the needle length is L and the flow rate is Q, the pressure drop through the needle will be

$$\Delta P = \frac{8\mu l Q}{\pi \alpha^4} \sim L^{-3}$$

According this scaling law, for a 30 μm in diameter and 3 cm long needle with a flow rate of 1 microliter per min the pumping pressure is 1.5 atm, but for a 0.3 μm in diameter needle the pumping pressure has to be more than 1.5×10^6 atm!

Scaling Law of Electromagnetics The nanomanufacturing and the operation of nanodevices are frequently involve the electromagnetic properties. Table 1.2 displays the scaling laws of the popular electromagnetic variables.

When the voltage remains constant and L varies, the electrical field E_{el} obviously changes $E_{el} \sim L^{-1}$. The magnetic field intensity in a solenoid with n turns of wire, of the length L, is defined as $B = n\mu I/L$, then $B \sim L$. The magnetic energy stored in the solenoid is

Table 1.2 Scaling laws of electromagnetic variables [51]

Electric quantity	Index, α in L^{α}
Current, I	2
Voltage, V	1
Resistance, R	−1
Capacitance, C	1
Inductance, L	1
Power, P	2

$B_{\text{mag}} = B^2V/2\mu$, V is the volume of the solenoid. One can get

$$B_{\text{mag}} \sim L^5$$

Scaling Laws of Optics are surely critical for laser nanomanufacturing. When light shines on the particle with a length of L, the reflective wave diverges. The divergence angle $\approx \lambda/L$. Hence,

$$\boldsymbol{\theta} \sim L^{-1}$$

This indicates a scattering light will have a very wide solid angle. For photolithography, the optical diffraction limitation with a fixed numerical aperture (NA) lens is

$$d \sim L \approx 2\lambda/(\boldsymbol{\pi}\text{NA}) \tag{1.2.1}$$

Therefore, a shorter wavelength is required for machining a small size of electrical component of integrated circuit chips. For a nanomanufacturing, an electrical ultraviolet (EUV) light source is required for photolithography.

These scaling laws have comprehensive influences of nanophotonic devices and laser-based nanomanufacturing. While microsized optical fibers possess superior performance for telecommunication with reduced lose and band width, submicrosize photonic devices, like, ring-shape resonant cavity, Fabry-Perot laser demonstrate limited quality factors and significant loss. These have to be considered for developing all-optics photonic devices and circuits [52]. In contract, metallic nanomaterials display potential to build plasmonic devices and circuits for light manipulation and confinement at a nanoscale. Through simulation, we have demonstrated several hybrid nanophotonic devices by integrating photonic circuits and plasmonic cavity or boundaries [53–55]. In the following sections we will first discuss how the light excites surface plasmonic resonance on a metallic nanoparticle and then illuminate how the light propagates along an optical fiber and a metallic nanowire. These fundamentals will form the foundation to understand, design and manufacture hybrid nanophotonic-plasmonic devices.

1.3.2 Surface Plasmonic Excitation of Nanoparticles

Surface Plasmons are coherent and collective electron oscillations bounded at the interface between two materials with positive and negative real part of dielectric functions respectively [24]. Fig. 1.5 shows the local electrical filed enhancement due to surface plasmonic excitation. The inherent subwavelength nature of surface plasmons enables significant spatial confinement of light energy and thereby dramatically strengthen the interaction between photons and materials. [56, 57] The enhanced light–matter interactions create fast-developing fields on plasmon-enhanced Raman spectroscopy [58, 59], photocatalysis [60], photothermal [61, 62], photovoltaic [63], fluorescence [64], nonlinear optics [65], etc.

The interaction of plasmonic material with light can be generally regard as the interaction of photons with the free electron gas inside the materials. Over a wide frequency range, the optical properties of plasmonic material can be linked to the well-known Drude approximation [66], where a gas of free electrons of number density moves against a fixed background of positive ion cores [24]. Here, electron-electron interactions and details of the lattice potential are simplified by using the effective mass of the electrons instead, under the hypothesis that the band structure is incorporated into the effective mass in some certain degree. The electrons oscillates with the applied light at an angular frequency ω, and their motion is damped via the relaxation time of the free electron gas τ. The dielectric function of plasmonic material can be write as

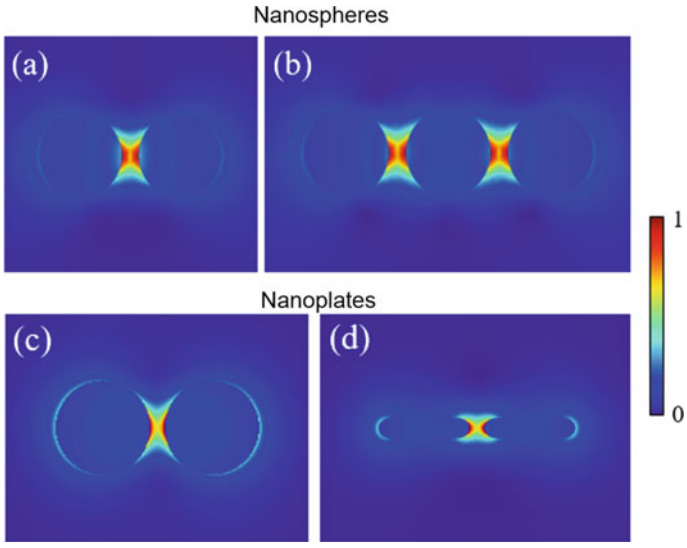

Fig. 1.5 The field distributions of localized surface plasmon resonances (LSPRs) in gold nanospheres and nanoplates

$$\varepsilon(\omega) = 1 - \frac{\omega_p^2}{\omega(\omega + j\gamma\omega)} \tag{1.2.2}$$

where ω_p is the plasma frequency of the free electron gas, $\gamma \sim 1/\tau$ is the impact frequency and τ is the characteristic impacting time.

Clearly the dielectric function of plasmonic material includes a complex form. The real and imaginary components $\varepsilon(\omega) = \varepsilon_r(\omega) + \varepsilon_i(\omega)$ are given by

$$\varepsilon_r(\omega) = 1 - \frac{\omega_p^2\tau^2}{1 + \omega^2\tau^2} \tag{1.2.3}$$

$$\varepsilon_i(\omega) = \frac{\omega_p^2\tau^2}{\omega\left(1 + \omega^2\tau^2\right)} \tag{1.2.4}$$

where the imaginary components of the complex dielectric function implies the attenuation of the lights inside the plasmon materials.

Note that this approximation is not adequate for high angle frequencies, where interband transitions occur [67]. This phenomenon is considerable at visible optical band for noble metals, where photons are efficient in inducing interband transitions [24]. For some of the noble metals such as gold and silver, this effect even occurs at an optical wavelength around 1 μm. The electrons from the filled band below the Fermi surface are excited to higher bands, and ultimately leads to a consequence of an increased damping.

By introducing the complex dielectric function of plasmon material, the interaction of plasmon materials with light can be generally described through classical electromagnetic field theory based on macroscopic Maxwell's equations. This theory is valid even when the spatial scale of the plasmon material is down to several nanometers, though quantum mechanics should be taking into account at sub-nanometer scale reign. In this chapter we limit our description within the realms of the classical theory. However, we have to be open mind for unexpected phenomena with the strong dependence of the properties on frequency and material characteristics.

Surface plasmons can be divided into two categories, i.e., localized surface plasmons (LSPs) and surface plasmon polaritons (SPPs). LSPs are non-propagating excitations of the conduction electrons of plasmonic structures by the light [68]. For metal or some certain kind of semiconductor nanoparticles with dimensions smaller than the incident light wavelength, LSPs can be excited by direct optical excitation. On the other hand, SPPs are electromagnetic excitations propagating at the interface and evanescently confined in the perpendicular direction [69, 70]. With the wavevector matching, SPPs can also be excited and propagated along a metallic nanowire that served as a subwavelength plasmonic waveguide, which is discussed in the next section.

Here, let us consider a small, isolated metal particle with its size comparable to the penetration depth of the incident electromagnetic field into the metal. Therefore the external electromagnetic field can penetrate into the particle and shift the free

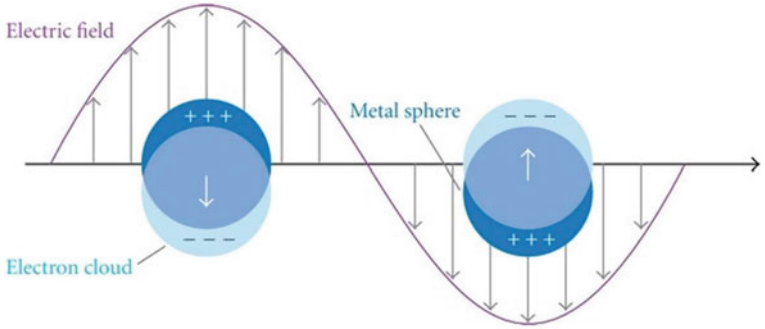

Fig. 1.6 Diagram of localized surface plasmon resonances (LSPRs) (Reprinted with permission from [71]. Copyright 2019. Hindawi Publishing Corporation)

conduction electron cloud with respect to the metal lattice and leads to a localized restoring field within the particle. The periodical shift of the electrons and change of the restoring field create coherent, resonant oscillations of the electron gas related to the exciting electromagnetic field. This phenomenon is called localized surface plasmon resonances (LSPRs) (Fig. 1.6).

Quasistatic Approximation can be used to describe LSPs in nanoparticles whose sizes are significant small compare with the wavelength of the exciting light [24]. Therefore exciting light can be regarded as a homogeneous field and the retardation over the particle volume can be neglected. Consider a homogeneous, isotropic sphere located at the origin in a uniform, static, homogeneous electric field $\boldsymbol{E}_0$, surrounding by an idea non-absorbing, isotropic medium with dielectric constant ε_m. Here we define the polarizability α via $\boldsymbol{p} = \varepsilon_0 \varepsilon_\mathrm{m} a \mathbf{E}_0$, where $\boldsymbol{p}$ is the dipole moment at the particle. By casting the Laplace equation, the complex polarizability is given by

$$\alpha = 4\pi a^3 \frac{\varepsilon(\omega) - \varepsilon_\mathrm{m}}{\varepsilon(\omega) + 2\varepsilon_\mathrm{m}} \tag{1.2.5}$$

where a and $\varepsilon(\omega)$ are the diameter and the dielectric function of the sphere of the sphere, respectively. The distribution of the electric field can be expressed as

$$\boldsymbol{E}_\mathrm{in} = \frac{3\varepsilon_\mathrm{m}}{\varepsilon(\omega) + 2\varepsilon_\mathrm{m}} \boldsymbol{E}_0 \tag{1.2.6}$$

$$\boldsymbol{E}_\mathrm{out} = \boldsymbol{E}_0 + \frac{3\boldsymbol{n}(\boldsymbol{n} \cdot \boldsymbol{p}) - \boldsymbol{p}}{4\pi \varepsilon_0 \varepsilon_\mathrm{m}} \frac{1}{r^3} \tag{1.2.7}$$

where $\boldsymbol{r}$ is the position vector point from the center of the sphere to the outside, $\boldsymbol{n}$ is the unit vector. The corresponding cross sections for scattering and absorption C_sca and C_abs are given by

$$C_{\text{sca}} = \frac{k^4}{6\pi}|\alpha|^2 = \frac{8\pi}{3}k^4a^6\left|\frac{\varepsilon - \varepsilon_{\text{m}}}{\varepsilon + 2\varepsilon_{\text{m}}}\right|^2 \tag{1.2.8}$$

$$C_{\text{abs}} = \text{Im}[\alpha] = 4\pi ka^3\text{Im}\left[\frac{\varepsilon - \varepsilon_{\text{m}}}{\varepsilon + 2\varepsilon_{\text{m}}}\right] \tag{1.2.9}$$

where $k = \frac{2\pi}{\lambda}$ is the wave vector of the exciting light. The extinction cross section can be defined as $C_{\text{ext}} = C_{\text{sca}} + C_{\text{abs}}$, i.e.

$$C_{\text{ext}} = 9\frac{\omega}{c}\varepsilon_{\text{m}}^{3/2}V\frac{\varepsilon_2}{[\varepsilon_1 + 2\varepsilon_{\text{m}}]^2 + \varepsilon_2^2} \tag{1.2.10}$$

When the particle diameter matches $a << \lambda$, the cross sections for scattering and absorption C_{sca} and C_{abs} scale with a^3 and a^6, respectively. Clearly all the scattering, both absorption and extinction of the particle are resonantly enhanced due to the LSPRs.

Quasistatic approximation can be relaxed to more complex geometrical shapes. For example, an ellipsoid with semiaxes specified by $\frac{x^2}{a_1^2} + \frac{x^2}{a_2^2} + \frac{x^2}{a_3^2} = 1$, where $a_1 \leq a_2 \leq a_3$, the polarizabilities α_i along the principal axes $i = 1,2,3$ can be written as

$$\alpha_i = 4\pi a_1a_2a_3\frac{\varepsilon(\omega) - \varepsilon_{\text{m}}}{3\varepsilon_m + 3L_i(\varepsilon(\omega) - \varepsilon_{\text{m}})} \tag{1.2.11}$$

where the geometrical factor L_i can be expressed as

$$L_i = \frac{a_1a_2a_3}{2}\int_0^\infty \frac{\text{d}q}{\left(a_i^2 + q\right)f(q)} \tag{1.2.12}$$

$$f(q) = \sqrt{\left(q + a_1^2\right)\left(q + a_2^2\right)\left(q + a_3^2\right)} \tag{1.2.13}$$

Despite only account for small plasmon structures with dipolar LSP modes, the quasistatic approximation still reveals the main profiles of the LSPs, i.e., the great field enhancement in the near field, and the significant scattering and absorption characteristics. The characteristics of LSPs can be influenced by the following factors, the shape and the size of the nanostructure (Figs. 1.7, 1.8), the dielectric function of the plasmon material and the dielectric function of the surrounding medium. Also, the excitation of the LSPs can be anisotropic for more complex plasmon structures with respect of the polarization of the exciting light (Fig. 1.9) [72].

Mie theory [73], based on the superposition of different eigenmodes which are dipolar or multipolar in character, provides a more exact analytical theoretical descripting of the absorption and scattering of light by spheres, especially for the spheres with a larger size, where the quasistatic approximation is not accurate. For more complex plasmon structures or the coupling among multiple structures, numerical computation protocols, such as, finite-different time-domain (FDTD) or finite

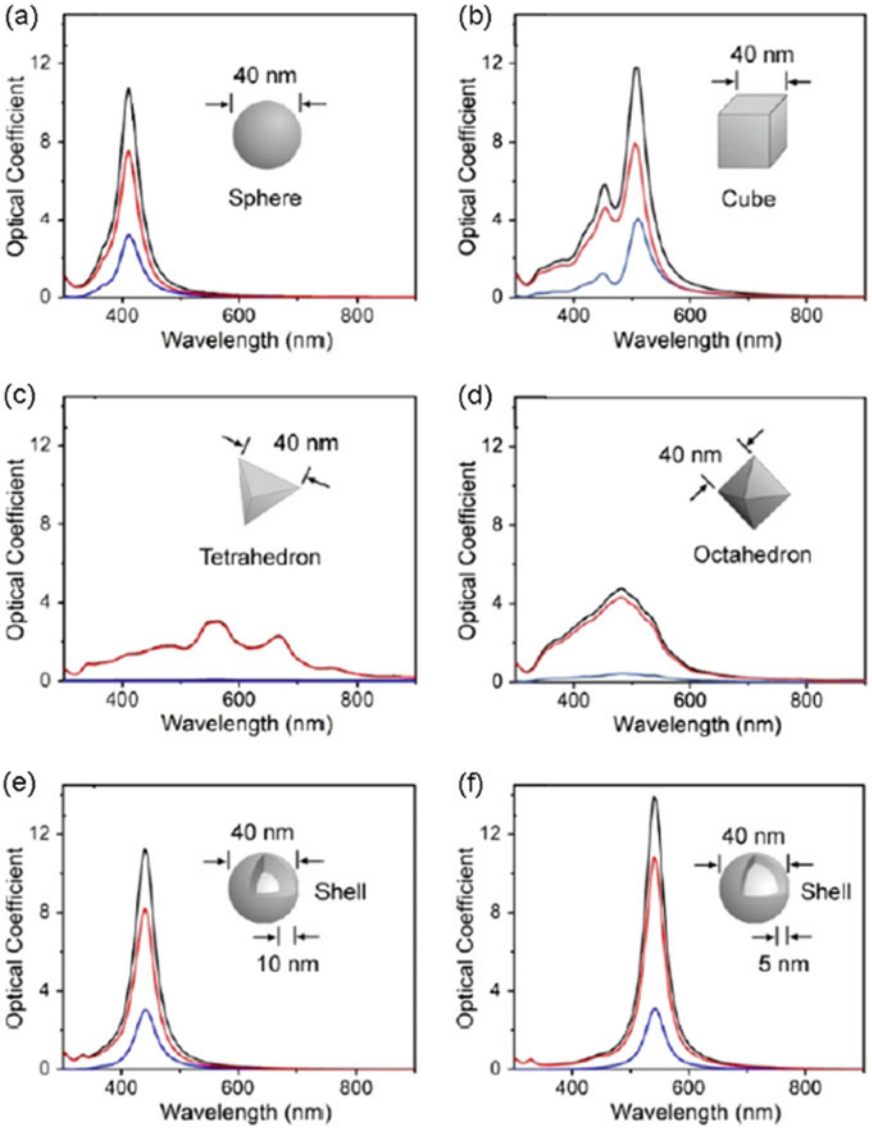

Fig. 1.7 The extinction spectra of nanoparticles in a variety of shapes. (Reprinted with permission from [74]. Copyright 2019 American Chemical Society)

element method (FEM), are more preferred to calculate the field distributions of the LSPs [24].

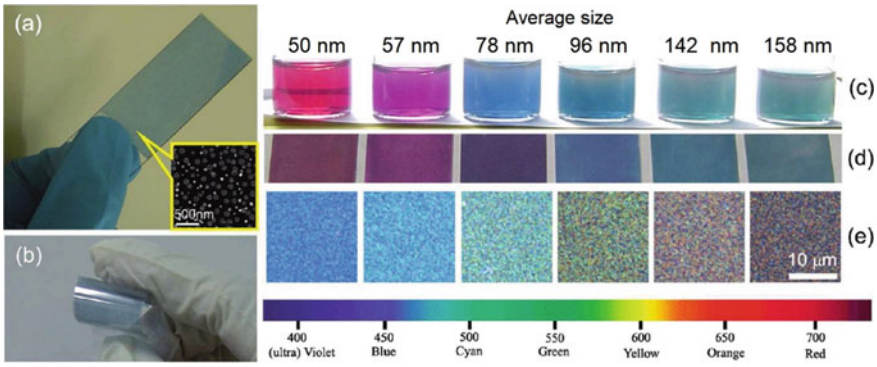

Fig. 1.8 The extinction spectra of silver nanoplates in a variety of sizes. (Reprinted with permission from [75]. Copyright 2011 American Chemical Society)

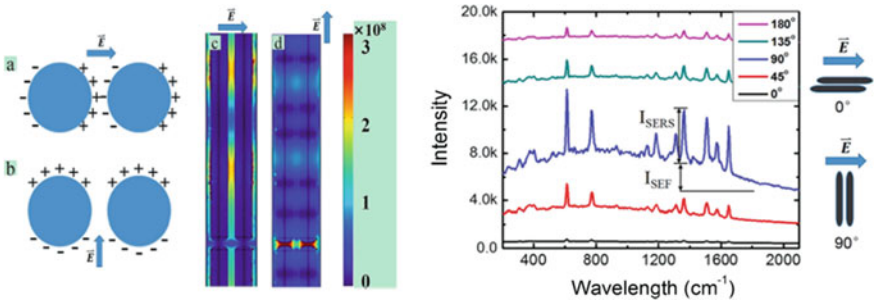

Fig. 1.9 The polarization dependence of the LSPs for nanoparticles in orthogonal directions. (Reprinted with permission from [76]. Copyright 2015 Royal Society of Chemistry)

1.3.3 Propagation Along an Optical Nanofiber (Optical Mode) and Metallic Nanowire (Plasmonic Mode)

Conventional dielectric fibers can guide electromagnetic modes with the core diameter thicker than the cut-off diameter. The lateral mode size in a dielectric fiber is limited by the diffraction limit to the order of λ/n, and will restrict higher degrees of miniaturization. Shown in Fig. 1.10, when the fiber diameter d is decreased, the evanescent fields of the fundamental mode extend deeper into the surrounding medium, which will degenerate the field confinement. Further decreasing the fiber diameter eventually turns the guided mode into a bulk plane-wave in the medium surrounding the fiber. The smallest mode size of conventional dielectric fiber is thus limited to a micrometer scale [77, 78].

Optical Nanofibers are one-dimensional (1D) nanoscale optical fibers with diameters in subwavelength scale (several hundred nanometers or less) respect to the guided light [79]. Compared with commercial glass fibers with diameters from several

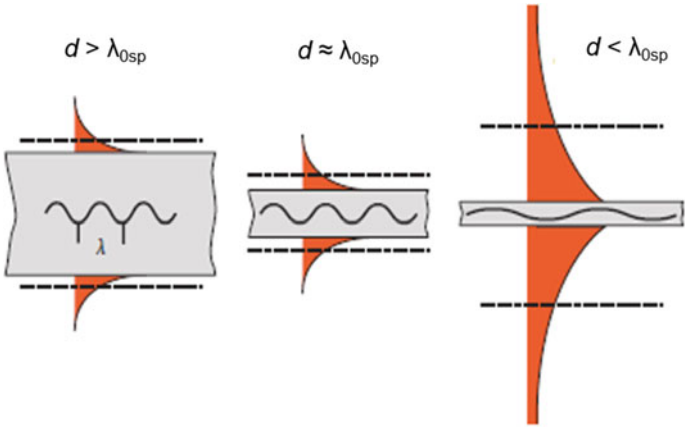

Fig. 1.10 The guided modes of the dielectric fibers with a variety of diameters. (Reprinted with permission from [77]. Copyright 2010. Springer Nature)

micrometers to hundreds of micrometers, optical nanofibers enable subwavelength or even deep subwavelength light guiding, and illustrate merits such as high optical confinement, strong field enhancement, small size and light weight. High optical confinement enables optical circuits with tight mode size, low loss sharp bends and short optical paths, which will be in favor of the minimization and condensing of optical or photonic devices, and may promote low-threshold or low-power optical nonlinear effects. Strong field enhancement will offer enhanced light-matter interactions at the nanofiber surroundings, and naturally promote the applications such as high sensitivity and fast response optical sensing. The steep gradient of the evanescent fields can provide large gradient force for optical trapping or deep potential wells for cold atom trapping and guiding.

Two mechanisms are mainly involved to realize subwavelength light guiding in optical nanofibers, high index difference for optical dielectric nanofibers and/or surface plasmon polaritons for plasmonic fibers.

High Index Difference is commonly utilized to construct optical dielectric nanofibers which supports optical waveguide modes. Shown in Fig. 1.11, a nanofiber consist a dielectric core with its refractive index n_1 significant higher than the index n_2 of the surrounding claddings such as vacuum, air and water. The guided light in optical dielectric nanofibers obtain the law for the conventional dielectric fibers. The mode size still contained by the diffraction limit. However, utilizing high-index core materials and high index difference ($\Delta n = n_1 - n_2$) can remarkably reduce the mode size and extend the optical fibers from micro scale to nano reign. A typical refractive index difference of an optical nanofiber ($\Delta n > 2$) is obviously higher than that of commercial optical fiber ($\Delta n \approx 0.01$).

The waveguiding properties for an optical nanofiber can be deduced from the Helmholtz equations

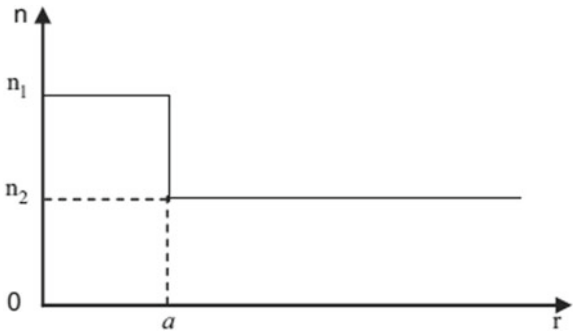

Fig. 1.11 Index profile of dielectric optical nanofibers. (Reprinted with permission from [79]. Copyright 2012. Elsevier Inc.)

$$\begin{aligned}\left(\nabla^2 + n^2k^2 - \beta^2\right)\boldsymbol{E} &= 0,\\ \left(\nabla^2 + n^2k^2 - \beta^2\right)\boldsymbol{H} &= 0\end{aligned} \tag{1.2.14}$$

where k is the wave vector of the light in vacuum and β is the propagation constant. Therefore the modes HE_{vm} and EH_{vm} can be expressed by the equations [79]:

$$\left\{\frac{(J'U)_v}{(UJU)_v + \frac{K'_v}{WK_v}\left\{\frac{(J'U)_v}{(UJU)_v + \frac{n_2^2K'_v}{n_1^2WK_v} = \left(\frac{v\beta}{kn_1}\right)^2\left(\frac{V}{UW}\right)^4}\right\}}\right\} \tag{1.2.15}$$

The $TE_{0\mathrm{m}}$ modes is given by

$$\left\{\frac{J_1(U)}{UJ_0(U)} + \frac{K_1(W)}{WK_0(W)}\right\} = 0 \tag{1.2.16}$$

The $TM_{0\mathrm{m}}$ modes is given by

$$\left\{\frac{n_1^2J_1(U)}{UJ_0(U)} + \frac{n_2^2K_1(W)}{WK_0(W)}\right\} = 0 \tag{1.2.17}$$

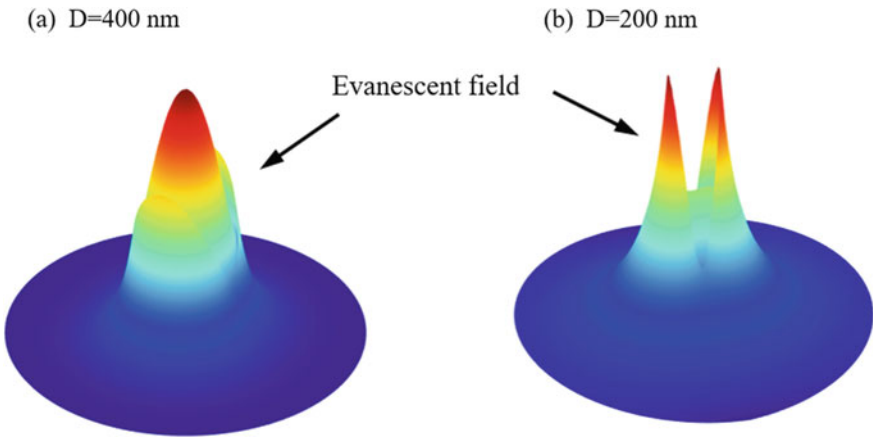

Fig. 1.12 Mode field distributions of dielectric optical nanofibers with thicknesses of **a** 400 nm and **b** 200 nm, respectively.

in which

$$U = a(k_0^2 n_1^2 - \beta^2)^{1/2}$$
$$W = a(\beta^2 - k_0^2 n_2^2)^{1/2}$$
$$V = k_0 a\left(n_1^2 - n_2^2\right)$$

J_v and K_v is the Bessel function of the first kind and the modified Bessel function of the second kind.

Figure 1.12 demonstrates the field distributions of nanofibers with diameters of 400 and 200 nm. A thinner nanofiber leads to a larger fractional evanescent fields which intrigue new opportunities for nanoscale light manipulation [80].

Surface Plasmon Polaritons (SPPs) are the coherent longitudinal charge oscillations of the conduction electrons coupled to the electromagnetic field at the interface of a metal and a dielectric, and are able to propagate along the interface [24]. Electromagnetic waves can be tightly confined around the interface in evanesce waves form with exponential distributions outwards from the dielectric-metal interfaces to both sides of metal and dielectric. [70] For plasmonic nanofibers, the fields decay exponentially in both the metal core and surrounding medium. The optical properties of SPPs can be deduced from Maxwell's equations of macroscopic electromagnetism and solve Helmholtz equation. The electromagnetic waves propagation along z directions matches the equations

$$\beta^2 + k_x^2 + k_y^2 = \varepsilon_\mathrm{m}\mu_0\omega^2 \tag{1.2.18}$$

$$\beta^2 - \kappa_x^2 - \kappa_y^2 = \varepsilon_\mathrm{d}\mu_0\omega^2 \tag{1.2.19}$$

where β is the propagation constant of the SPP mode, k_x, k_y, κ_x and κ_y are the component of the wavevector perpendicular to the interface in the two media, i.e., the metal cladding and surrounding dielectric. Note that, surface plasmons typically involve complex ε_m with negative real part and large imaginary part of ε_m. The k_x and k_y can be imaginary, making it possible to confine and guide the light beyond the beyond the diffraction limit in plasmon nanofibers like metal nanowires [81, 82] (Fig. 1.13).

The mode pattern of SPP can be much smaller than the optical propagation modes. When the diameter d of the plasmonic nanofiber is reduced below the wavelength λ_{0sp} of the SPP, there is significant reduction in the phase and group velocities, and thereby localization occurs [77]. It is possible to reduce the mode size of the guided SPP down to a few nanometers. Shown in Fig. 1.14, the diameter of plasmonic waveguide, $2a$, can be much smaller than $\lambda/(2n)$, the so-called optical diffraction limit.

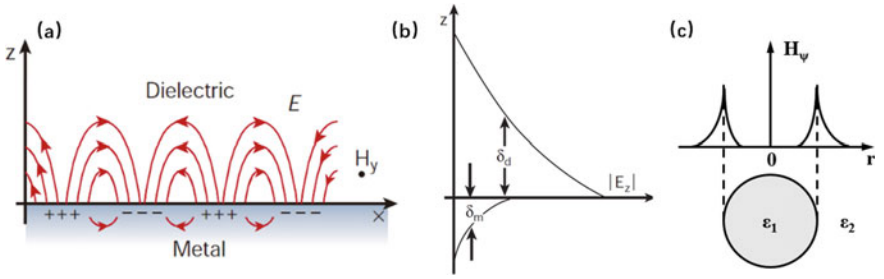

Fig. 1.13 Diagram of Surface plasmon polaritons (SPPs), **a** charge oscillations of the conduction electrons coupled to the electromagnetic field (Reprinted with permission from [69]. Copyright 2003. Springer Nature), field distributions of SPP modes propagate along, **b** a dielectric-metal interface (Reprinted with permission from [69]. Copyright 2003. Springer Nature.), and **c** a metal nanowire, showing the exponential distributions of the evanesce waves outwards from the dielectric-metal interface (reprinted with permission from [83] ©The Optical Society)

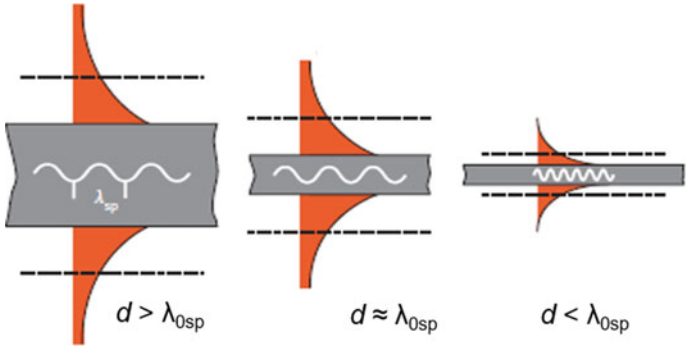

Fig. 1.14 The guided SPP modes of the metal nano wires with a variety of diameters (Reprinted with permission from [77]. Copyright 2010. Springer Nature)

The dielectric fiber, as we discussed in Fig. 1.10, on the contrary, with an extending of the evanescent fields, dramatically enlarges the mode sizes and eventually lose the effective confinement with a decreasing fiber diameter.

The dispersion relation of SPPs obeys the equation

$$\beta = k_0 \sqrt{\frac{\varepsilon_d \varepsilon_m}{\varepsilon_d + \varepsilon_m}} \tag{1.2.20}$$

in which $k_0 = \frac{\omega}{c}$ is the wavevector of the light in vacuum, ε_m an ε_d are the dielectric functions of the metal and the surrounding dielectric. The wavevector of the SPP mode $k_{sp} = \beta$ is obvious smaller than that of the light in vacuum. Therefore unlike LSPs, SPPs cannot be launched directly by incident light due to the momentum mismatch between the photons and plasmons. Techniques such as prism coupling, lens focusing, nanowire coupling and electron excitation were developed for the exciting of SPPs (Fig. 1.15).

Figure 1.16 demonstrates SPPs propagates along metal nanowires. With a bright spot of the exciting light at one end of a nanowire, dimmer spot can be observed at

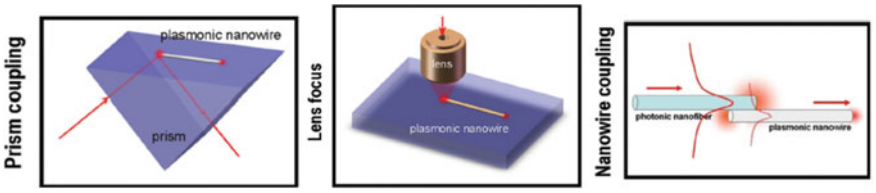

Fig. 1.15 Several techniques for the exciting of SPPs such as prism coupling, lens focusing and nanowire coupling (Reprinted with permission from [81]. Copyright 2013, Wiley-VCH)

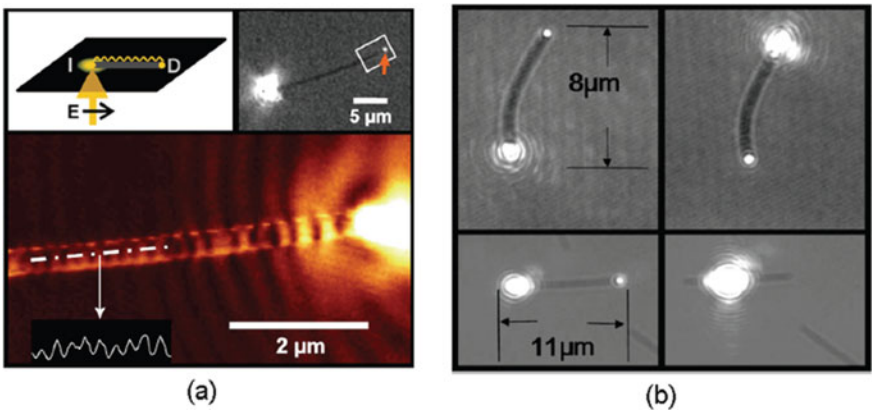

Fig. 1.16 SPPs propagates along metal nanowires (**a** Reprinted with permission from [84]. Copyright 2004 American Physical Society. **b** Reprinted with permission from [85]. Copyright 2006. American Chemical Society)

the other. The propagation of the SPP modes are limited by the attenuation due to the absorption in metal [84, 85].

The propagation length of SPP is given by

$$\delta_{sp} = \frac{1}{2k''_{sp}} = \frac{c}{\omega}\left(\frac{\varepsilon_d + \varepsilon'_m}{\varepsilon_d \varepsilon'_m}\right)^{\frac{3}{2}} \frac{\left(\varepsilon'_m\right)^2}{\varepsilon''_m} \tag{1.2.21}$$

in which k''_{sp} is the imaginary part of the complex SPP wavevector $k_{sp} = k'_{sp} + ik''_{sp}$, ε'_m and ε''_m are the real and imaginary parts of the complex dielectric function of the metal

$$\varepsilon_m = \varepsilon'_m + i\varepsilon''_m. \tag{1.2.22}$$

The propagation length of a SPP mode is strictly dominated by the mode size. For a silver nanowire, the propagation length typically ranges from hundreds of nanometers to several micrometers (Fig. 1.15). This characteristic sets the upper size limit for any photonic circuit based on SPPs.

To extend the propagation length, hybrid plasmon mode involve together with optical waveguide modes and SPP modes, and combine the superiority from both high index difference and SPPs [86, 87]. Fig. 1.17 demonstrates two configurations involves hybrid plasmon modes. Figure 1.18 shows subwavelength devices based on plasmonic circuits: plasmonic route, logic gate and the hybrid nanophononic circuits.

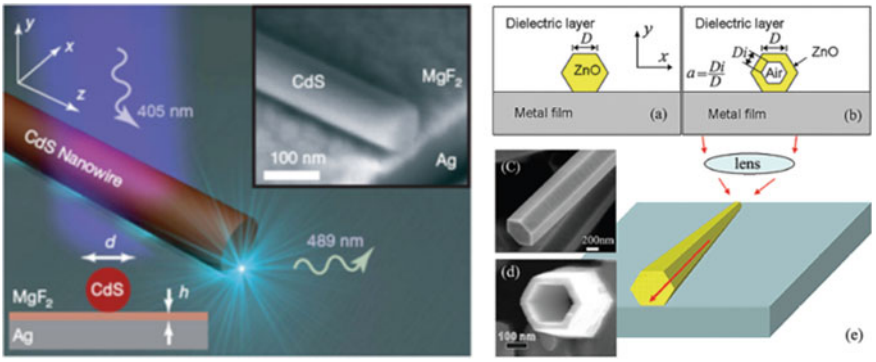

Fig. 1.17 Configurations involves hybrid plasmon modes (**a** Reprinted with permission from [87]. Copyright 2009. Springer Nature. **b** Reprinted with permission from [53]. Copyright 2010. American Institute of Physics Publishing)

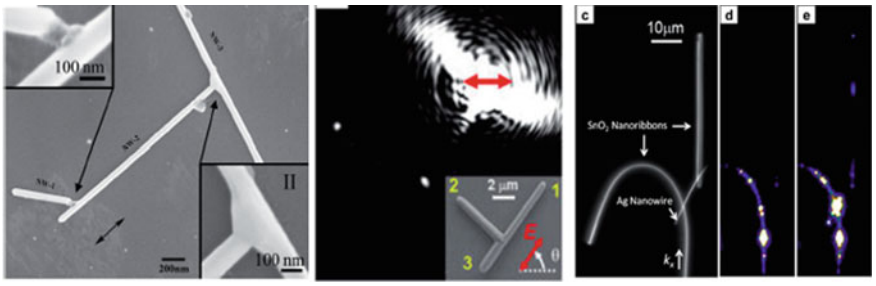

Fig. 1.18 Subwavelength devices using plasmonic nanofibers: plasmonic route (Reprinted with permission from [88]. Copyright 2016. Institute of Physics publications), logic gate (Reprinted with permission from [89]. Copyright 2010. American Chemical Society) and hybrid nanophotonic circuits (Reprinted with permission from [90]. Copyright 2009. Proceedings of the National Academy of Sciences)

1.3.4 Nanocomposite Absorption and Photothermal Effect

Photothermal effect is a well-known phenomenon that involves light absorption and heat generation. Nanocomposites consisting of metal nanostructures and other dielectrical/polymer materials, are considered as efficient and localized light-driven heat sources due to the huge absorption cross sections, effective light concentration and strong absorption medium due to large Ohmic losses of light-induced surface plasmons [61]. The heat from surface plasmons is generated from two parts, metal nanostructures and the surrounding dielectrics.

Photothermal effects in metal nanostructures arise from the exciting of surface plasmons. Surface plasmons can decay nonradiatively, which create energetic carriers, referred as "hot" carriers (electrons and/or holes) [91]. Following Landau damping, the athermal distribution of electron–hole pairs decays through two pathways, re-emission of photons or carrier multiplication caused by electron–electron interactions. Then the hot carriers will redistribute their energy by electron–electron scattering processes, subsequently generate heat through a Joule effect (i.e., electron-lattice scattering), and eventually transfer to the surroundings of the metal nanostructure through thermal conduction [92].

Since the heat originates from Joule effects, the heat power density distribution ($q(\boldsymbol{r}, t)$) in the metal nanostructure is given by [93]

$$q(\boldsymbol{r}, t) = \boldsymbol{j}(\boldsymbol{r}, t) \cdot \boldsymbol{E}(\boldsymbol{r}, t) \tag{1.2.23}$$

in which $\boldsymbol{j}(\boldsymbol{r}, t)$ and $\boldsymbol{E}(\boldsymbol{r}, t)$ are the complex amplitude of the electronic current density and the complex electric field intensity inside the metal, respectively. The equation can be write as

$$q(\boldsymbol{r}) = \frac{1}{2}\varepsilon_0 \omega \,\mathrm{Im}[\varepsilon(\omega)]|\boldsymbol{E}(\boldsymbol{r})|^2 \tag{1.2.24}$$

Obviously, the imaginary part ($\mathrm{Im}[\varepsilon(\omega)]$) of the dielectric functions of the nanostructure, represents the loss in the nanostructure, and contributes to the heat generation.

Surrounding the metal nanostructures, organic or inorganic mediums serve as the dielectrics which affect the field distributions of the surface plasmons and in turn impact the light absorption and heat generation processes. The absorption of light by the surrounding medium also contribute to the heat generations to some extent.

The total heat power p can be obtained from

$$p = \oint_v q(\boldsymbol{r})\mathrm{d}V \tag{1.2.25}$$

where the integral runs over the metal nanostructure volume V.

Let us consider a silver/organic nanocomposite cluster (Fig. 1.19), which consists of layered silver nanoplates with 3 nm-thick polyvinylpyrrolidone (PVP) shell capped on each of the nanoplate. The surface plasmons is extremely localized within the ultra-small volume between two silver nanoplates due to the strong plasmon coupling effect [94], whereas very limited electric field distribute in silver [75]. The heat, on the other hand, generates mainly in the silver reign due to the strong absorption in metal. However, the heat generated in PVP is several orders of magnitude smaller

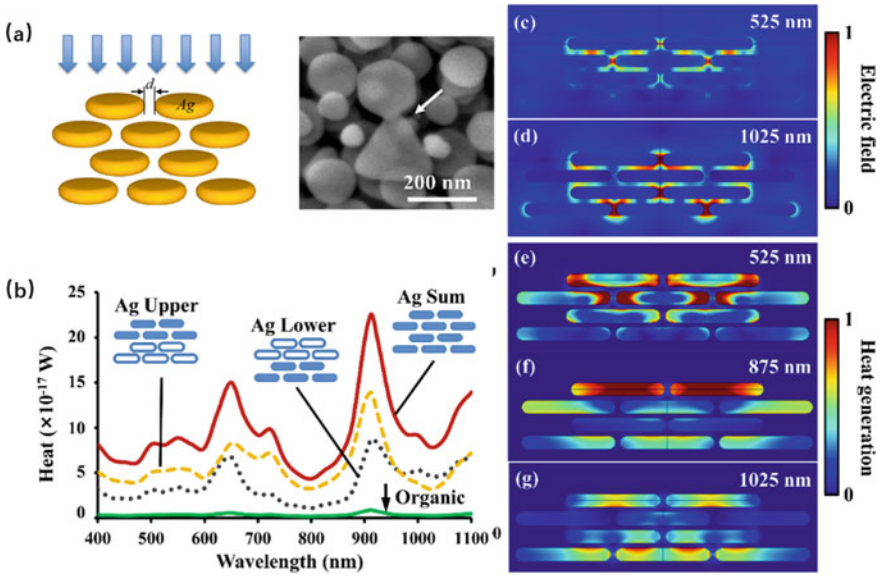

Fig. 1.19 Photothermal effect in a silver/polyvinylpyrrolidone (PVP) nanocluster, **a** diagram of the setup and SEM images of silver nanoplates, **b** calculated heat generation as a function of wavelength, electric field distributions with light wavelengths of **c** 525 nm and **d** 1025 nm, and heat distributions at wavelengths of **e** 525 nm, **f** 875 nm and **g** 1025 nm, respectively (Reprinted with permission from [95]. Copyright 2015 Royal Society of Chemistry)

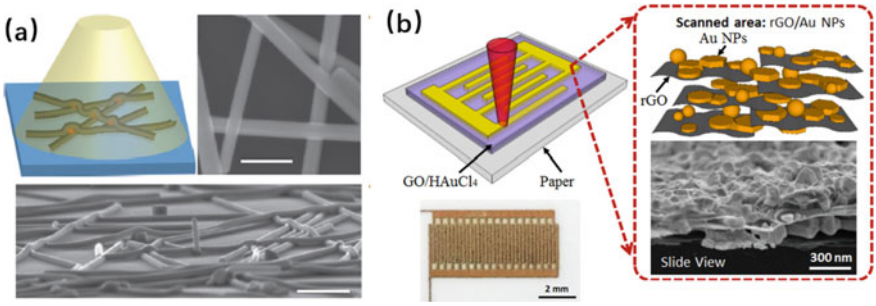

Fig. 1.20 Applications of photothermal effects, **a** photonic sintering (Reprinted with permission from [94]. Copyright 2012. Springer Nature.), **b** laser direct writing (Reprinted with permission from [98]. Copyright 2015 Royal Society of Chemistry)

than that generated in silver. Also, similar to Ag nanowires, heat generation is highly localized and self-contained in the junction point, creating "hot spots". Despite the heat at the hot spots can rapidly spread to the whole Ag nanoplate because of the high thermal conductivity of silver, the heat could be contained in several to hundreds nanometers scale depended on the size and shape of the nanostructures [61].

Besides the aforementioned merits, such as, highly localized heating and efficient light conversion, light-induced heat generation can be well controlled by multiple factors: material absorption involving material, geometrical morphology, size, etc., and incident light properties, such as light intensity, dose, polarization, direction, spectra and even pulse parameters for pulsed light sources. For example, the photothermal effects shows strong wavelength dependency in the silver/PVP nanocluster. The peaks in the heat-wavelength curves (Fig. 1.19b) typically reveals the strong surface plasmon resonance as well as the high efficient heat generation. Therefore, photothermal effects in nanocomposites naturally stimulate vast physical processes and chemical reactions with unprecedented spatial and temporal controls [94, 96]. Shown in Fig. 1.20, applications of photothermal effects have been extend to the fields as photothermal therapy [97, 100], laser direct writing [98], photonic sintering [94], solar energy harvesting [62], surface modification [99], and so on.

1.4 Photothermal Versus Photonic Nonthermal Manufacturing

1.4.1 Photonic Sintering

Photonic sintering is critical for printed electronics and 3D printing. Compared to conventional thermal sintering photonic sintering is a local effect by highly selected

surface plasmonic excitation. As aforementioned, the locally excited plasmonic resonance can only heat the adjacent particles with the narrowest gap. Besides, plasmonic sintering is more energy efficient by selected wavelength for excitation than the thermal sintering. The most unique feature of photonic sintering is "smart" and self-terminated: once the adjacent particles are fused together the new plasmonic excitation will automatically move to the new adjacent positions which usually locate at the edge of a pore [94, 101, 102]. Thus, the particle fusion induced by plasmonic sintering will lead to the eventual disappearance of pores.

The nature of photonic sintering that photothermally induced diffusion. For the diffusion, the liquid phase diffusion is much faster than a solid-state diffusion since the diffusivity in a liquid is much higher than in a solid [103]. As discussed in Sect. 1.1.2, the surface atoms are much activated than the inner atoms due to less bonding and the surface defects [40]. As a result, the sintering temperature can be much lower than the melting point of a particle. The onset sintering temperature as a function of the melting temperature can be written as

$$T_s(d) = \alpha T_m(d) \tag{1.3.1}$$

where the d is the particle diameter. For microparticles, α ranges from 0.5 to 0.8 [40], but for nanoparticles, this value decreases to 0.1–0.3 [45]. This indicates that the sintering of nanoparticles can occur at a very low temperature, only 10% of the melting point. This explains nanomaterials can be joined even at a room temperature without external heating [47]. Considering a possible surface melting of nanoparticle and thereby associated a liquid phase sintering, sintering of nanoparticles for 2D to 3D printed electronics and functional mechanical components are extremely attracted in micro-to-nanomanufacturing.

Diffusion Mechanisms Based on a conventional sintering theory, the driving force for sintering is dependent on the curvature of two touched particles, i.e., (Fig. 1.21)

$$\sigma = \gamma\left(\frac{1}{R_1} + \frac{1}{R_2}\right) \tag{1.3.2}$$

where γ is the specific surface energy, R_1 and R_2 are principle radii of two spherical particles. For two identical particles with a radium of r, the neck size can be expressed a function of r [104],

$$\frac{x}{r} = \left(\frac{Bt}{r^m}\right)^{1/n} \tag{1.3.3}$$

where t is the sintering holding time, B is a temperature-dependent sintering function, and the values of m and n are defined by individual diffusion mechanisms. Three dominant mechanisms have been discussed as the surface diffusion, grain boundary diffusion and the lattice diffusion. If sintering is driven by surface diffusion, (1.3.3) becomes

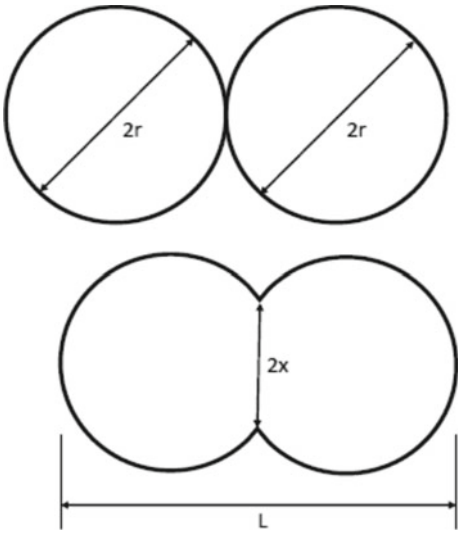

Fig. 1.21 sintering of two particles with the identical radiums

$$\left(\frac{x}{r}\right)_{\text{surf}} = \left(\frac{4.17\delta D_s \gamma_{sv} \Omega t}{RTr^4}\right)^{1/6} \tag{1.3.4}$$

where δ is the surface layer thickness and is estimated as 0.3 nm for Ag [105]) D_s is the surface diffusion coefficient calculated by (2), δ_{sv} is the bulk solid-vapor interfacial surface energy and is estimated as 1.14 J/m^2 for Ag [106]) and Ω is the molar volume (10.3 cm^3/mol for Ag). If sintering is driven by grain boundary diffusion, (1.3.3) becomes

$$\left(\frac{x}{r}\right)_{\text{gb}} = \left(\frac{32\omega D_{\text{gb}} \gamma_{sv} \Omega t}{RTr^4}\right)^{1/6} \tag{1.3.5}$$

where w is the grain boundary width and is estimated as 0.5 nm for Ag [105]) and D_{gb} is the grain boundary diffusion coefficient, which can be calculated by (1.1.8). For lattice diffusion sintering, (1.3.3) becomes

$$\left(\frac{x}{r}\right)_{\text{l}} = \left(\frac{42.05 D_l \gamma_{sv} \Omega t}{RTr^3}\right)^{1/4.78} \tag{1.3.6}$$

where D_l is the lattice diffusion coefficient calculated by (1.1.8). $D_s = 5 \times 10^3$ m^2/s) for surface diffusion, $D_{\text{gb}} = 1.2 \times 10^5$ m^2/s) for grain boundary diffusion, and $D_l = 4.4 \times 10^5$m^2/s) for volume diffusion [107]. $E(\infty)$ is bulk activation energy and is equal to ($E(\infty) = 2.661 \times 10^5$J/mol), ($E(\infty) = 9 \times 10^4$ J/mol), and ($E(\infty) = 18.5 \times 10^4$J/mol) for surface diffusion, grain boundary diffusion, and lattice diffusion, respectively [107, 108]). Dependent on different materials, particle size, particle shape and local temperatures, one of these or two, even three of them may involve the

underlying diffusion. It is possible to identify these mechanisms by characterizing the neck variation as a function of time. Nevertheless, there is limited experimental analyses by these models. The molecular dynamics simulations display remarkable differences from these models [107, 108]. The further investigation is desired to verify these models at a nanoscale.

It is extensively to use a pulsed light rather than a continue wave (constant) light for photonic sintering. With a constant energy output, a pulsed laser indicates a higher peak, which allows a deep penetration since the penetration is proportional to the input power. Besides, the pulsed laser allows the photothermal energy dissipation with a pulse gap for cooling. For sintering of printed circuit with pulsed light, because of the absorption difference of printed materials and substrates, it is possible to limit the thermal effect on the oriented layer only by choosing the proper wavelength. The metallic particles mainly absorb a visible or infrared light while the plastic/paper absorbs a ultraviolet light. It is thus reasonable to use a long-wavelength light for photonic sintering to avoid the thermal accumulation onto the plastic/paper substrate. This feature has advantage because one can print circuits onto a cheap plastic and/or paper substrates for flexible and/or stretchable devices for wearable/portable electronics [101, 109]. On the other hand, it is worth noting that the plasmonic resonant frequency is proportional to the anisotropy of nanomaterials. This means that the resonant wavelength has a blue-shift while the sintering processing [5, 75]. Thus, if the photonic sintering is completed by integrating different light sources, one should put a longer light sources before a short light source. Figure 1.22 shows a practical photonic sintering system by combining three kinds of pulsed light for sintering of printed Cu circuits [110].

The single sintering will gradually lead to the decrease of resistance. However, due to the inhomogeneous distribution of grain size as well as the diffusion is influenced by grain orientations and impurity on the grain boundaries, it is naturally predicted that there are large variation of local resistivity [111]. Thus, the global resistivity of printed circuits will dependent on several factors including the scattering from grain boundaries and surface roughness. It is extensively expressed the resistivity as follows [112],

$$\rho = \rho_{\mathrm{b}} + \rho_{\mathrm{im}} + \frac{\rho_{\mathrm{gb}}\sigma_{\mathrm{gb}}}{R} + \frac{\rho_{\mathrm{s}}s}{h} \tag{1.3.7}$$

where ρ_{b} is the bulk resistivity, ρ_{im} is due to the impurity scattering, this 3rd term is the resistivity due to the scattering of grain boundaries, R is the grain size and σ_{gb} is the grain boundary width, ρ_{gb} is the specific boundary resistivity and the last term comes from the surface scattering with s the surface roughness, h the film thickness and ρ_{s} the specific surface resistivity. Microstructure observation can determine σ_{gb} and R. Atomic force microscopy measurements can determine the surface roughness. During the transient temperature can be measured by a high speed infrared (IR) camera. Assuming the ρ_{b} and ρ_{im} unchanged during curing, one can deduce the resistivity arising from grain boundaries and surface scattering at different

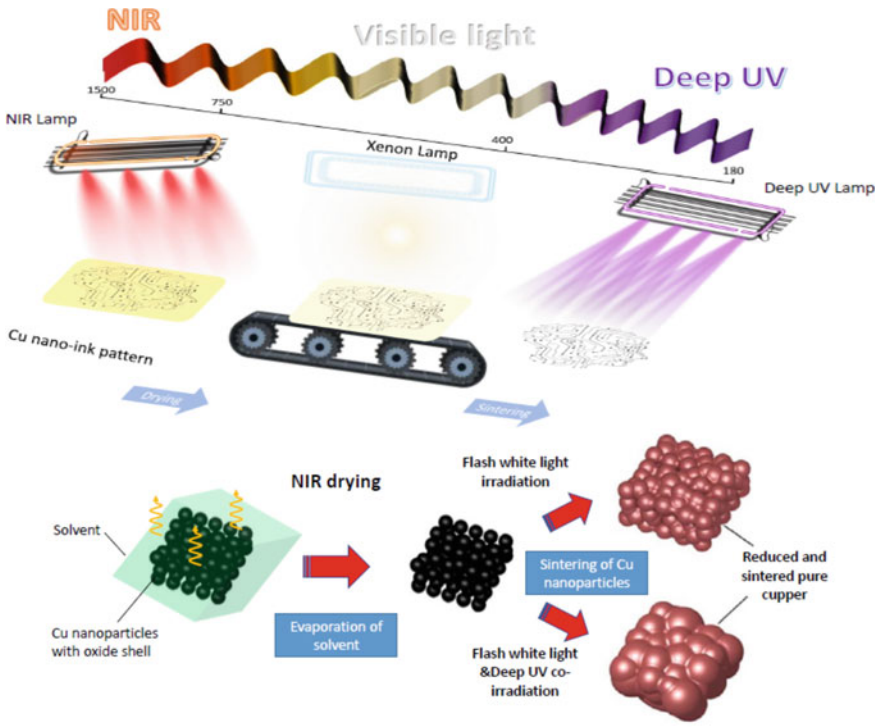

Fig. 1.22 Photonic sintering with different light sources. Adapted from [110]

temperatures. From the relationship between the microstructure and resistivity one can easily optimize the processing window of photonic sintering.

1.4.2 Ultrafast Laser Versus Long Pulsed and Continue Wave Laser Direction

Although laser has been extensively employed for precise manufacturing down to a nanoscale the physics procedure of laser-matter interaction will be significantly influenced by laser pulse widths since the relevant energy and mass transfers will take different characteristic times. To elucidate these procedures is critical to optimize laser-based manufacturing. Before we discuss nanomaterials processed by different lasers let us first check the physics model for laser-matter interaction with different pulse widths.

Two-Temperature Model for Different Pulsed Lasers According to a one-dimensional, two-temperature diffusion model [113, 114] the energy of low intensity

short laser pulses is absorbed by free electrons due to inverse Bremsstrahlung (Joule heat). The evolution of the absorbed energy involves thermalization within the electron gas (electron subsystem), energy transfer to the lattice and thermal diffusion in the lattice. These processes can be expressed as:

$$C_{\mathrm{e}}\frac{\partial T_{\mathrm{e}}}{\partial t} = \frac{\partial Q(z)}{\partial Z} - \gamma(T_{\mathrm{e}} - T_{\mathrm{l}}) + S \tag{1.3.8}$$

$$C_{\mathrm{l}}\frac{\partial T_{\mathrm{l}}}{\partial t} = \gamma(T_{\mathrm{e}} - T_{\mathrm{l}}) \tag{1.3.9}$$

$$Q(Z) = -k_{\mathrm{e}}\frac{\partial T_{\mathrm{e}}}{\partial z}, \quad S = I(t)A\alpha\exp(-\alpha Z) \tag{1.3.10}$$

here z is the direction of energy propagation perpendicular to the target surface, $Q(z)$ is the heat flux, S is the laser source function, $I(t)$ the laser intensity, $A = 1 - R$ is the surface transmissivity and α is the absorption coefficient. C_{e} and C_{l} are the specific heat of the electron and lattice subsystems with $C_{\mathrm{e}} = aT_{\mathrm{e}}$ where a is a constant, γ is the electron-lattice coupling parameter, and k_{e} is electron thermal conductivity. In (1.3.8) we should consider three characteristic time scales: τ_{e}, τ_{i}, and τ_{L}. $\tau_{\mathrm{e}} = C_{\mathrm{e}}/\gamma$ is the electron cooling time, $\tau_i = C_{\mathrm{l}}/\gamma$ is the lattice heating time and τ_{L} the laser pulse width. Following previous studies [9, 115], the laser pulses can be separated into three kinds of time regimes.

Femtosecond Pulses For a fs pulse, the laser width is much shorter than the electron cooling time, $\tau_{\mathrm{L}} \ll \tau_{\mathrm{e}} \sim 1$ ps. Then, $C_{\mathrm{e}}T_{\mathrm{e}}/t \gg \gamma T_{\mathrm{e}}$, and electron-lattice coupling can be neglected. If $D_{\mathrm{e}}\tau_{\mathrm{L}} < \alpha^{-2}$, where $D_{\mathrm{e}} = k_{\mathrm{e}}/C_{\mathrm{e}}$ is the electron thermal diffusivity, the electron heat conduction term can be neglected and (1.3.8) reduces to

$$C_e'\frac{\partial T_{\mathrm{e}}^2}{\partial t} = 2I_\alpha\alpha\exp(-\alpha z) \tag{1.3.11}$$

and gives

$$T_{\mathrm{e}}(t) = \left(T_0^2 + \frac{2I_\alpha\alpha}{C_{\mathrm{e}}'}t\exp(-\alpha z)\right)^{1/2} \tag{1.3.12}$$

here it is assumed that $I(t) = I_0$ and $I_a = AI_0$, while $T_0 = T_{\mathrm{e}}(0)$ is the initial temperature. $C_{\mathrm{e}}' = C_{\mathrm{e}}/T_{\mathrm{e}}$ is a constant when T_{e} remains smaller than the Fermi energy (in temperature). At the end of the laser pulse the electron temperature is given by

$$T_{\mathrm{e}}(\tau_{\mathrm{L}}) \approx \left(\frac{2F_\alpha\alpha}{C_{\mathrm{e}}'}\right)^{\frac{1}{2}}\exp\left(-\frac{z}{\delta}\right) \tag{1.3.13}$$

where $T_e(\tau_L) \gg T_0$, $F_a = I_a \tau_L$ is the absorbed laser fluence, and $\delta = 2/\alpha$ is the skin depth. After the laser pulse the electrons are rapidly cooled due to energy transfer to the lattice and heat conduction into the bulk. Since the electron cooling time is very short, (1.3.9) can be written as $T_i \sim T_e(\tau_L)t/\tau_i$ (neglecting the initial lattice temperature). The maximum lattice temperature can be estimated from the average cooling time of the electrons,

$$\tau_e^a \sim \frac{\tau_e}{2} = C_e^{'} \frac{T_e(\tau_e)}{2\gamma}$$

and is given by

$$T_l \sim T_e^2(\tau_L) \frac{C_e^{'}}{2C_l} \approx \frac{F_a a}{C_l} \exp(-az) \tag{1.3.14}$$

Significant evaporation will occur when $C_i T_i > \rho L_v$, where ρ is the density and L_v is the specific heat of evaporation. Using (1.3.14), we can express the condition of strong evaporation as $F_a \geq F_{th} \exp(az)$, where $F_{th} \sim \rho L_v/\alpha$ is the threshold laser fluence with fs pulses. Then the ablation depth per pulse L is

$$L \approx \alpha^{-1} \ln\left(\frac{F_a}{F_{th}}\right) \tag{1.3.15}$$

Such a logarithmic dependence of the ablation depth per pulse has been confirmed by the ablation of copper in vacuum using 150 fs laser pulses (780 nm, Momma et al. 1997) and in the ablation of highly oriented pyrolytic graphite (HOPG) with 120 fs pulses [16, 116]. It is notable that this penetration depth, standing for the influence regime of hot electrons, may be larger than the optical penetration depth described in formula (1.1.1).

Picosecond Pulses For a ps pulse, $\tau_e \sim 1$ ps $< \tau_L < \tau_i \sim 10$ ps. At times $t \gg \tau_e$, $C_e T_e/t \ll \gamma T_e$, (1.3.8) becomes quasi-stationary, (1.3.8)–(1.3.10) reduce to

$$\frac{\partial}{\partial z}\left(\frac{k_e \partial T_e}{\partial z}\right) - \gamma(T_e - T_l) + I_a a \exp(-az) = 0 \tag{1.3.16}$$

$$T_l = \frac{1}{\tau_l} \int_0^t \exp\left(-\frac{t-\theta}{\tau_l}\right) T_e(\theta) \mathrm{d}\theta + T_0 \tag{1.3.17}$$

The integral corresponds to the temperature increase of the lattice. At $t \ll \tau_i$, (1.3.17) can be simplified due to the quasi-stationary character of the electron temperature. Neglecting T_0, we get

$$T_l \approx T_e\left(1 - \exp\left(-\frac{t}{\tau_l}\right)\right) \approx \left(\frac{t}{\tau_l}\right) T_e \tag{1.3.18}$$

It is obvious that in the ps regime the lattice temperature remains much lower than the electron temperature. Thus the lattice temperature can be omitted in (1.3.16). When the condition $k_e T_e \alpha^2 \ll \gamma T_e$ is fulfilled (1.3.16) and (1.3.11) are very simple. The electron and lattice temperatures at the end of a ps pulse are given by

$$T_e \approx \frac{I_a a}{\gamma} \exp(-az) \tag{1.3.19}$$

$$T_l \approx \frac{F_a a}{C_l} \exp(-az) \tag{1.3.20}$$

Note that the obtained lattice temperature is governed by the electron cooling time. Thus, in fs and ps regimes (1.3.14), (1.3.19) and (1.3.20) give the same expression for the lattice temperature. This indicates that a logarithmic dependence of the ablation depth on laser fluence is also found in the ps regime. However, this conclusion is based on an assumption that the electron heat conduction is negligible. This is a very crude approximation since the electron heat conduction and the formation of melted zone must be related in ps ablation.

Nanosecond Pulses Ablation with ns pulses can be modeled with the condition $\tau_i \sim 10$ ps $\ll \tau_L$. In this case, the electron and lattice temperatures are equal, $T_e = T_l = T$ and (1.3.8)–(1.3.10) reduce to

$$\frac{C_l \partial T}{\partial t} = \frac{\partial}{\partial z\left(\frac{k_0 \partial T}{\partial z}\right)} + I_a a \exp(-az) \tag{1.3.21}$$

There are many experimental and theoretical studies on the processes involved in laser heating and irradiation with long pulses [117]. In this regime the target surface is first heated to the melting point and then to the vaporization temperature. During the interaction the dominant energy loss is heat conduction into the solid target. The heat penetration depth is given by $l \sim (Dt)^{1/2}$, where $D = k_0/C_i$ is the thermal diffusivity. Note that for a long pulse, $D_L \gg 1/\alpha^2$. The energy deposited inside the target per unit mass is given by $E_m \sim It/\rho l$. Evaporation occurs when $E_m \sim L_v$ at t_{th}, where L_v is the specific heat of evaporation. So, the condition for strong evaporation becomes, $E_m > L_v$ (or $\tau_L > t_{th}$) and

$$\begin{aligned} I &\geq I_{th} \sim \frac{\rho L_v D^{1/2}}{\tau^{1/2}} \\ F &> F_{th} \sim \rho L_v D^{1/2} \tau_l^{1/2} \end{aligned} \tag{1.3.22}$$

for the laser intensity and the fluence, respectively. A striking characteristic is that the threshold laser fluence depends on the square root of the laser pulse width. A deviation of the damage threshold from the $\tau^{1/2}$ scaling with short pulses has been clearly evident by ablation of fused silica by infrared (1053 nm) and visible (526 nm) laser radiation [118].

In summary of this section, fs pulses trigger a nonthermal ablation mechanism since both the electron-lattice thermal coupling and thermal diffusion to the lattice take longer time than the pulse width. ns pulses allow thermal equilibrium to occur between the electrons and the lattice.

Comparative Study Between Ultrashort Laser and Continue Wave Laser Interacted with 1-D Nanowire Due to the size effect, thermal diffusion in a nanoscale will be quite different from the aforementioned macroscale. Besides, the energy radiation, reflection and dissipation to the environment have to be considered. To understand the local melting of a Cu nanowire (Cu NW) using a focused laser beam, we recently conducted a comparative study with 1030 nm FS laser and 532 nm continuous-wave (CW) green laser at different power and atmosphere conditions [6]. To support the experimental observation and explain the difference between two types of laser irradiation, we examined computational modeling of the temperature distribution of CuNW. For the simulation, we model CuNW as a circular rod with a length of 30 μm and a diameter of 200 nm and assume that laser is irradiated at the tip of a modeled NW, and the temperature is distributed only along the length (defined as x direction) as shown in Fig. 1.23.

A one-dimensional (1-D) heat diffusion model and the finite difference method are employed for the thermal analysis of two types of laser irradiation: femtosecond laser (FS) and a continue wavelength laser at 532 nm (CW). In the case of CW laser, assuming a steady heat supply, the single-temperature model is used to calculate the temperature distribution and its evolution. In contrast, simulations of FS laser irradiation consider the electron and lattice temperatures (T_e and T_l), separately, (i.e., the aforementioned two-temperature model) due to the time-dependent heat flow from electrons to lattice.

Single-Temperature 1-D Heat Diffusion Model The temperature distribution in Cu nanowire (CuNW) and its evolution during the CW laser heating are calculated by using the single-temperature 1-D heat diffusion model and the finite difference

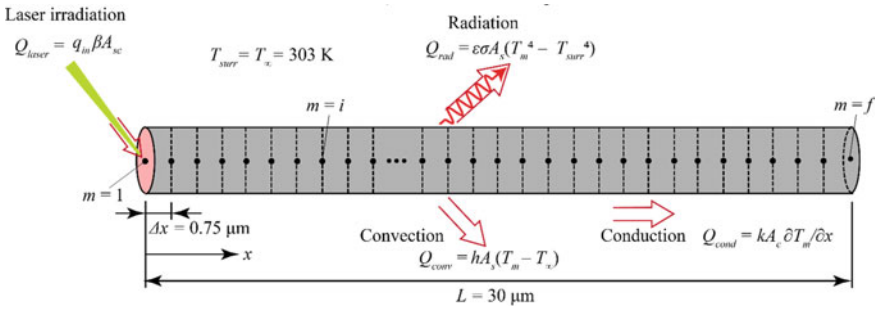

Fig. 1.23 Computational model of 30 μm long CuNW for 1-D heat diffusion equation solved with finite difference method simulation. Convection and radiation heat transfer are considered as the experiment occurred in the ambient atmosphere. The heat source from laser is considered at the tip (first nodal point) of the CuNW [6]

method. The energy balance in control volume of each nodal point (m) is used as the following governing equation [119, 120]:

$$Q_{\text{laser}} + Q_{\text{cond}} - Q_{\text{conv}} - Q_{\text{rad}} = \Delta E_{\text{st}}, \tag{1.3.23}$$

where Q_{laser} is the heat addition by laser and considered for the first nodal point ($m = 1$ or $x = 0$) only, Q_{cond} is the net heat conduction flow to the neighboring nodes, Q_{conv} and Q_{rad} are the convection and radiation heat loss through the CuNW surface, and ΔE_{st} is the change of stored heat in the control volume of each node. Here, for simplification, this analysis excludes heat dissipation through the substrate. This omission of the CuNW/substrate conduction heat transfer is because its inclusion can impose excessive complexities (from contact shape, roughness, and interfacial transport) although their influence is not significant (due to roughness and smaller actual contact area) and can be included in other surface heat dissipation terms (Q_{conv} and Q_{rad}). Q_{laser} is given as the product of laser heat flux q_{in}, absorptance (ratio of the absorbed to the incident radiant power) β, and the first node surface area, i.e., $Q_{\text{laser}} = q_{\text{in}}\, \beta A$, and our simulations employ $q_{\text{in}} = 4.46 \times 10^{10}$ W/m^2 for CW laser and $\beta = 0.5$ at the wavelength of CW laser (532 nm) [121]. Q_{cond} is calculated using nodal temperatures (T_{m}) and Cu thermal conductivity, $k = 400$ W/m K with 1-D Fourier heat conduction equation [119]. The convection and radiation heat transfer are calculated as $Q_{\text{conv}} = hA(T_{\text{m}} - T_{\infty})$ and $Q_{\text{rad}} = \varepsilon\sigma A(T_{\text{m}}^4 - T_{\text{surr}}^4)$ [119]. Here, σ represents the Stefan-Boltzmann constant, and we use room temperature for the surrounding and ambient air temperatures ($T_{\text{surr}} = T_{\infty} = 303$ K), convection coefficient of $h = 2000$ W/m^2 K, and Cu emissivity of $\varepsilon = 0.07$ [122]. Lastly, specific heat capacity, $c = 385$ J/kg K and density $\rho = 8960$ kg/m^{-3} of Cu are used for the calculation of the stored thermal energy change, i.e., $\Delta E_{\text{st}} = \rho Vc(\partial T_{\text{m}}/\partial t)$, where V is the control volume of nodal point m.

Two-Temperature Model for 1-D Nanowire With a short pulse of high-intensity laser irradiation, nonequilibrium between electron and lattice systems dynamically changes, and to address this nonequilibrium dynamics, electron and lattice temperatures of CuNW (T_{e} and T_{l}) are separately calculated. As in the analysis of CW laser, 1-D model and FDM are employed, but for each nodal point, the thermal energy balances for electron and lattice are considered, given by [13]:

$$\text{for electron } T_{\text{e}},\ Q_{\text{laser}} - Q_{\text{el}\to\text{latt}} + Q_{\text{el,cond}} = \Delta E_{\text{el}}, \text{ and} \tag{1.3.24}$$

$$\text{for lattice } T_{\text{l}},\ Q_{\text{el}\to\text{latt}} + Q_{\text{latt,cond}} - Q_{\text{conv}} - Q_{\text{rad}} = \Delta E_{\text{latt}}. \tag{1.3.25}$$

Here, the laser heat addition ($Q_{\text{laser}} = q_{\text{in}}\beta A$) is applied to the first node as in the CW laser simulation but considered only in T_{e} analysis [13, 123]. At the wavelength of FS laser (1030 nm), β has been reported as 0.06 [121]. During a pulse with 300 fs of duration, we assume a constant laser heat flux, $q_{\text{in}} = 1.77 \times 10^{17}$ W/m^2, which ensures the employed average power of FS laser (5 mW) considering 1 μm of laser

beam diameter and 120 kHz of pulse repetition rate. Heat flow from electron to the lattice, $Q_{el \rightarrow latt}$ is calculated using the electron-lattice coupling coefficient (g, W/m^3 K) from the literature [124] and the difference between T_e and T_l, i.e., $Q_{el \rightarrow latt} = gV(T_e - T_l)$. Conduction heat flow and stored thermal energy change for electron and lattice [$Q_{el,cond}$ and ΔE_{el} in (2) and $Q_{latt,cond}$ and ΔE_{latt} in (3)] are calculated using the electron thermal conductivity, $k_e = 385$ W/m K, lattice thermal conductivity, $k_l = 17$ W/m K, [125] temperature-dependent electron volumetric heat capacity C_e (J/m^3 K) from [124] and lattice volumetric heat capacity, $C_l = 3.45 \times 10^6$ J/m^3 K for Cu [125]. Convection and radiation (Q_{conv} and Q_{rad}) are included in the T_l analysis only and calculated as the single-temperature modeling using the same properties.

Figure 1.24 shows SEM images of laser-irradiated CuNWs under different processing conditions. Two kinds of laser beams, either a 130 fs pulse laser or 532 nm continue wavelength green laser, was focused by a long working distance 100× microscope lens with an NA of 0.8. After focusing, the diameter of the laser beam spot applied to the substrate was around 1 μm. The experiments were accomplished at room temperature and ambient atmosphere. Figure 1.24a-represent an experiment result for FS laser with an average laser power of 35 mW and Fig. 1.24d–f represent experiment results for CW laser at the same average power of 35 mW. Obviously, at the same average laser power, two laser irradiations create significant differences. For the FS laser, explosive deformations can be observed on both substrate and CuNW after the laser process by comparing Fig. 1.24a–c. The silicon wafer substrate is damaged, and a large number of Si and Ag nanoparticles splash around in the vicinity of the irradiation area (about ten micrometers). A large particles-aggregation appears on top of the NW. However, there is no structural and surface deformation on other parts of the nanowire. On the other hand, at the same laser power condition, the CW laser produced a different effect from that with the FS laser. Comparing Fig. 1.24d, e,

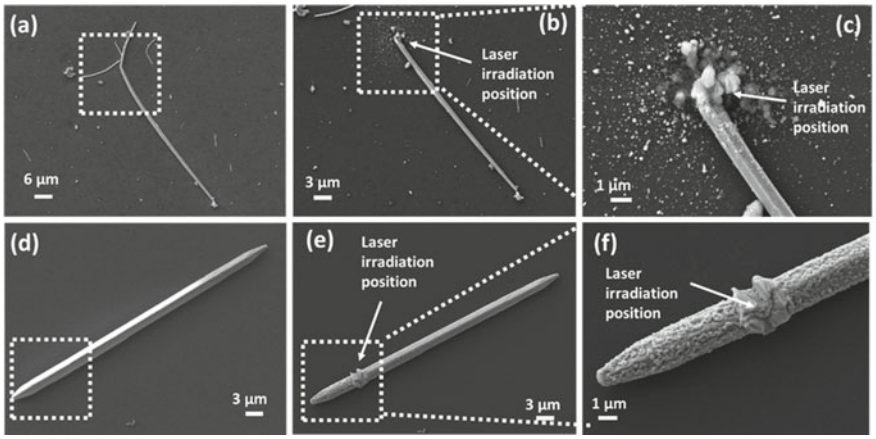

Fig. 1.24 SEM images of CuNW **a** before and **b** after FS laser irradiation, and **c** enlarged image of FS laser irradiation area. CuNW images (**d**) before and (**e**) after CW laser irradiation and **f** enlarged image of the CW laser irradiation area [6]

CW laser cannot break a CuNW at all but create a very clear surface deformation on the nanowire. As shown in Fig. 1.24f, at the laser-focused position, CuNW is partially melted at high temperatures induced by laser irradiation, and then the melted wire solidifies and crystalizes again after the laser is off. Furthermore, this thermal effect is propagated along the CuNW, and cause the increase of surface roughness of the entire nanowire (see Fig. 1.24f). In a sharp contrast, the surface of the un-irradiated area is kept as clean and smooth before and after FS laser irradiation. However, after CW laser irradiation, a clear surface change can be observed even in the un-irradiation area. Because the CuNW was exposed to air, serious oxidation could occur on the surface due to the heat-induced by CW laser, which will be further confirmed by the chemical analysis later. This oxidization has been confirmed by checking the oxygen distribution before and after the CW laser irradiation [6]. FS laser is an ultrafast high repetition pulse laser, with an average laser power of 35 mW, it can generate a peak power density of 1.24×10^{14} W/cm^2. On the other hand, with 35mW power, CW laser only generates a power density of 4.46×10^6 W/cm^2. Meanwhile, from the aforementioned theoretical analysis, for an ultrafast interaction, the absorption of photons stimulates electrons within a hundred femtoseconds (fs), which is too short to disturb lattice. The absorbed energy was thus transferred from electrons to the lattice by electron-lattice scattering after the laser pulse [13, 14]. The thermal coupling between free electrons and lattices typically occurs within 100 ps, depending on the electron-phonon coupling strength of different materials. The typical electron-phonon coupling time of hundred femtoseconds is much shorter than the heat transfer period by thermal conduction. Therefore, the thermal diffusion to the laser-irradiated surrounding area for a FS laser is very limited [15].

According to our computational simulations [6] with the CW laser (35 mW) irradiation (at $x = 0$), heat is accumulated, increasing temperature of CuNW with heating time (t), and the heat is dissipated along the length of CuNW (i.e., in the x-direction) in a nanosecond scale, as shown in Fig. 1.25a. With the CW laser heating longer than 0.5 μs, the temperature rises beyond the Cu melting point ($T_{\mathrm{m,Cu}} =$ 1368 K [126]), and a large portion of CuNW has a temperature above the oxidation temperature (1073 K) [127, 128]. Figure 1.25b displays that the thermally affected zone (i.e., the heated portion of the CuNW where the temperature is above the oxidation temperature) extends to 10 μm after 1 μs of heating time. It can be inferred that with the increase of irradiation time, the whole CuNW will be heated above the oxidation temperature. This explains that the oxidization of the entire CuNW with a CW laser observed from the experiment conducted in an ambient atmosphere in our study.

With the FS pulse laser irradiation at $x = 0$, the electron temperature (T_e) reaches a very high peak value (~27.5×10^4 K) within the pulse duration (~300 fs), and then it decays rapidly, releasing their energy to phonons (or lattice). The electron-lattice interaction causes the rise of local T_l [129], and T_e reaches almost equilibrium with T_l shortly (<20 ps) after the pulse at $x = 0$ (Fig. 1.25c). The lattice temperature (T_l) rises and decreases, and for most of the wire (>27 μm), it stays below the Cu melting point (Fig. 1.25d). A non-thermal ablation is expected at the beginning of the irradiated zone (<1 μm, close to the focus spot size) as the lattice temperature

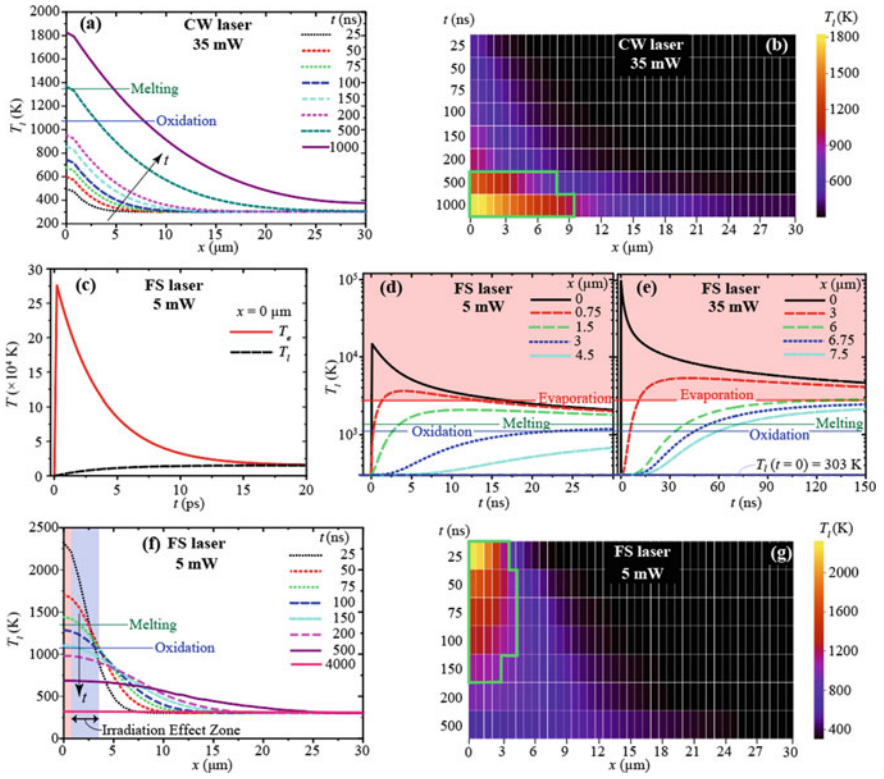

Fig. 1.25 **a** Temperature distribution and **b** heatmap of a modeled CuNW with respect to the distance from the heating area (x; the length direction) at a different heating time (t) when using the CW laser irradiation. **c** Electron and lattice temperatures of the first nodal point (T_e and T_l at $x = 0$) in a short time period after the FS laser pulse (with an average power of 5 mW) starts (< 20 ps). Time evolution of lattice temperature (T_l) from the beginning of a laser pulse (300 fs) at five different locations (i.e., $x = 0$, 0.75, 1.5, 3.0, and 4.5 μm) of CuNW with average FS laser power of **d** 5 mW and **e** 35 mW. (f) Temperature distribution and **g** heatmap of CuNW in the x-direction at different t when using the FS laser with 5 mW average power. The regions surrounded by green lines in (**b**) and (**f**) are above the oxidation temperature and vulnerable to oxidation [6]

is above the evaporation temperature of Cu (T_{ev} = 2840.15 K [130]), as shown in Fig. 1.25d. It is important to point out that such heat is very localized and maintained in a very short time period; T_l can be above the melting point less than 100 ns only near the heating region (x < 3 μm). FS laser irradiation with an average power of 35 mW as in the CW laser is expected to induce ablation of the much larger area, as Fig. 1.25e shows up to 6 μm of CuNW with a higher temperature than T_{ev}. With an average power of 5 mW, T_l drops below the oxidation temperature in 150 ns after a laser pulse, and the entire CuNW will be cooled close to room temperature before the next laser pulse comes (t = 8.33 μs with 120 kHz), as indicated by Figs. 1.25f, g. As T_l is maintained below the oxidation temperature in most regions (x > 4 μm),

we expect no significant oxidation even the experiment is conducted in an ambient atmosphere [6]. Even if thermal melting and oxidation exist, they are limited to a very local region (near the irradiated region) less than 3 μm. This simulation result is identical to the experiments, indicating that FS laser irradiation effect zones are about 2.5–4 μm with different laser powers [6].

In summary, computational simulations using 1-D heat diffusion equation and finite difference method (FDM) were performed to gain an insight into metal-laser interactions with different lasers. Simulation studies on lasers have established contrasting melting behaviors of metal under laser irradiations, which may pave the way to use the ultrashort laser for innovative nonthermal welding of nanowires and relevant devices development.

1.4.3 Photonic Reduction

Photonic reduction of metal salt has been developed as an effective method to form metal nanoparticles. The morphology of metal nanoparticles can be controlled by the various photonic parameters, such as, intensity, frequency, pulse width and polarization, etc. Generally, the photonic reduction of metal salt is realized by single-photon and two/multiphoton absorption induced photochemical reaction.

Single-photon Reduction and Two/Multiphoton Reduction For metal salt solution, the energy of a single photon in near-ultraviolet (3.11–6 eV), visible (3.11–1.78 eV) and infrared region (<1.78 eV) is not enough to photodecomposition of water (>6.5 eV) leading to the production of e^- to reduce metal ions [131]. Therefore, reducing reagent is needed for reducing reaction. As one typical reducing agent for silver salt reduction, citrate is extensively used for the synthesis of silver nanoparticles [132]. The process of photoreduction on silver ions by citrate is known as,

$$\text{Citrate} \xrightarrow{h\nu} \text{acetone} - 1, 3 \text{ - dicarboxylate} + CO_2 + e^-$$
$$Ag^+ + e^- \rightarrow Ag^0$$

In addition, small silver clusters Ag_n ($n = 2$–8) could be formed by continuous photoreduction,

$$\text{Citrate} + Ag_n \xrightarrow{h\nu} \text{acetone - 1, 3 - dicarboxylate} + CO_2 + Ag_n^-$$
$$Ag_n^- + Ag^+ \rightarrow Ag_{n+1}$$

By inducing the reducing agent, the metal ions may be also reduced by a photothermal effect. For example, the copper ions can be reduced by ethylene glycol during laser irradiation. The temperature of copper precursor increases to 250 °C by laser irradiation, which will result in the ethylene glycol decomposes into acetaldehyde [133]. The –CHO group of acetaldehyde can reduce the copper ions to

copper.

$$
\begin{aligned}
&2\mathrm{HO(CH_2)2} \xrightarrow{-\mathrm{H_2O}} 2\mathrm{C_2H_4O} \\
&\xrightarrow{\mathrm{Cu(OH)(NO_3)}} \mathrm{C_4H_6O_2} + 2\mathrm{H^+} + 2\mathrm{e^-} + \mathrm{Cu^{2+}} + \mathrm{OH^-} + \mathrm{NO_3^-} \\
&\rightarrow \mathrm{C_4H_6O_2} + \mathrm{Cu} + \mathrm{H_2O} + \mathrm{HNO_3} \\
&\rightarrow \mathrm{C_4H_6O_2} + \mathrm{Cu} + \frac{1}{2}\mathrm{H_2O} + \mathrm{NO_2} + \frac{1}{4}\mathrm{O_2}
\end{aligned}
$$

There are lots of reducing reagents suitable for different ion reduction. The reduction potential will gradually increase from ethylene glycol, polyvinylpyrrolidone (PVP), sodium citrate, ascorbic acid, sodium hypophosphite, sodium boron hydrate, and hydrazine hydrate. For a higher reduction potential, a lower temperature is required for reduction. On the other hand, some polymers can work as the capping layer to protect nanoparticles or limit the crystal growth in a certain direction and thereby to control the nanocrystal orientation. The experiments show that PVP is easily absorbed onto the (110) plane, while poly(methacrylic acid) (PMAA) and poly(acrylic acid) (PAA) tend to attach to (111) and (100) planes, respectively. Therefore, it is widely to use PVP with different molecule masses to grow silver nanowires [101] and nanoplane [95]. Ethan et al. have successfully grown (100) silver nanoplates with PMAA [134] and silver nanowire with nanodisc piling chains has been fabricated with PAA [135].

If the photon intensity is high enough to trigger two/multiphoton absorption, the metal salt can be converted to metal nanoparticles by photoreduction without any reducing agent [136]. Solvated electrons can be generated through a double photon excitation. This transient electron can reduce silver ions [137]. Furthermore, at the focal spot of a tightly focused laser beam, the energy absorbed during the transition (three-photon absorption) can exceed 7 eV. The water is photodecomposed and produces e^-, OH• and H• radicals. The metal ions can be therefore reduced to their zero valence state,

$$
\begin{aligned}
&\mathrm{Ag^+} + \mathrm{e^-} \rightarrow \mathrm{Ag^0} \\
&\mathrm{Ag^+} + \mathrm{H} \rightarrow \mathrm{Ag^0} + \mathrm{H^+}
\end{aligned}
$$

However, the efficiency of the photodecomposition of water is very low that only ~10% of silver ions can be reduced after 1 h [131]. It should be noted that the photon energy should surpass the threshold of multiphoton absorption which means high energy density is needed. It indicates that for laser processing, the multiphoton absorption usually occurs at an area in the center of beam focal spot. Therefore, the size of the reactive area may smaller than the focus spot, which may fabricate quantum dots with a size smaller than the optical diffraction.

Selectivity of Photonic Reduction for Wavelength Interestingly, the shape of nanoparticles synthesized by photonic reduction can be controlled by different wavelength illumination. Typically, the shape of nanoparticles is a sphere under

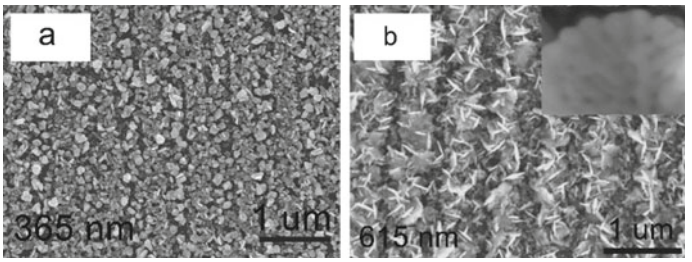

Fig. 1.26 SEM images of Ag film photoreduced by **a** 365 nm light and (**b**) 615 nm light [132]

short-wavelength illumination (Fig. 1.26a). In opposite, the shape of nanoparticles converted to a plate (disk) under long-wavelength illumination (Fig. 1.26b).

This phenomenon can be explained by the surface plasmon-enhanced photonic reduction. Briefly, in the case of short-wavelength illumination, the surface plasmon mode is dominantly transverse. Thus, short-wavelength light acts as feedback irradiation making the particle grow spherical. Conversely, as the longitudinal plasmon absorbs the longer wavelength irradiation more strongly, this longer particle axis grows preferentially, resulting in a plate-like shape [138].

1.4.4 Laser Direct Writing and Interference Lithography

Laser Direct Writing Laser direct writing provides high flexibility with non-contact and maskless fabrication processes, which significantly reduces the fabrication cost. Since laser direct writing can achieve a one-step fabrication combing local processing with patterning, the manufacturing efficiency is significantly enhanced. Figure 1.27 shows one schematic for laser direct writing setup. The setup has four basic elements to realize direct writing, including laser source, beam expander, focus lens (objective

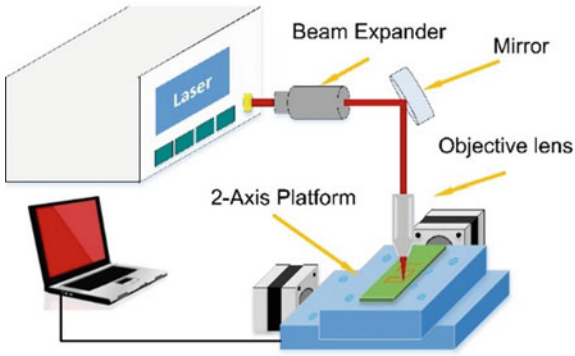

Fig. 1.27 Schematic for laser direct writing setup

lens), and translation motorized stage (multi-axis platform). Using high numerical - aperture objective lens and piezo stage stages, laser direct wiring have the fabrication resolution down to the sub-micrometer dimension.

Laser Interference Lithography Although laser direct writing has advantages as the aforementioned, laser interference lithography is suitable for the fabrication of periodic pattern due to high fabrication efficiency. Figure 1.28 shows a schematic of laser interference lithography setup using two inferred beams split by a beam splitter and the SEM image of periodic metal nanoparticle array fabricated by laser interference lithography. The period of interference pattern fabricated by laser interference lithography can be calculated by the following:

$$p = \frac{\lambda/2}{\sin(\theta)}$$

where P is the period of the interference pattern, λ is the laser wavelength and θ is the angle of the two interference beams. Also, by controlling the laser parameters such as beam intensity, the number of inferred beam and phase of a wavefront, periodic nanodots, and nanopolygon array can be fabricated by laser interference lithography. For multibeam interference lithography, the interference pattern can be calculated by the following equations:

$$I(x, y, z) = \int \left| \sum_{n=1,2,3....}^{N} E_n(E_{n0}, x, y, z, k_n, \theta_{\text{int}}, \varphi_n, \omega_n, \alpha_n, t) \right|^2 \mathrm{d}t \qquad (1.3.26)$$

where n is the number of laser beams, θ_{int} is the polar angle, φ is the azimuthal angle, α is the phase shift. For example, Fig. 1.29 shows the interference pattern at $\alpha = 0$ and $\alpha = \pi$, which indicates the shape of the pattern is ring and square, respectively [140]

It is worth mentioning that another method to fabricate periodic structure by laser is the laser-induced periodic surface structure (LIPSS). The orientation of the periodic structure of LIPSS is perpendicular/parallel (based on the fabrication conditions) to the laser polarization. Therefore, the two-dimensional periodic nanostructure can

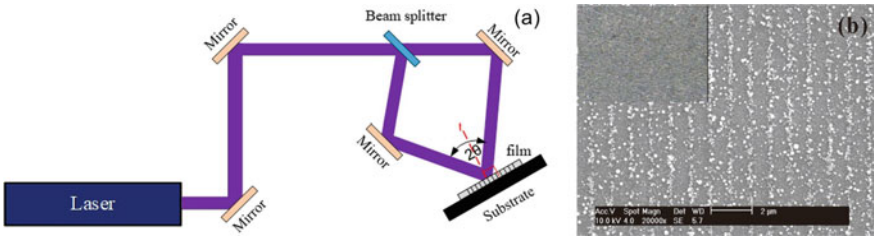

Fig. 1.28 **a** Schematic of laser interference lithography setup and **b** SEM images of periodic metal nanoparticle array fabricated by laser interference lithography [139]

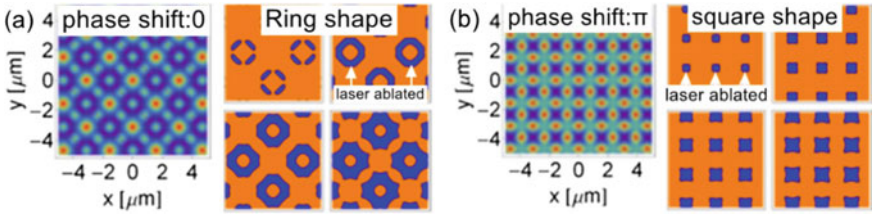

Fig. 1.29 Interference patterns as the phase shift. **a** 0 and **b** π using laser interference lithography (Figure adapted from [140])

be fabricated by orthogonally double laser exposure [141]. Such a nanostructure is successfully used for in situ on-line real-time pollutant monitoring of water.

1.4.5 Laser Ablation, Trimming, and Drilling

Extreme conditions, such as a high-temperature and high-pressure plasma state, generated by laser provide unique access to materials science and manufacturing. New materials and new phases synthesized via femtosecond laser-induced micro-explosions have appeared as a very attractive research topic [142]. As aforementioned procedure of Sect. 1.1.2, electron ejection due to ultrafast laser-matter interaction will lead to a Coulomb explosion of positively charged ions after laser-induced vaporization of electrons [4, 16]. This Coulomb explosion is confined in a microscale space in the vicinity of the focal spot. High-temperature and high-pressure conditions can thus be used for the synthesis of new materials. Hu reported that *sp*-bonded carbon chains (polyyne) can be formed on a graphite surface using femtosecond laser irradiation associated with the formation of amorphous tetrahedral carbon (diamond-like carbon) [16]. This *sp*-bonded carbon chain species can be precursors for various carbon allotropes, including carbon nanotubes, fullerenes, and carbynes [143]. Rapp reported a new tetragonal polymorph of silicon induced by confined microexplosions [144]. On the other hand, this Coulomb explosion can also occur in a liquid by focusing femtosecond into an organic solvent. Polyyne molecules are evident in such an environment [143, 145, 146]. However, polyyne molecules are unstable in a laser-thermal conduction, thus a nonthermal interaction induced by femtosecond is favorited for polyyne synthesis. Moreover, the mechanical shock wave induced by fs laser pulses can be used as a powerful surface peening tool for metals [147]. Femtosecond laser peening research without using a sacrificed layer was motivated by the process simplicity and localized shock pressure attainable with fs pulses in comparison to ns laser peening. More recently, strengthened mechanical properties in terms of high compressive residual stress and hardness enhancement were reported in fs laser peening of aluminum [148] and steel [149] free from a protective coating and a transparent overlay. Hence, it can be said that ultrafast laser is innovative for

materials synthesis and surface engineering but more research is needed in these directions.

Femtosecond laser-induced water spliting and coal gasification have been reported for facile synthesis of porous graphene and graphene quantum dots [150, 151]. The underlying dynamics is not yet established but taking a critical role for large scale synthesis of quantum dots. Femtosecond laser direct writing is also employed for device fabrication though the laser-induced reduction of graphene oxide. The reduction should be correlated to both the photonic thermal effect and multiphotonic absorption [98]. Recently we studied laser trimming of alloy stripes with femtosecond laser and nanosecond pulsed laser. The precision cutting for precisive resistance adjustment is realized by femtosecond laser trimming [152].

Multiphoton absorption of ultrafast laser is extensively used for drilling high aspect ratio microchannel or holes in transparent materials which the linear absorption is limited [1]. Recently we reported the microball lens by forming the microcavity in polymer [21]. Shown in Fig. 1.30, a wide angle imaging is demonstrated with

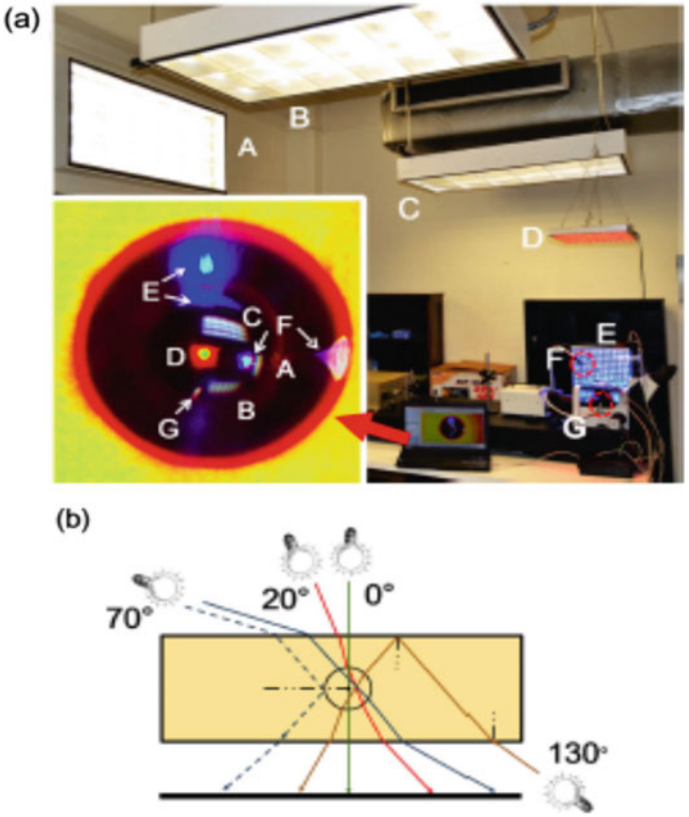

Fig. 1.30 Super-wide imaging by cavity microball lens. **a** Super-wide imaging taken by an inverted microscope. **b** Schematic for the super-angle-imaging of embedded microball lens [21, 153]

a micro-cavity ball lens combined with an inverter microscope. The photothermal modified optical index convex lens is also formed by precisely controlling laser power [153].

1.5 Micro-to-Nano Manipulation

The size effect and the scaling law make the nanoworld is quite different from the micro- and macroworld. Shown in Fig. 1.31, the volume force, such as gravity, scaling to L^3 will be negligible at microscale by compared to surface forces, scaling to L^2, like electrostatic force and pressure and friction force. The manipulation operating in the macroworld cannot thus work for a microscopic assembly. Furthermore, the linear force, such as surface tension is much stronger than a surface force. Therefore, a microtool cannot be used for a nanomanipulation. As a result, nanoscopic assembly methods have to be developed before a nanomanufacturing can be implemented.

In vacuum and/or ambient atmosphere, a metallic tip, such as a tungsten tip, is usually used for manipulating a microscale building block. However, for a nanomaterial, certain attachment-detachment procedures are required. For example, to prepare a TEM sample preparing by focused ion beam (FIB), the cut piece has to attach to the tip by the first deposition a carbon film to join the TEM sample and tip together, and then the separation of them by cutting carbon film by FIB again after the tip displacement with a 3D programmed platform. Cox et al. used this method to construct an "ATI" logo with carbon nanotubes [154].

Magnetic force allows the manipulation and orientation in both air and liquid environment without contacting. The magnetic force acting on a nanoparticle can be expressed as

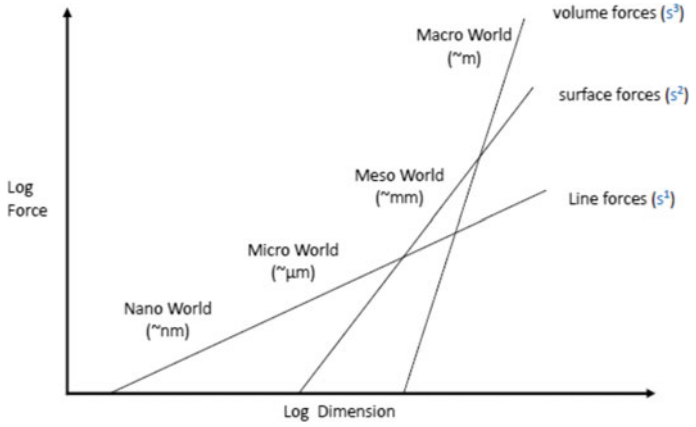

Fig. 1.31 Scaling laws of different forces at macro-, meso-, micro- and nanoworld

$$F_{\mathrm{m}} = V_{\mathrm{m}} \Delta\chi \nabla \left(\frac{1}{2} B \cdot H \right) \tag{1.4.1}$$

where the $\frac{1}{2} B \cdot H$ is the energy density of the magnetic field, V_{m} is the volume of the particle, $\Delta\chi$ is the effective susceptibility of the particle (assumed in water), if > 0, the magnetic force will cause the displacement of a nanoparticle. For placing a nanowire in a uniform magnetic field, the torque $_{\mathrm{m}}$ acted on the nanowire can be expressed as [155]

$$\tau_{\mathrm{m}} = m \times H = M_s \pi r^2 H L \sin\theta_l \tag{1.4.2}$$

where M_{s} is the saturation magnetization and m is the magnetic moment of the nanowire, $_{\mathrm{L}}$ is the angle between the nanowire and the magnetic field. The friction torque generated by liquid can be calculated through the following equation [155],

$$\tau_{\mathrm{d}} = \frac{1}{3} \omega_{\mathrm{w}} \pi \eta L^3 C \tag{1.4.3}$$

where $_{\mathrm{w}}$ is the angular rotation speed, C is the geometric factor. Then the rotation equation of nanowire driven by the magnetic field can be written by

$$I \alpha_{\mathrm{w}}(t) = \tau_{\mathrm{m}} - \tau_{\mathrm{d}} \tag{1.4.4}$$

where the a_{w} is the mass density of nanowire and I is the moment of inertia of nanowire.

In liquid optical tweezer is one popular tool for micromanipulation. In principle, optical tweezers generate forces by the optical gradient field. At the vicinity of the focal point, two forces will be generated: pick-up force $F\ \nabla$ and scattering force F_{s} [156].

$$F_{\nabla} = 2\pi a^3 \frac{\sqrt{\varepsilon_0}}{c} \left(\frac{\varepsilon - \varepsilon_0}{\varepsilon + 2\varepsilon_0} \right) \nabla |S| \tag{1.4.5}$$

$$F_{\mathrm{s}} = \frac{8}{3} \pi (ka)^4 a^2 \frac{\sqrt{\varepsilon_0}}{c} \left(\frac{\varepsilon - \varepsilon_0}{\varepsilon + 2\varepsilon_0} \right)^2 \mathrm{S} \tag{1.4.6}$$

where the s is Poynting vector, $s = 1/\mathrm{ExB}$, ε, and ε_0 are the dielectric coefficients of the particle and the medium, a is the particle diameter. $F_{\bigtriangledown}$ is scaling to a^3 and F_{s} scaling to a^6. At the microsize, F_{d} will be larger than F_{s}. A microscale building block is easily entrapped by a focal light. However, at a nanoscale, $F_{\bigtriangledown}$ will decrease rapidly and therefore, cannot effectively grasp a nanoparticle. For a nanoparticle, a near-field plasmonic tweezer has been developed [157], where the surface plasmonic field provides an entrapped force to grasp a metallic nanoparticle. However, optical tweezer, as a non-contact tool, is very practical for cell manipulation and other biomedical applications. To grasp a nanowire, a multipoint optical tweezer is invented

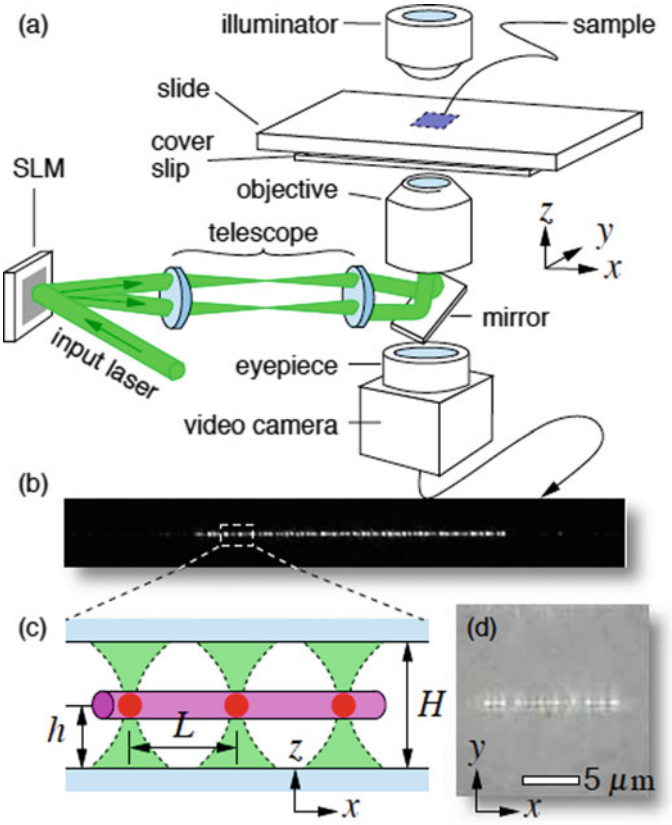

Fig. 1.32 Multifocal point optical tweezer (Reprinted with permission from [156] ©The Optical Society)

[156]. Shown in Fig. 1.32, through splitting light into a multibeam using a liquid crystal mirror and then focus several points onto a nanowire, a nanowire can be effectively picked up [156]. Through synchronously rotating the focal points the nanowire can be rotated.

Electric interaction is another popular tool for manipulation in liquid. For charged ions, the DC (direct current) electrical field will directly drive the displacement of ions. However, for a charged particle suspended in an electrolyte solution (Fig. 1.33), the electrical double layer phenomenon will make it similar to a neutral particle. According to the Stern model, the zeta potential can be expressed as

$\zeta = \varphi(z)e^{\kappa z}$, where the $\kappa$is a constant relevant to the electrical double layer thickness, which at least spreading over a Debye length λ_D.

$$\lambda_D = \kappa^{-1} = \sqrt{\frac{\varepsilon_d \kappa_B T}{\sum_i q_i^2 c_i^2}} \tag{1.4.7}$$

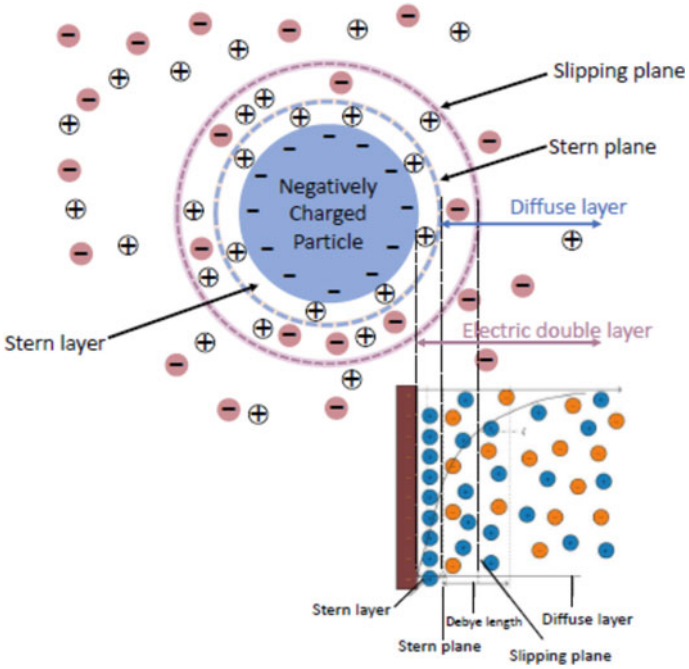

Fig. 1.33 Electrical double layers around a charged particle in an electrolyte solution

where $_{d}$ is the dielectric permittivity of the solution, K_B is the Boltzmann constant, q_i is the electrolyte charge, C_i is the concentration of electrolyte. For pure water, $_{D}$ is about 700 nm but in salted water, the double layer can be as thin as 10 nm. When the charged particle, the associated electrical double layer structure will move accordingly, the effective mass of the charged particle thus significantly increases. In this case, the dielectric interaction between the electrical field and electrical dipolar moment of particles will result in a driving force. Dielectrokinetics results in three kinds of effects: dielectrophoresis (DEP), electro-osmosis (EO), and electrothermal effect (ET). Because the electrical field can be generated by either DC (direct current) or AC (alternative) current source, electrokinetics can respectively be DCEK and ACEK. DCEK requires a high voltage to drive electrokinetic flow, an electrochemical reaction or a bubble can be easily formed in liquid during DCEK. In contrast, ACEK induced changes of fluidic polarity and thus effectively drive the transporting of liquid and suspended particles. ACK is thus extensively employed for manipulation.

For a DEP, a force will exert on a dielectric particle when it is subjected to a non-uniform electrical field. This force does not require the particle to be charged. All particles exhibit dielectrophoretic activity in the presence of electric fields. However, the strength of the force depends strongly on the medium and particles' electrical properties, on the particles' shape and size, as well as on the frequency of the electric field. Shown in Fig. 1.34, DEP force in a conducting dielectric medium can be written

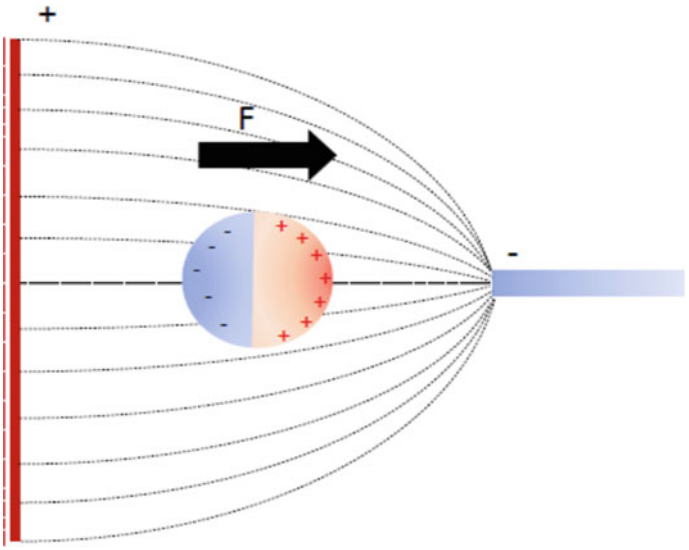

Fig. 1.34 Dielectrical forces acting on a particle in an electrical field

as

$$F_{\mathrm{DEP}} = \pi r^2 l \varepsilon_{\mathrm{m}} k(\omega) \left(\vec{E}_{\mathrm{r}} \cdot \nabla \vec{E}_{\mathrm{r}} \right) = \pi r^2 l \varepsilon_{\mathrm{m}} k(\omega) \nabla |E_{\mathrm{r}}| \tag{1.4.8}$$

$$k(\omega) = \mathrm{Re}\left[\frac{\varepsilon_{\mathrm{n}}^* - \varepsilon_{\mathrm{m}}^*}{\varepsilon_{\mathrm{m}}^*} \right] \tag{1.4.9}$$

$$\varepsilon^* = \varepsilon - i \frac{\sigma}{\omega} \tag{1.4.10}$$

where $\varepsilon_{\mathrm{n}}^*$ is the complex permittivity of particle and $\varepsilon_{\mathrm{m}}^*$ is for medium, ε is the dielectric constant, σ is electrical conductivity and ω is the field frequency, E_{r} is the root mean square of the external excitation field E. For a positive DEP, the particle will move toward to high field region and the negative DEP drives the particle to move away from high field region. In our recent works [6], both Cu nanowires and T_{e} nanowires are aligned by DEP at a certain frequency range and voltage.

ACEO is a phenomenon of induced-charge electro-osmosis of liquid, where the fluidic flow is generated by the action of an electric field on its induced ion diffusion near a polarizable surface. The ion's attachment and accumulation to the electrode surface will cause the capacitance change. Thus, ACEO is extensively used for sensing in liquid [158].

Since ACEO is caused by the counter-ions migration with or against the electric field, which produces fluidic motion due to fluidic viscosity, it is expected that the fluidic flow velocity will keep changing due to the ion migration. At a low

applied voltage (<100 mV), the time-average displacement of ACEO as a function of frequency can be expressed as

$$u \propto \frac{\varepsilon V^2}{\eta(1+\delta)L\left[\frac{\omega}{\omega_c}+\frac{\omega_c}{\omega}\right]^2} \tag{1.4.10}$$

where η is the viscosity of the fluid, ε is the permittivity of fluid, V is the applied voltage, L electrode spacing, δ is the ratio of the diffuse-layer to compact-layer capacitances (both assumed constant). The peak frequency is at the scale of the RC charging time

$$\omega_c \propto \frac{D(1+\delta)}{\lambda L} \tag{1.4.11}$$

where λ is the Debye screening length and D is a characteristic ionic diffusivity. At a high voltage, a Faradic charging occurs at the particle surface [159]. The aforementioned model is not appropriated. ACEO has applied to manipulate the microparticle and cells [160]. The application of ACEO for nanomanipulation is still unclear.

ACET refers to fluid motion resulting from temperature gradients in the fluid induced by an AC electric field. The fluid velocity based on the thermal gradient [160, 161] can be expressed as

$$|u| \approx 3 \times 10^{-3}\left(\frac{\varepsilon V^2}{\eta\sigma}\right)\left(\frac{\partial T}{\partial y}\right) \tag{1.4.12}$$

where V is the voltage, σ is electrical conductivity, η is the viscosity of fluid, ε is permittivity of fluid and $\frac{\partial T}{\partial y}$ is the local thermal gradient along axis y. Unlike Joule heating, the ACET velocity has a quadratic relationship with voltage [162]. The electrothermal force can be expressed as below [163]

$$F_{ET} = \frac{1}{2}\frac{\varepsilon(\alpha-\beta)}{1+(\omega\tau)^2}(\nabla T \cdot E)E - \frac{1}{4}\varepsilon\alpha|E|^2\nabla T \tag{1.4.13}$$

where $\alpha = \frac{1}{\varepsilon}\left(\frac{\partial\varepsilon}{\partial T}\right)$, $\beta = \frac{1}{\sigma}\left(\frac{\partial\sigma}{\partial T}\right)$, is the angular frequency of the AC electrical field, and. For aqueous solutions and temperatures around 293 K, a and beta can be estimated as $-0.4\%\ \mathrm{K}^{-1}$ and $2\%\ \mathrm{K}^{-1}$, respectively [164]. Therefore, the aforementioned equation can be simplified as [165]

$$F_{ET} = -0.012 \cdot \frac{\varepsilon|E|^2}{1+(\omega\tau)^2} \cdot \nabla T - 0.001\nabla T \cdot \varepsilon|E|^2 \tag{1.4.14}$$

ACET is extensively applied in microsystems for mixing, pumping of fluids, and microparticles manipulation [166]. Nanoparticle manipulation and/or in a nanofluid is relatively less studied.

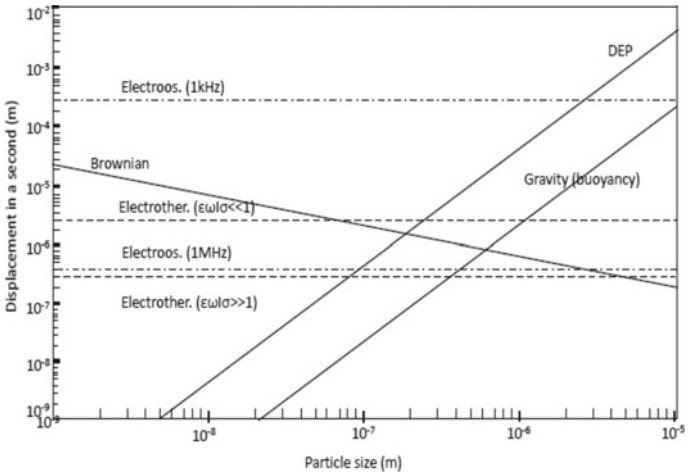

Fig. 1.35 Diagram of various motion mechanisms and forces in liquid [165]

Figure 1.35 displays various dielectric force versus gravity, buoyancy, and Brownian motion. For effective manipulation, DEP works for a microparticle or a nanowire with a length in micrometer. However, for a nanoparticle and/or quantum dots, ACEO is especially powerful to suppress the Brownian motion.

It is possible to combine an electrical field driving and an optical tweezer principle and form a so-called optoelectrical tweezer (OET). Shown in Fig. 1.36 is the principle of OET [167]. Light excises a transparent amorphous Si film and causes the increase of local conductivity. The local conductive Si electrode and transparent top-electrode form a 3D electric field for electrical driving. By scanning light, this field can be programmed and patterned for particle manipulation. Micro-and nano-robots become innovative tools for nanomanipulation.

Fig. 1.36 Principle of an optoelectrical tweezer [167]

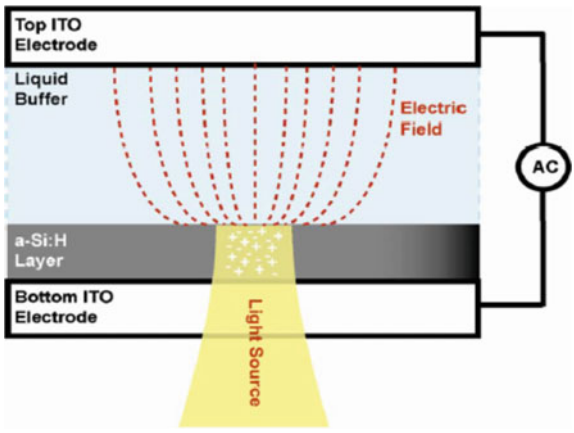

Numerical innovative methods have been investigated for particle manipulation. Microrobots have been proposed for manipulation [168]. It is facile to generate a microbubble by laser heat and use this bubble as a microrobot for particle manipulation [169]. Recently, such a microrobot has been demonstrated to enable 3D assembly of a micromechanical device [170]. Surface tension and LB methods are also used for nanowire alignment [76]. Large-area photonic crystal can be formed through self-assembly [171]. Laser-induced front transfer can be a powerful tool for nanomaterial transporting and manipulation. The last chapter of this book will focus on this method.

1.6 Nanojoining and Molecular Devices

1.6.1 Overview of Nanojoining

Welding of nanomaterials is essential manufacturing of functional nanoelectronics [172], including nanocircuits [173], light-gated nanowire transistors [174], nano waveguides and nanophotonic circuits and nanoplasmonic devices for quantum computation [5, 89, 175]. To realize a nanoscale joining, various methods have been developed to join nanomaterials, such as mechanical riveting [176, 177], mechanical pressure [178, 179], adhesive bonding [180, 181], cold welding [45, 47, 48], Joule heating [182–185], thermal annealing [95, 186–188], soldering and brazing [189–195], and laser (laser-induced plasmonic) welding [196–198].

Table 1.3 Various conventional joining methods versus nanojoining innovations

Conventional catalogue	Nanojoining
Mechanical joining	Mechanical clamping [176] Von der Waals force [177] Pressure [178, 179]
Adhesive joining	CNT/epoxy, polymer [180, 181]
Solid-state bonding	Diffusion/sintering/cold welding [47, 48] Electron/ion beam [199, 200] Ultrasonic welding [201]
Soldering/brazing	Resistance soldering [185] Active brazing [192] Self-powered brazing [195] Laser brazing [193] Vacuum brazing [194, 202] Transient liquid phase bonding [195]
Fusion welding	Resistance spot welding [182] Laser welding [196] Ultrafast nonthermal welding [6, 198]

Table 1.3 shows a comparison between conventional joining techniques and nanojoining innovations [41]. Solid-state diffusion driven by surface energy has enabled welding of two bare Au nanowires in vacuum at room temperature [47] and joining of two silver nanowires after removal of the surface-capping amorphous layer at an ambient atmosphere [48]. However, this solid-state diffusion is difficult to achieve joining with an arbitrary angle unless applying the external excitation energy, such as a head-to-side joining (T-shape) since the capping layer on the sidewall is thicker than the layer at the wire head [48]. Although the Joule heating was proposed to join metallic nanowires in case of contact wires [182, 183], the so-called nanoscopic resistance spot welding can be only applied to conductive nanowires. A mechanical pressing with nanoindentation was also developed to join nanowires to the substrate [178, 179]. Unfortunately, this press will significantly deform the wire head. On the other hand, the substrate can be also deformed seriously by Joule heating, mechanical pressure and thermal annealing unless the processing parameters, e.g., current, pressure, and temperature, are accurately controlled. Compared with these joining methods, photonic sintering was conducted for joining metal nanowires at arbitrary contact angles, which enables non-contact processing and good thermal management to minimize the damage of the substrate and nanomaterials. Due to self-localized plasmonic excitation [94], this plasmonic heat can lead to the perfect joining of adjacent and/or contact nanowires. A continuous-wave laser was reported to braze the crossed NWs [196], which is similar to autogenous laser brazing for metal microjoining [203]. However, laser joined metal NWs display a polycrystalline nature with lots of defects at the joined regions [88, 197, 204]. This is quite different from a self-oriented joining with solid-state diffusion where a clear lattice matching is founded. Femtosecond laser joining and a laser-healing of cutting wires has shown possible epitaxial recrystallization or enhanced grain orientation [88, 204, 205]. Therefore, precise control of laser parameters based on the understanding of the interaction of laser and nanowires is critical to improve nanojoining quality for innovative applications. As shown in Fig. 1.37, recent experiments by comparing femtosecond laser to continuous-wave laser and computation simulation and modeling have demonstrated

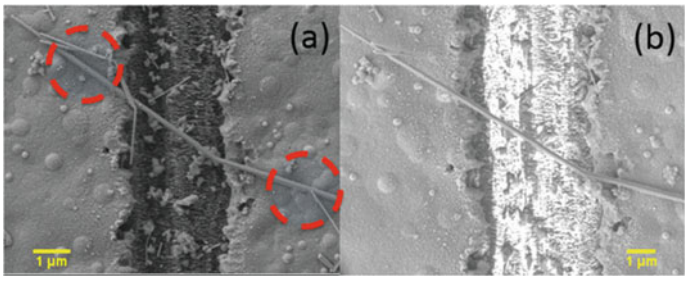

Fig. 1.37 Femtosecond laser joining of single Cu nanowire onto silver nanofilms printed by an aerosol printer [198]. The groove is cut by femtosecond laser. The groove width is 4 μm. **a** Before laser joining. Two dashed circles indicate the joining site. **b** After laser joining. The thin Cu nanowires indicated by circles in (**a**) were blown away by laser illumination

the success welding of metallic nanowires [6, 206]. However, the further work to join dissimilar nanowires, such as, metallic oxide nanowires still needs extensive research [197].

1.6.2 Molecular Electronics

Transistor, which is one of the essential components in integrated circuits, controls the flow of electrons by customizing the voltage that applied. In 2004 Ghost et al. predicted to realize an evolutional solid-state molecular transistor by the electrostatic regulation of the molecular orbital energy of a single molecule [207]. Electrostatic and conformational interactions are two possible mechanisms for field-effect molecular transistors. Electrostatic component leads to the thermal limit in the absence of tunneling. In their research, it shows that only if the molecular dipole moment μ is close to qt_{ox}, where t_{ox} represents the thickness of the oxide isolation layer, the conformational field effect can take a major role. Take advantage of that, if a large molecular dipole along a suitable direction is established, the conformational transition can be achieved. Soon after, Ahm et al. [208] have suggested another approach, in which internal electrostatic charge density can be adjusted by using an external node to control the charge transfer across the metal electrodes and the molecules. Transistor action can be achieved by aligning the molecular energy levels and the Fermi level of the leads. Remarkably, researchers have developed molecular transistors by gold nanowire wires [209]. In this research, an approximately 100 nm gold nanowire was patterned by electron beam lithography on top of an aluminum gate electrode. As an active device, a 1,4-benzenedithiol (BDT) with a delocalized aromatic ring as a π-conjugated molecule was coated on the gold nanowire surface, which acted as a channel material.

Diodes are another crucial component of integrated circuits that conduct current only in one direction when they are forward biased. Usually, a diode is composed of two kinds of semiconductor materials to form a P-N junction. Currently, two types of molecular diodes have been reported: rectifying diodes and resonant tunneling diodes. In 1974, Aviram and Rater discussed the possibility of a rectifier, which provided a foundation for current works on molecular rectifying diodes [210]. In their research, a donor π-system and an acceptor π-system linked by a σ-bonded tunneling bridge. This behavior has been identified by a hemi-quinone molecule, as shown in Fig. 1.38 [211]. For resonant tunneling diodes (RTD), electrons can pass through the resonant state at different energy levels; these diodes can be used as oscillators and switches [212]. For molecular RTDs, methylene groups or aliphatic groups are attached to both sides of a benzene ring, which leads to creating a potential barrier. To create a functional device, electrodes need to be able to pass through this potential barrier. However, the unoccupied energy level of the benzene ring does not match the energy level of the electrode. In this case, the transistor remains in the "off" state. The transistor can be turned to an "on" state, by varying the applied voltage [213]. To design a proper molecule device, computation modeling is facile and time-effective.

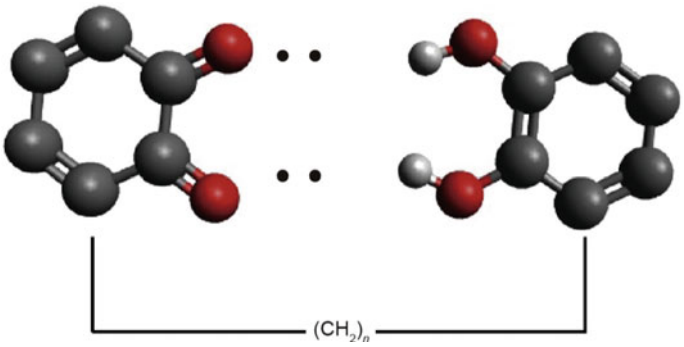

Fig. 1.38 a schematic of a hemi-quinone molecular structure [211]

Currently, the Hartree–Fock self-consistent field theory and the density functional theory (DFT) are two main theories used in developing a theoretical fundamental for molecular electronic devices.

Based on the concept of molecular electronic devices, molecular capacitors/memory units are developed as well. Jurow et al. have been reported a detailed review of porphyrins, which elucidated a potential for using these molecules in the fabrication of molecular capacitors [214]. Coming to molecular diodes and molecular transistors, molecular devices functional on dielectrics material and tunable dielectric constant are desired. In 2007, Chen et al. reported a hafnium dioxide (HfO_2) based metal-insulator-molecule-metal device [215]. A HfO_2 dielectric layer was deposited by an atomic layer deposition process. Although new studies provide an excellent potential for deployment of the molecular capacitor, current understanding of the molecular mechanism of the capacitor are not yet well experimentally established.

On the other hand, to establish a complete molecular electronic system, the development of molecular isolator and conductive wire is also necessary. For any integrated circuit, the isolator plays a significant role in regulating the flow of current. Many molecular with specific functional groups can be used as molecular insulator material. Currently, aliphatic organic molecular is considered as the best molecular insulator [216]. In aliphatic organic molecular, there are only σ bonds existing. By inserting these molecules between electrodes, it is very easy to break the pass current flow. Similar to the isolator, the concept of the molecular wire is crucial when dealing with the molecular electronics system. Different from molecular isolators, molecular wire requires high electrical conductivity. There are two primary types of molecular wires can be classified: saturated chains and conjugated chains [16, 217]. The main difference between the two chains is that whether atoms are connected with single bonds or connected by alternate single and double bonds [218]. In the development of molecular wire, CNTs are considered as a widely acceptable material [219].

1.6.3 1D (Nanowire and Nanotube) and 2D Material in Molecular Electrodes

1D and 2D materials are very promising building blocks for molecular electronics; especially, the carbon-based material plays a significant role in the design process and device fabrication. The first demonstration of carbon nanotubes (CNT) used in a field-effect transistor has been reported in 1998 [220]. A single wall CNT (SWCNT) was positioned on top to bridge two gold electrodes, which were fabricated on a SiO_2 film grown on a silicon wafer. Two gold electrodes act as source and drain electrodes, and the wafer itself was used as the gate electrode ("back-gate"). These CNT-FETs behaved as p-type FETs with ON/OFF current ratio of $\approx 10^5$ [221]. The further improvement of current conductance across the metal -molecule interface is a great technical challenge in a molecular transistor [222, 223]. It has been proved that the Schottky barrier between nanotube and metal contact leads to limit the current flow, which reduces molecular conductivity [224]. In terms of this issue, Javey et al. provided a valuable idea to reduce the barrier by placing a palladium contact with SWCNT [225]. The research shows that palladium has a high work function and an exceptional wetting interaction with CNTs, these properties can effectively reduce the contact resistance. Furthermore, metallic and semiconductor property of CNTs can be strengthened by controlling its geometric features during growth [226].

CNT has also become an indispensable material in other molecular devices. In 2004, Dragoman et al. discussed the possibility of using semi-conductive SWCNT for a molecular diode. As reported, the semi-conductive SWCNT yields better performance than the usual semiconductor hetero-structured RTD [227]. In their design, the barrier height was controlled by the DC voltage applied to the gate and the gap of intra-electrodes. Pandey et al. bridged pseudopeptide between two semi-conductive CNT and created a based molecular RTD (Fig. 1.39) [228]. As claimed in this system, no special bistable properties of the molecule are required and can exhibit longer reliability than bistable molecules, which is known as molecules that can be switched reversibly between two stages, such as magnetic [229], electrical properties [230], or optical properties [231]. Except for carbon-based materials, metal and metal oxide nanowire/nanotube-based 1D material have also been developed for molecular devices. In 2017 Madini et al. provide a new theoretical framework for molecular capacitor by introducing a single-walled boron nitride nanotube (SWBNNT) inside

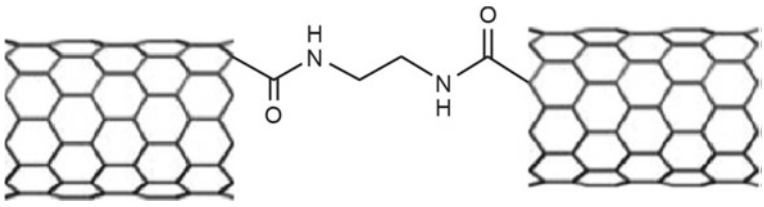

Fig. 1.39 Schematic of the CNT–pseudopeptide–CNT [228]

of anther SWBNNT [232]. Green et al. reported a 160-kilo-byte molecular electronic memory pattern, which fabricated by over 1400 Ti nanowires [233]. These molecular device patterns were configured to form a fully functional random-access memory circuit for storing and retrieving information.

Graphene is a typical 2D material providing valuable mechanical, electronic, chemical, and optical properties. At the same time, graphene is recognized as an ideal candidate for molecular junction [234, 235]. Wang et al. evident graphene as the ideal electrode through a comparative study to PEDOT:PSS and gold in molecular devices [235]. In their report, graphene has better transport characteristics and contact conductance. Nowadays, graphene is extensively applied in multiple molecular electric devices, such as conducting electrode in memory devices [236], field-effect transistors [236], and dye-sensitized solar cells [237].

1.6.4 Fabrication of Molecular Devices

In the process of molecular devices fabrication, pre-patterning, and precise manipulation of nanomaterials are required as very critical processes. Usually, e-beam lithography and chemical vapor deposition for in situ growth are the main tools for these procedures [238, 239]. With the development of molecular devices, some novel approaches have been established. As aforementioned the laser as a tool for precision machining has considerably contributed to the nanoscale process, such as laser-induced plasmonic nano joining [5, 6], nanoscale ablation [240], and etching [141, 241]. The precision machining property of laser processing has also been applied in molecular electrical devices as well. Maurice et al. reported a low-temperature process for nanogap creating in graphene [242]. In this study, a tightly focused femtosecond laser was used to induce a pre-patterned defect in graphene. After the laser process, an electro-burn process was applied to generate a gap with tens nanometer wide. During this process, the defected area could locally generate a dynamic hot spot, further facilitate the burn of graphene and eventually yield a nano-size gap. As a result, the nanogap width is 36.4 ± 18.5 nm (as presents in Fig. 1.40). A few nanometer gap as a basic architecture allows a single molecule to be inserted to create molecular transistors [243, 244], DNA sequencers [245, 246], and sensors [247]. Therefore, develop a nanogap fabrication process is essential in the field of molecular electronics.

Currently, the development of molecular electronics using DNA molecules as the building blocks or template for growth nanostructure has gained a huge interest. The key to using DNA as a scaffold for electronic circuits is to effectively transform the DNA molecules into conductive wires, which is called DNA metallization [248]. Typically, DNA-templated electronics is a two-step process; First, establish metallic nucleation centers on DNA molecules, which can be approached by binding metal ions or complexes to the DNA and their subsequent reduction, or by directly placing small metallic particles to the DNA. Once metallic nucleation centers were formed, using these centers as catalysts for selective deposition of metal along with

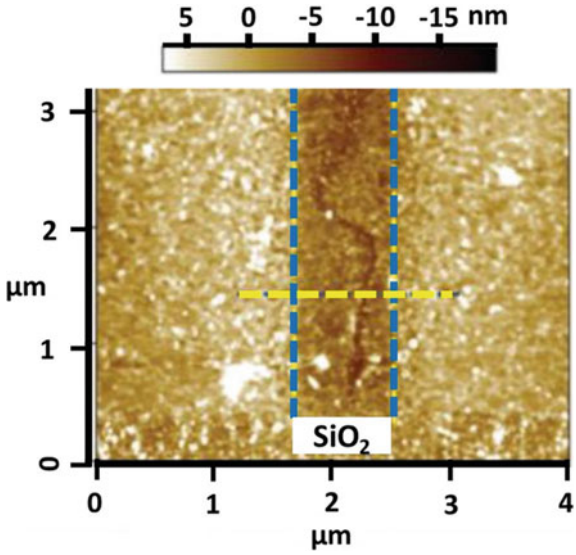

Fig. 1.40 AFM height image of a graphene device after laser pre-patterning and electroburning Modified from [242]

the DNA molecular template, which leads to creating a conductive metallic wire by bridging gaps between nucleation sites. Various metals have been employed including silver [249], palladium [250], platinum [251] and gold [252]. The disadvantage of this metallization method is the non-uniformity over the entire DNA scaffold. To address the uniformity problem, sequence-specific molecular lithography was further developed [253]. In molecular lithography, masks used in conventional photolithography is replaced by the information encoded in the DNA molecules. In 2003 Keran et al. reported a caritative process for assembly a CNT along with a pre-designed template on a DNA substrate [254]. In this research, a framework of using DNA and homologous genetic recombination for CNT self-assembly is established. By using homologous recombination, which is a protein-mediated reaction between two DNA molecules, a CNT was localized at a desired DNA scaffold molecule. *RecA* protein from *Escherichia coli* bacteria was used in the process. After CNT was localized, DNA molecule is metallized by $AgNO_3$. Conductive metallic wires were formed by silver reduction along the DNA. In here, *RecA* act as a protector to protects the active area of the transistor against metallization. Subsequently, electroless gold plating was applied using the silver clusters as nucleation centers to create a highly conductive gold electrode. Figure 1.41 shows an SEM image of an individual SWNT contacted by two DNA-templated gold nanowires.

Although current approaches of making DNA-templated wires have shown a promising development, it is still facing a difficulty in the production of smaller-scale nanostructures and devices, which is the major drawback [255]. To overcome this problem, better methods to realize conductance based on DNA scaffolds have to be developed. The laser-induced photochemistry is probably a promising solution.

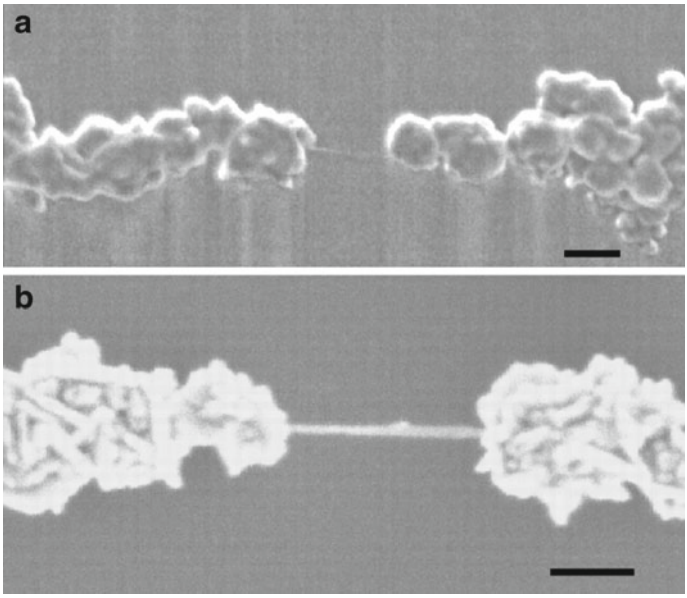

Fig. 1.41 A DNA-templated carbon nanotube FET and metallic wires contacting it. SEM images of SWNTs contacted by self-assembled DNA-templated gold wires. **a** An individual SWNT. **b** A rope of SWNTs. Scale bars, 100 nm [254]

1.7 Ultrafast Laser Near- and Super-Resolution Manufacturing

For decades, the ultrafast laser has been successfully used in cutting, drilling, welding, cleaning, surface modification, micromachining, and additive manufacturing [256]. Super-resolution processing is always one of the attractive goals of precision laser processing. Super-resolution laser manufacturing technology refers to technology that manufactures or processes dimensions smaller than the optical diffraction limit of the laser system ($\sim\lambda/(2n.\sin\alpha)$). At present, the smallest voxel size is about 50 nm, which is equivalent to 0.5 million dots per inch (dpi) in today's 2D graphics printing [257]. Although this value is already more than ten times smaller than the laser wavelength used, they are insufficient to manufacture many components compared to an electron beam with a resolution of a few nanometers, which is frequently required for a molecular device. Therefore, many innovative methods are still under development to further increase the resolution.

1.7.1 Two-Photon Direct Writing

The two-photon direct writing technology based on femtosecond laser has been developed to prepare micro/nanostructures. Two-photon absorption means that organic material molecules can simultaneously absorb two photons, with the same or different frequencies, and then be excited from a low energy state to a higher energy state. This two-photon direct writing technology enables the feature size of 3D printing down to submicron, thereby promoting the trend of miniaturization. The theoretical manufacturing size of TPP is about $\lambda/(2.7n.\sin\alpha)$, smaller than the single-photon diffraction limit [18]. Gissibl demonstrated the application of direct writing and testing by two-photon direct laser writing with a target of approximately 100 μm multilens and verified its high performance and functionality for quantitative measurement of modulation transfer function and aberrations [258]. Liao proposed a technique based on two-photon polymerization (TPP) for the preparation of precise and customizable hollow three-dimensional microstructure devices [259]. Different from traditional manufacturing technology, direct laser writing with TPP manufacturing scheme can better control all geometric characteristics of the manufactured architecture both interiorly and exteriorly. Two-photon printing is also used in the biological field. Worthington used the two-photon direct writing technique to print topological patterns with different feature sizes to study their effects on cell differentiation. This technique demonstrates a fast manufacturing of terrain surfaces with well-defined shapes with a resolution of less than 3 μm [260].

1.7.2 Near-Field Manufacturing

Another powerful nanofabrication using lasers with a spatial resolution beyond the optical diffraction limit is to use near-field technology, that is, evanescent waves manufacturing near scattering objects, which can achieve sub-diffraction limited focusing (minimum ~10 nm) [261]. In the near-field optical phenomenon, the evanescent wave becomes more important than free space far-field wave. The characteristic of the evanescent wave is that its amplitude decays rapidly in at least one direction of space. The light can be confined to a lateral dimension far less than half of the wavelength. There are a few near-field laser nanomanufacturing technologies as follows.

Particle lens array (PLA) technology uses an array of two-dimensional (2D) small particles as a lens array. The array is then used to convert the laser beam into a near-field parallel focused multiple enhancement optical spot. The efficiency of this method is very high. As the lens array covers a large area, millions of nanostructures can be prepared by irradiating with laser pulse only once. This makes it an ideal method for nanofabrication of large-area surfaces [262]. With 140 nm dielectric particles and 248 nm laser light source, PLA can obtain smaller features with a resolution as low as 30 nm [263].

Laser coupled near-field scanning optical microscopy tip can prepare arbitrary-shaped nanofeatures by controlling the path of the needle tip, as shown in Fig. 1.42. In a scanning near-field optical microscope (SNOM), a very small fiber tip (usually 50 nm) is used to scan while approaching the target surface (10–20 nm), which produces a high-resolution evanescent energy field at the tip [19]. Using this method a resolution of 35 nm can be obtained, corresponding to $\lambda/10$ [264].

Plasma lithography (PL) technology is the use of surface plasmon ultrashort wavelength characteristics combined with field positioning for nanolithography. Surface plasmons can produce high-precision patterns to realize a subwavelength resolution in the optical near-field with metal masks [265]. The lithography mask is usually composed of a silver film perforated with a 2D nanohole array. Numerical studies have shown that this method can achieve a lithographic resolution of 20 nm by using light at a wavelength of 365 nm through a silver mask. The experiment proves that the half-pitch resolution of nanolithography is as low as 60 nm [266, 267]. Dong proposed a surface plasmon interference lithography technique that uses a deep ultraviolet plasma structure to form ultra-high-resolution periodic nanopatterns in photoresists. The resolution of the generated pattern can thus be adjusted by changing the refractive index and thickness of the photoresist [268]. It is proved by numerical methods that one-dimensional and two-dimensional patterns with a half-pitch resolution of 14.6 nm can be generated. In addition, the half-pitch resolution of the generated pattern can be as low as 13 nm, using a high refractive index photoresist.

1.7.3 Stimulated Emission Depletion (STED) Manufacturing

In 1994, Hell and Wichmann provided a revolutionary proposal to ultimately break Abbe's resolution limit in fluorescence microscopy [269]. In their proposal, the fluorophore at the outer edge of the point spread function (PSF) is deliberately switched off by a mechanism of stimulated emission depletion (STED). Here, a second laser beam is focused into a special ring-shape, deactivating a surrounding part of the excited molecules, thereby limiting the effect of the excitation laser to a small volume at the central spot. In this case, the observation region does not have any fundamental diffraction limits. STED-nanoscopy has been proven to achieve resolutions below 10 nm [270]. In 2014, Stefan Hell was awarded the Nobel Prize in Chemistry, because of the diffraction barrier is eliminated in the optical fluorescence microscope, through the concept of stimulated emission depletion (STED) [270]. This STED concept can also be applied to optical super-resolution manufacturing. Figure 1.43 shows typical setups of STED microscopy and STED lithography. In a typical STED principle, the diameter of the exposure area can be calculated by the formula [271, 272]

$$d \approx \frac{\lambda}{2n\sin\alpha\sqrt{1 + bI_{\mathrm{STED}}/I_{\mathrm{S}}}} \tag{1.6.1}$$

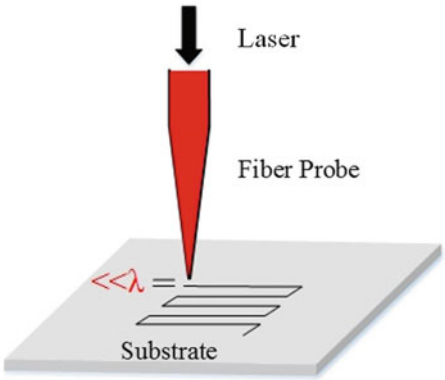

Fig. 1.42 A schematic diagram of laser coupled scanning near field optical microscopy tip [19]

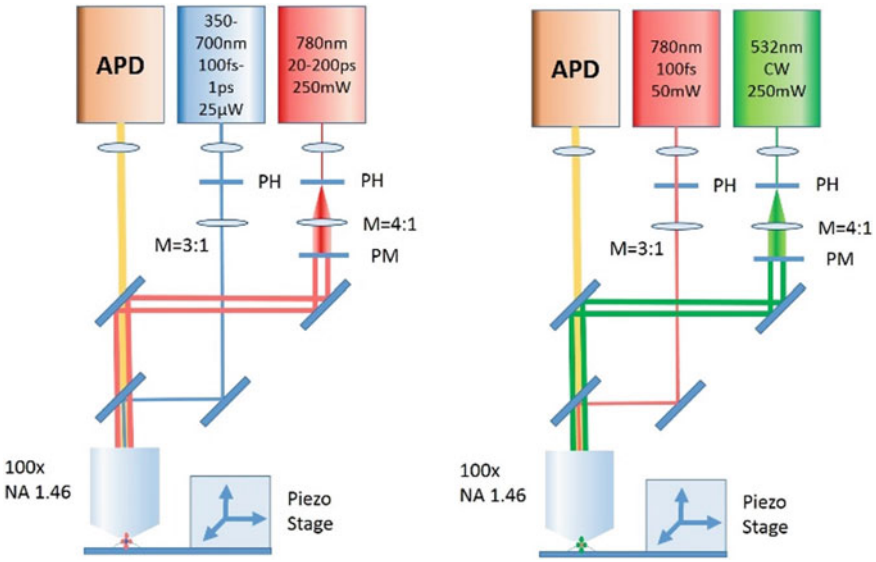

Fig. 1.43 Set up of STED microscopy (left) and STED lithography (right) [19]

where $n\sin\alpha$ is the numerical aperture, b is a systematic coefficient dependent on the beam shape, I_{STED} is the intensity of the depletion light, and I_{s} is the switching intensity at which half of the radicals will be depleted through stimulated emission. It can be easily understood that one can reduce the exposure area by increasing $I_{\mathrm{STED}}/I_{\mathrm{S}}$ ratios. Wollhofen proposed new limitations on the lateral resolution and feature size of the STED lithography technology with two-photon STED direct laser writing. The minimum lateral width can be prepared up to 55 nm, the width of separated twin lines can reach 120 nm [273]. Vitukhnovsky demonstrated the advantages of STED-inspired nanolithography for the preparation of metals and hybrid

nanostructures [274]. Compared with the direct laser writing method, they demonstrated that the use of STED nanolithography can greatly reduce the lateral size of the line. Using optically STED lithography, sub-diffraction-limited acrylate nanoanchors were prepared [275]. Acrylic nanopatches with a diameter of 60–70 nm prepared by STED enhanced two-photon polymerization are easily functionalized by antibodies at the single-molecule level. He proposed a control method of 45 nm wire based on direct laser writing with STED, which has a rod-shaped effective focal point. In traditional standard direct laser writing, a donut-shaped depletion focus is usually used, and the minimum line width is limited to 55 nm. In this work, they push this limit to the sub-50 nm size with a rod-like effective focal point, which is a combination of Gaussian excitation focusing and twin-oval depletion focusing [276]. Furthermore, Gan has demonstrated deep sub-diffraction optical beam lithography with a 9 nm feature size based on the STED mechanism [277].

1.8 Summary and Outlooks

A laser is a crucial tool for precise micro-to-nano manufacturing. For various applications the understanding of fundamentals between the laser and material interaction is basic. With the development of ultrafast laser available for a shorter pulse, higher peak power, and tunable wavelength at a wider band, the laser manufacturing enables versatile processing with a higher precision beyond the optical diffraction limit.

The basic interaction of laser and materials involves in energy absorption. At a micro-to-nanoscale, this physical procedure includes surface plasmon excitation and surface electron excitation. At a periodic approximately equal to or shorter than the electron-lattice coupling time, typically a couple of picoseconds, the so-called Coulomb explosion, and nonthermal melting will occur due to the surface electron vaporization. This localizes the thermal effect to the size similar to the optical penetration depth. This is the current physical basis for precision manufacturing using an ultrafast laser.

At a nanoscale, the physical properties of materials will be quite different from their bulk counterparts. The micro-to-nano manufacturing leads to the mass transfer at these scopes. The surface properties will be dominant due to the size effect and the scaling laws. The nanoparticles can be melt and sintered at a pretty low temperature, even close to room temperature. The involved surface liquid phase and enhanced surface diffusion will bring new mechanisms to the manufacturing and materials science.

Due to these new features, laser-based micro-to-nanomanufacturing is especially effective and powerful for printed electronics, such as flexible/stretchable electronics, 3D microprinting for portable electronics at current big data, Internet of things, next-generation computation and artificial intelligent era. It will create extensive opportunities in energy, environment, sensing, and biomedical applications.

With the further development of laser-based micro-to-nano manufacturing, it can be expected that molecular devices with high manufacturing and manipulation will

be research hot topics. These fields should base on hybrid manufacturing which may involve interdisciplinary techniques and disruptive concepts, such as near-field manufacturing and super-resolution manufacturing. It is believed that these progress may pave the way for science and technique evolution for post-Si and post-Moore's law and beyond.

Acknowledgements This book chapter is partially based on the lectures of Dr. Anming Hu presented at the course of "introduction to micro-to-nanomanufacturing" at the University of Tennessee Knoxville (UTK) for the period of 2014 to 2019. Some materials are modified from the students' presentations and course exercises. The contribution from all students is therefore recognized. The authors are also grateful to Dr. Seungha Shin (UTK) for numerical simulation and computation simulation, Dr. Jayne Wu (UTK) for ACEK mechanism, and Dr. Feng-yuan Zhang (UTK) for the scaling theory. The cited research work was supported by numerical funds. These supports are also sincerely grateful by the authors.

References

1. S. Lei, X. Zhao, X. Yu, A. Hu, S. Vukelic, M.B.G. Jun, H.-E. Joe, Y.L. Yao, Y.C. Shin. Ultrafast laser applications in manufacturing processes: a state-of-the-art review. J. Manuf. Sci. Eng. **142** (2020)
2. Y. Yu, S. Bai, S. Wang, A. Hu, Ultra-short pulsed laser manufacturing and surface processing of microdevices. Engineering **4**, 779–786 (2018)
3. Y. Yu, S. Wang, D. Ma, P. Joshi, A. Hu, Recent progress on laser manufacturing of microsize energy devices on flexible substrates. JOM **70**, 1816–1822 (2018)
4. A. Hu, Interaction of nanosecond and femtosecond laser pulses with carbon: deposition of carbon films having novel compositions. Thesis, UWSpace (2008)
5. A. Hu, P. Peng, H. Alarifi, X. Zhang, J. Guo, Y. Zhou, W. Duley, Femtosecond laser welded nanostructures and plasmonic devices. J. Laser Appl. **24**, 042001 (2012)
6. Y. Yu, Y. Deng, M.A. Al Hasan, Y. Bai, R.-Z. Li, S. Deng, P. Joshi, S. Shin, A. Hu. Femtosecond laser-induced non-thermal welding for a single Cu nanowire glucose sensor. Nanoscale Adv. **2**, 1195–1205 (2020)
7. D. Strickland, G. Mourou, Compression of amplified chirped optical pulses. Optics Commun. **56**, 219–221 (1985)
8. M.F. Yanik, H. Cinar, H.N. Cinar, A.D. Chisholm, Y. Jin, A. Ben-Yakar, Functional regeneration after laser axotomy. Nature **432**, 822 (2004)
9. C. Momma, B.N. Chichkov, S. Nolte, F. von Alvensleben, A. Tünnermann, H. Welling, B. Wellegehausen, Short-pulse laser ablation of solid targets. Opt. Commun. **129**, 134–142 (1996)
10. R. Srinivasan, E. Sutcliffe, B. Braren, Ablation and etching of polymethylmethacrylate by very short (160 fs) ultraviolet (308 nm) laser pulses. Appl. Phys. Lett. **51**, 1285–1287 (1987)
11. S. Küper, M. Stuke, Femtosecond UV excimer laser ablation. Appl. Phys. B **44**, 199–204 (1987)
12. N. Bärsch, K. Körber, A. Ostendorf, K.H. Tönshoff, Ablation and cutting of planar silicon devices using femtosecond laser pulses. Appl. Phys. A **77**, 237–242 (2003)
13. S.S. Wellershoff, J. Hohlfeld, J. Güdde, E. Matthias, The role of electron–phonon coupling in femtosecond laser damage of metals. Appl. Phys. A **69**, S99–S107 (1999)
14. R.R. Gattass, E. Mazur, Femtosecond laser micromachining in transparent materials. Nat. Photon. **2**, 219–225 (2008)
15. K. Sugioka, Y. Cheng, Ultrafast lasers—reliable tools for advanced materials processing. Light: Sci. Appl. **3**, e149–e149 (2014)

16. A. Hu, M. Rybachuk, Q.B. Lu, W.W. Duley, Direct synthesis of sp-bonded carbon chains on graphite surface by femtosecond laser irradiation. Appl. Phys. Lett. **91**, 131906 (2007)
17. C. Zheng, A. Hu, T. Chen, K.D. Oakes, S. Liu, Femtosecond laser internal manufacturing of three-dimensional microstructure devices. Appl. Phys. A **121**, 163–177 (2015)
18. J. Fischer, M. Wegener, Three-dimensional optical laser lithography beyond the diffraction limit. Laser Photon. Rev. **7**, 22–44 (2013)
19. W. Zhou, D. Bridges, R. Li, S. Bai, Y. Ma, T. Hou, A. Hu, Recent progress of laser micro-and nano manufacturing. Sci. Lett. J **5**, 228 (2016)
20. S. Küper, M. Stuke, Ablation of UV-transparent materials with femtosecond UV excimer laser pulses. MRS Proc. **129**, 375 (1988)
21. C. Zheng, A. Hu, K.D. Kihm, Q. Ma, R. Li, T. Chen, W.W. Duley, Femtosecond laser fabrication of cavity microball lens (CMBL) inside a PMMA substrate for super-wide angle imaging. Small **11**, 3007–3016 (2015)
22. K. Seibert, G.C. Cho, W. Kütt, H. Kurz, D.H. Reitze, J.I. Dadap, H. Ahn, M.C. Downer, A.M. Malvezzi, Femtosecond carrier dynamics in graphite. Phys. Rev. B **42**, 2842–2851 (1990)
23. D.E. Aspnes, E.D. Palik, *Handbook of optical constants of solids* (Academic, New York, 1985), pp. 89–112
24. S.A. Maier, *Plasmonics: Fundamentals and Applications* (Springer, 2007)
25. A. Vial, A.-S. Grimault, D. Macías, D. Barchiesi, M.L. de la Chapelle, Improved analytical fit of gold dispersion: Application to the modeling of extinction spectra with a finite-difference time-domain method. Phys. Rev. B **71**, 085416 (2005)
26. C.B. Schaffer, A. Brodeur, E. Mazur, Laser-induced breakdown and damage in bulk transparent materials induced by tightly focused femtosecond laser pulses. Measure. Sci. Technol. **12**, 1784–1794 (2001)
27. L. Sheng-hsien, F. Yuichi, (*Advances in Multi-photon Processes and Spectroscopy* (World Scientific, 2004)
28. Y.L. Yao, H. Chen, W. Zhang, Time scale effects in laser material removal: a review. Int. J. Adv. Manuf. Technol. **26**, 598–608 (2005)
29. L.V. Keldysh, Ionization in the field of a strong electromagnetic wave. Sov. Phys. JETP **20**, 1307–1314 (1965)
30. P. Lambropoulos, *Multiphoton Ionization of Atoms* (Academic Press, 1984)
31. B.C. Stuart, M.D. Feit, S. Herman, A.M. Rubenchik, B.W. Shore, M.D. Perry, Nanosecond-to-femtosecond laser-induced breakdown in dielectrics. Phys. Rev. B **53**, 1749–1761 (1996)
32. K. Sokolowski-Tinten, D. von der Linde, Generation of dense electron-hole plasmas in silicon. Phys. Review B **61**, 2643–2650 (2000)
33. P. Stampfli, K.H. Bennemann, Theory for the instability of the diamond structure of Si, Ge, and C induced by a dense electron-hole plasma. Phys. Rev. B **42**, 7163–7173 (1990)
34. P. Stampfli, K.H. Bennemann, Dynamical theory of the laser-induced lattice instability of silicon. Phys. Rev. B **46**, 10686–10692 (1992)
35. P.L. Silvestrelli, A. Alavi, M. Parrinello, D. Frenkel, Ab initio molecular dynamics simulation of laser melting of silicon. Phys. Rev. Lett. **77**, 3149–3152 (1996)
36. P.L. Silvestrelli, A. Alavi, M. Parrinello, D. Frenkel, Structural, dynamical, electronic, and bonding properties of laser-heated silicon: An ab initio molecular-dynamics study. Phys. Rev. B **56**, 3806–3812 (1997)
37. D.H. Reitze, H. Ahn, M.C. Downer, Optical properties of liquid carbon measured by femtosecond spectroscopy. Phys. Rev. B **45**, 2677–2693 (1992)
38. M. Wautelet, Scaling laws in the macro-, micro- and nanoworlds. Eur. J. Phys. **22**, 601–611 (2001)
39. C. Yang, C.P. Wong, M.M.F. Yuen, Printed electrically conductive composites: conductive filler designs and surface engineering. J. Mat. Chem. C **1**, 4052–4069 (2013)
40. K. Lu, Sintering of nanoceramics. Int. Mat. Rev. **53**, 21–38 (2008)
41. Y. Ma, H. Li, D. Bridges, P. Peng, B. Lawrie, Z. Feng, A. Hu, Zero-dimensional to three-dimensional nanojoining: current status and potential applications. RSC Adv. **6**, 75916–75936 (2016)

42. F.G. Shi, Size dependent thermal vibrations and melting in nanocrystals. J. Mater. Res. **9**, 1307–1314 (1994)
43. Q. Jiang, S.H. Zhang, J.C. Li, Grain size-dependent diffusion activation energy in nanomaterials. Solid State Commun. **130**, 581–584 (2004)
44. P. Peng, A. Hu, A.P. Gerlich, G. Zou, L. Liu, Y.N. Zhou, Joining of silver nanomaterials at low temperatures: processes, properties, and applications. ACS Appl. Mater. Interfaces. **7**, 12597–12618 (2015)
45. A. Hu, J.Y. Guo, H. Alarifi, G. Patane, Y. Zhou, G. Compagnini, C.X. Xu, Low temperature sintering of Ag nanoparticles for flexible electronics packaging. Appl. Phys. Lett. **97**, 153117 (2010)
46. D. Bridges, C. Rouleau, Z. Gosser, C. Smith, Z. Zhang, K. Hong, J. Cheng, Y. Bar-Cohen, A. Hu, Self-powered fast brazing of Ti–6Al–4 V using Ni/Al reactive multilayer films. Appl. Sci. **8**, 985 (2018)
47. Y. Lu, J.Y. Huang, C. Wang, S. Sun, J. Lou, Cold welding of ultrathin gold nanowires. Nat. Nanotechnol. **5**, 218–224 (2010)
48. P. Peng, L. Liu, A.P. Gerlich, A. Hu, Y.N. Zhou, Self-oriented nanojoining of silver nanowires via surface selective activation. Particle Particle Syst. Character. **30**, 420–426 (2013)
49. K. Dick, T. Dhanasekaran, Z. Zhang, D. Meisel, Size-dependent melting of silica-encapsulated gold nanoparticles. J. Am. Chem. Soc. **124**, 2312–2317 (2002)
50. A. Ghosh, B. Corves. *Introduction to Micromechanisms and Microactuators* (Springer, 2015)
51. K.E. Drexier, in *Nanosystems* (Wiley, 1992, Chap. 2)
52. K. Liu, S. Sun, A. Majumdar, V.J. Sorger, Fundamental scaling laws in nanophotonics. Sci. Rep. **6**, 37419 (2016)
53. X.-Y. Zhang, A. Hu, T. Zhang, X.-J. Xue, J.Z. Wen, W.W. Duley, Subwavelength plasmonic waveguides based on ZnO nanowires and nanotubes: a theoretical study of thermo-optical properties. Appl. Phys. Lett. **96**, 043109 (2010)
54. X. Zhang, T. Zhang, A. Hu, Y. Song, W.W. Duley, Controllable plasmonic antennas with ultra narrow bandwidth based on silver nano-flags. Appl. Phys. Lett. **101**, 153118 (2012)
55. X.-Y. Zhang, A. Hu, J.Z. Wen, T. Zhang, X.-J. Xue, Y. Zhou, W.W. Duley, Numerical analysis of deep sub-wavelength integrated plasmonic devices based on semiconductor-insulator-metal strip waveguides. Opt. Express **18**, 18945–18959 (2010)
56. H. Raether, in *Surface Plasmons on Smooth and Rough Surfaces and on Gratings* (Springer 1988), pp. 4–39
57. Z. Fang, X. Zhu, Plasmonics in Nanostructures. Adv. Mater. **25**, 3840–3856 (2013)
58. Y. Fang, N.-H. Seong, D.D. Dlott, Measurement of the distribution of site enhancements in surface-enhanced raman scattering. Science **321**, 388 (2008)
59. P. Peng, H. Huang, A. Hu, A.P. Gerlich, Y.N. Zhou, Functionalization of silver nanowire surfaces with copper oxide for surface-enhanced Raman spectroscopic bio-sensing. J. Mater. Chem. **22**, 15495–15499 (2012)
60. W. Hou, S.B. Cronin, A review of surface plasmon resonance-enhanced photocatalysis. Adv. Funct. Mater. **23**, 1612–1619 (2013)
61. G. Baffou, R. Quidant, C. Girard, Heat generation in plasmonic nanostructures: influence of morphology. Appl. Phys. Lett. **94**, 153109 (2009)
62. C. Ma, J. Yan, Y. Huang, C. Wang, G. Yang, The optical duality of tellurium nanoparticles for broadband solar energy harvesting and efficient photothermal conversion. Sci. Adv. **4**, eaas9894 (2018)
63. C. Clavero, Plasmon-induced hot-electron generation at nanoparticle/metal-oxide interfaces for photovoltaic and photocatalytic devices. Nat. Photon. **8**, 95–103 (2014)
64. T. Neumann, M.L. Johansson, D. Kambhampati, W. Knoll, Surface-plasmon fluorescence spectroscopy. Adv. Funct. Mat. **12**, 575–586 (2002)
65. G.I. Stegeman, J.J. Burke, D.G. Hall, Nonlinear optics of long range surface plasmons. Appl. Phys. Lett. **41**, 906–908 (1982)
66. P. Drude, Zur Elektronentheorie der Metalle. Ann. Phys. **306**, 566–613 (1900)

67. S. Link, M.A. El-Sayed, Shape and size dependence of radiative, non-radiative and photothermal properties of gold nanocrystals. Inte. Rev. Phys. Chem. **19**, 409–453 (2000)
68. E. Petryayeva, U.J. Krull, Localized surface plasmon resonance: nanostructures, bioassays and biosensing—A review. Anal. Chim. Acta **706**, 8–24 (2011)
69. W.L. Barnes, A. Dereux, T.W. Ebbesen, Surface plasmon subwavelength optics. Nature **424**, 824–830 (2003)
70. K. Welford, Surface plasmon-polaritons and their uses. Opt. Quant. Electron. **23**, 1–27 (1991)
71. Y. Hong, Y.-M. Huh, D.S. Yoon, J. Yang, Nanobiosensors based on localized surface plasmon resonance for biomarker detection. J. Nanomater. (2012)
72. A. Agrawal, S.H. Cho, O. Zandi, S. Ghosh, R.W. Johns, D.J. Milliron, Localized surface plasmon resonance in semiconductor nanocrystals. Chem. Rev. **118**, 3121–3207 (2018)
73. G. Mie, Beiträge zur Optik trüber Medien, speziell kolloidaler Metallösungen. Ann. Phys. **330**, 377–445 (1908)
74. H. Yu, Y. Peng, Y. Yang, Z.-Y. Li, Plasmon-enhanced light–matter interactions and applications. NPJ Comput. Mater. **5**, 45 (2019)
75. X.-Y. Zhang, A. Hu, T. Zhang, W. Lei, X.-J. Xue, Y. Zhou, W.W. Duley, Self-assembly of large-scale and ultrathin silver nanoplate films with tunable plasmon resonance properties. ACS Nano **5**, 9082–9092 (2011)
76. W. Zhou, A. Hu, S. Bai, Y. Ma, D. Bridges, Anisotropic optical properties of large-scale aligned silver nanowire films via controlled coffee ring effects. RSC Adv. **5**, 39103–39109 (2015)
77. D.K. Gramotnev, S.I. Bozhevolnyi, Plasmonics beyond the diffraction limit. Nat. Photon. **4**, 83–91 (2010)
78. M. Born, E. Wolf, *Principle of Optics*, 7th edn (World Scientific, Cambridge, 1999)
79. L. Tong, F. Zi, X. Guo, J. Lou, Optical microfibers and nanofibers: a tutorial. Opt. Commun. **285**, 4641–4647 (2012)
80. L. Tong, J. Lou, E. Mazur, Single-mode guiding properties of subwavelength-diameter silica and silicon wire waveguides. Opt. Express **12**, 1025–1035 (2004)
81. X. Guo, Y. Ma, Y. Wang, L. Tong, Nanowire plasmonic waveguides, circuits and devices. Laser Photon. Rev. **7**, 855–881 (2013)
82. Y. Fang, Z. Li, Y. Huang, S. Zhang, P. Nordlander, N.J. Halas, H. Xu, Branched silver nanowires as controllable plasmon routers. Nano Lett. **10**(5), 1950–1954 (2010)
83. J. Takahara, S. Yamagishi, H. Taki, A. Morimoto, T. Kobayashi, Guiding of a one-dimensional optical beam with nanometer diameter. Opt. Lett. **22**, 475–477 (1997)
84. H. Ditlbacher, A. Hohenau, D. Wagner, U. Kreibig, M. Rogers, F. Hofer, F.R. Aussenegg, J.R. Krenn, Silver nanowires as surface plasmon resonators. Phys. Rev. Lett. **95**, 257403 (2005)
85. A.W. Sanders, D.A. Routenberg, B.J. Wiley, Y. Xia, E.R. Dufresne, M.A. Reed, Observation of plasmon propagation, redirection, and fan-out in silver nanowires. Nano Lett. **6**, 1822–1826 (2006)
86. R.F. Oulton, V.J. Sorger, D.A. Genov, D.F.P. Pile, X. Zhang, A hybrid plasmonic waveguide for subwavelength confinement and long-range propagation. Nat. Photon. **2**, 496–500 (2008)
87. R.F. Oulton, V.J. Sorger, T. Zentgraf, R.-M. Ma, C. Gladden, L. Dai, G. Bartal, X. Zhang, Plasmon lasers at deep subwavelength scale. Nature **461**, 629–632 (2009)
88. L. Lin, L. Liu, P. Peng, G. Zou, W.W. Duley, Y.N. Zhou, In situ nanojoining of Y-and T-shaped silver nanowires structures using femtosecond laser radiation. Nanotechnology **27**, 125201 (2016)
89. Y. Fang, Z. Li, Y. Huang, S. Zhang, P. Nordlander, N.J. Halas, H. Xu, Branched silver nanowires as controllable plasmon routers. Nano Lett. **10**, 1950–1954 (2010)
90. R. Yan, P. Pausauskie, J. Huang, P. Yang, Direct photonic–plasmonic coupling and routing in single nanowires. Proc. Natl. Acad. Sci. **106**, 21045 (2009)
91. A.D. Semenov, G.N. Goltsman, R. Sobolewski. Hot-electron effect in superconductors and its applications for radiation sensors. Supercond. Sci. Technol. **15**, R1–R16 (2002)
92. S. Link, M.A. El-Sayed, Spectral properties and relaxation dynamics of surface plasmon electronic oscillations in gold and silver nanodots and nanorods. J. Phys. Chem. B **103**, 8410–8426 (1999)

93. A.O. Govorov, W. Zhang, T. Skeini, H. Richardson, J. Lee, N.A. Kotov, Gold nanoparticle ensembles as heaters and actuators: melting and collective plasmon resonances. Nanoscale Res. Lett. **1**, 84 (2006)
94. E.C. Garnett, W. Cai, J.J. Cha, F. Mahmood, S.T. Connor, M. Greyson Christoforo, Y. Cui, M.D. McGehee, M.L. Brongersma. Self-limited plasmonic welding of silver nanowire junctions. Nat. Mat. **11**, 241–249 (2012)
95. R.-Z. Li, A. Hu, D. Bridges, T. Zhang, K.D. Oakes, R. Peng, U. Tumuluri, Z. Wu, Z. Feng, Robust Ag nanoplate ink for flexible electronics packaging. Nanoscale **7**, 7368–7377 (2015)
96. J. Qiu, W.D. Wei, Surface plasmon-mediated photothermal chemistry. J. Phys. Chem. C **118**, 20735–20749 (2014)
97. A. Csaki, F. Garwe, A. Steinbrück, G. Maubach, G. Festag, A. Weise, I. Riemann, K. König, W. Fritzsche, A parallel approach for subwavelength molecular surgery using gene-specific positioned metal nanoparticles as laser light antennas. Nano Lett. **7**, 247–253 (2007)
98. R.Z. Li, R. Peng, K.D. Kihm, S. Bai, D. Bridges, U. Tumuluri, Z. Wu, T. Zhang, G. Compagnini, Z. Feng, A. Hu, High-rate in-plane micro-supercapacitors scribed onto photo paper using in situ femtolaser-reduced graphene oxide/Au nanoparticle microelectrodes. Energy Environ. Sci. **9**, 1458–1467 (2016)
99. L. Röntzsch, K.-H. Heinig, J.A. Schuller, M.L. Brongersma, Thin film patterning by surface-plasmon-induced thermocapillarity. Appl. Phys. Lett. **90**, 044105 (2007)
100. J.M. Stern, J. Stanfield, W. Kabbani, J.-T. Hsieh, J.A. Cadeddu, Selective Prostate cancer thermal ablation with laser activated gold nanoshells. J. Urol. **179**, 748–753 (2008)
101. R.-Z. Li, A. Hu, T. Zhang, K.D. Oakes, Direct writing on paper of foldable capacitive touch pads with silver nanowire inks. ACS Appl. Mater. Interfaces. **6**, 21721–21729 (2014)
102. Y. Huang, Y. Tian, C. Hang, Y. Liu, S. Wang, M. Qi, H. Zhang, J. Zhao, Self-limited nanosoldering of silver nanowires for high-performance flexible transparent heaters. ACS Appl. Mater. Interfaces. **11**, 21850–21858 (2019)
103. R.M. German, P. Suri, S.J. Park, Review: liquid phase sintering. J. Mater. Sci. **44**, 1–39 (2009)
104. F.E. Kruis, K.A. Kusters, S.E. Pratsinis, B. Scarlett, A simple model for the evolution of the characteristics of aggregate particles undergoing coagulation and sintering. Aerosol Sci. Technol. **19**, 514–526 (1993)
105. W.K. Lee, R.L. Eadie, G.C. Weatherly, K.T. Aust, A study of the sintering of spherical silver powder—II. The initial stage. Acta Metall. **26**, 1837–1843 (1978)
106. M.I. Alymov, E.I. Maltina, Y.N. Stepanov, Model of initial stage of ultrafine metal powder sintering. Nanostruct. Mater. **4**, 737–742 (1994)
107. H.A. Alarifi, M. Atis, Z. Ouml, C. Gbreve, A. Hu, M. Yavuz, Y. Zhou. Molecular dynamics simulation of sintering and surface premelting of silver nanoparticles. Mater. Tran. **54**, 884–889 (2013)
108. H.A. Alarifi, M. Atiş, C. Özdoğan, A. Hu, M. Yavuz, Y. Zhou, Determination of complete melting and surface premelting points of silver nanoparticles by molecular dynamics simulation. J. Phys. Chem. C **117**, 12289–12298 (2013)
109. W. Zhou, S. Bai, Y. Ma, D. Ma, T. Hou, X. Shi, A. Hu, Laser-direct writing of silver metal electrodes on transparent flexible substrates with high-bonding strength. ACS Appl. Mater. Interf. **8**, 24887–24892 (2016)
110. H.-J. Hwang, K.-H. Oh, H.-S. Kim, All-photonic drying and sintering process via flash white light combined with deep-UV and near-infrared irradiation for highly conductive copper nano-ink. Sci. Rep. **6**, 19696 (2016)
111. J.R. Greer, R.A. Street, Thermal cure effects on electrical performance of nanoparticle silver inks. Acta Mater. **55**, 6345–6349 (2007)
112. S. Mypati, S.R. Dhanushkodi, M. McLaren, A. Docoslis, B.A. Peppley, D.P.J. Barz, Optimized inkjet-printed silver nanoparticle films: theoretical and experimental investigations. RSC Adv. **8**, 19679–19689 (2018)
113. M. Kaganov, E. Lifshitz, L. Tanatarov, Relaxation between electrons and the crystalline lattice. Soviet Phys.-JETP **4**, 173–178 (1957)

114. S. Anisimov, B. Kapeliovich, T. Perelman, Electron emission from metal surfaces exposed to ultrashort laser pulses. Zh. Eksp. Teor. Fiz. **66**, 375–377 (1974)
115. B.N. Chichkov, C. Momma, S. Nolte, F. von Alvensleben, A. Tunnermann, Appl. Phys. A **63**, 109 (1996)
116. M.D. Shirk, P.A. Molian, Ultra-short pulsed laser ablation of highly oriented pyrolytic graphite. Carbon **39**, 1183–1193 (2001)
117. W.W. Duley (*UV Lasers: Effects and Applications in Materials Science* (Cambridge University Press, 2005)
118. M.D. Perry, B.C. Stuart, P.S. Banks, M.D. Feit, V. Yanovsky, A.M. Rubenchik, Ultrashort-pulse laser machining of dielectric materials. J. Appl. Phys. **85**, 6803–6810 (1999)
119. T.L. Bergman, F.P. Incropera, D.P. DeWitt, A.S. Lavine, *Fundamentals of Heat and Mass Transfer* (Wiley, 2011)
120. J.H. Lienhard, *A Heat Transfer Textbook* (Courier Dover Publications, 2019)
121. D. Bergström, The absorption of laser light by rough metal surfaces (2008)
122. Z. Yang, J. Hao, S. Yuan, S. Lin, H.M. Yau, J. Dai, S.P. Lau, Field-effect transistors based on amorphous black phosphorus ultrathin films by pulsed laser deposition. Adv. Mater. **27**, 3748–3754 (2015)
123. L.L. Taylor, R.E. Scott, J. Qiao, Integrating two-temperature and classical heat accumulation models to predict femtosecond laser processing of silicon. Opt. Mater. Express **8**, 648–658 (2018)
124. Z. Lin, L.V. Zhigilei, V. Celli, Electron-phonon coupling and electron heat capacity of metals under conditions of strong electron-phonon nonequilibrium. Phys. Rev. B **77**, 075133 (2008)
125. Y. Wang, Z. Lu, X. Ruan, First principles calculation of lattice thermal conductivity of metals considering phonon-phonon and phonon-electron scattering. J. Appl. Phys. **119**, 225109 (2016)
126. S.W. Holman, R.R. Lawrence, L. Barr (1895)
127. U. Nerle, M.K. Rabinal, Thermal oxidation of copper for favorable formation of cupric oxide (CuO) semiconductor. IOSR J. Appl. Phys. **5**, 1–7 (2013)
128. M. Kaur, K.P. Muthe, S.K. Despande, S. Choudhury, J.B. Singh, N. Verma, S.K. Gupta, J.V. Yakhmi, Growth and branching of CuO nanowires by thermal oxidation of copper. J. Cryst. Growth **289**, 670–675 (2006)
129. J.K. Chen, D.Y. Tzou, J.E. Beraun, Numerical investigation of ultrashort laser damage in semiconductors. Int. J. Heat Mass Transf. **48**, 501–509 (2005)
130. Y. Bentor, *Periodic Table: Copper*. http://www.chemicalelements.com/elements/cu.html
131. J.P. Abid, A.W. Wark, P.F. Brevet, H.H. Girault, Preparation of silver nanoparticles in solution from a silver salt by laser irradiation. Chem. Commun. 792–793 (2002). https://doi.org/10.1039/b200272h
132. S. Bai, Y.-H. Lin, X.-P. Zhang, W.-P. Zhou, T. Chen, Y. Ma, T.-X. Hou, D. Bridges, K.D. Oakes, A. Hu, Two-step photonic reduction of controlled periodic silver nanostructures for surface-enhanced Raman spectroscopy. Plasmonics **10**, 1675–1685 (2015)
133. S. Bai, S. Zhang, W. Zhou, D. Ma, Y. Ma, P. Joshi, A. Hu, Laser-assisted reduction of highly conductive circuits based on copper nitrate for flexible printed sensors. Nano-Micro Lett. **9**, 42 (2017)
134. E. Marzbanrad, A. Hu, B. Zhao, Y. Zhou, Room temperature nanojoining of triangular and hexagonal silver nanodisks. J. Phys. Chem. C **117**, 16665–16676 (2013)
135. J. Bai, Y. Qin, C. Jiang, L. Qi, Polymer-controlled synthesis of silver nanobelts and hierarchical nanocolumns. Chem. Mater. **19**, 3367–3369 (2007)
136. C.L. Thomsen, D. Madsen, J. Tho/gersen, J.R. Byberg, S.R. Keiding, Femtosecond spectroscopy of the dissociation and geminate recombination of aqueous CS2. J. Chem. Phys. **111**, 703–710
137. C.R. Wang, A. Hu, Q.B. Lu, Direct observation of the transition state of ultrafast electron transfer reaction of a radiosensitizing drug bromodeoxyuridine. J. Chem. Phys. **124**, 241102 (2006)

138. M. Maillard, P. Huang, L. Brus, Silver nanodisk growth by surface plasmon enhanced photoreduction of adsorbed [Ag +]. Nano Lett. **3**, 1611–1615 (2003)
139. S. Bai, W. Zhou, Y. Lin, Y. Zhao, T. Chen, A. Hu, W.W. Duley, Ultraviolet pulsed laser interference lithography and application of periodic structured Ag-nanoparticle films for surface-enhanced Raman spectroscopy. J. Nanopart. Res. **16**, 2470 (2014)
140. Y. Nakata, Y. Matsuba, K. Murakawa, N. Miyanaga, Change of interference pattern using fundamental and second-harmonic wavelengths by phase shift of a beam. Appl. Phys. A **117**, 207–210 (2014)
141. S. Bai, D. Serien, A. Hu, K. Sugioka, 3D microfluidic surface-enhanced Raman spectroscopy (SERS) chips fabricated by all-femtosecond-laser-processing for real-time sensing of toxic substances. Adv. Funct. Mater. **28**, 1706262 (2018)
142. S.M. Yalisove, K. Sugioka, C.P. Grigoropoulos, Advances and opportunities of ultrafast laser synthesis and processing. MRS Bull. **41**, 955–959 (2016)
143. A. Hu, J. Sanderson, A.A. Zaidi, C. Wang, T. Zhang, Y. Zhou, W.W. Duley, Direct synthesis of polyyne molecules in acetone by dissociation using femtosecond laser irradiation. Carbon **46**, 1823–1825 (2008)
144. L. Rapp, B. Haberl, C.J. Pickard, J.E. Bradby, E.G. Gamaly, J.S. Williams, A.V. Rode, Experimental evidence of new tetragonal polymorphs of silicon formed through ultrafast laser-induced confined microexplosion. Nat. Commun. **6**, 7555 (2015)
145. A.A. Zaidi, A. Hu, D.E. Henneke, W.W. Duley, Femtosecond laser irradiation of liquid alkanes: mechanism of polyyne formation. Chem. Phys. Lett. **723**, 151–154 (2019)
146. A.A. Zaidi, A. Hu, M.J. Wesolowski, X. Fu, J.H. Sanderson, Y. Zhou, W.W. Duley, Time of flight mass spectrometry of polyyne formation in the irradiation of liquid alkanes with femtosecond laser pulses. Carbon **48**, 2517–2520 (2010)
147. T. Matsuda, T. Sano, K. Arakawa, O. Sakata, H. Tajiri, A. Hirose, Femtosecond laser-driven shock-induced dislocation structures in iron. Appl. Phys. Express **7**, 122704 (2014)
148. T. Sano, T. Eimura, R. Kashiwabara, T. Matsuda, Y. Isshiki, A. Hirose, S. Tsutsumi, K. Arakawa, T. Hashimoto, K. Masaki, Femtosecond laser peening of 2024 aluminum alloy without a sacrificial overlay under atmospheric conditions. J. Laser Appl. **29**, 012005 (2017)
149. J.D. Majumdar, E.L. Gurevich, R. Kumari, A. Ostendorf, Investigation on femto-second laser irradiation assisted shock peening of medium carbon (0.4% C) steel. Appl. Surface Sci. **364**, 133–140 (2016)
150. P. Russo, A. Hu, G. Compagnini, W.W. Duley, N.Y. Zhou, Femtosecond laser ablation of highly oriented pyrolytic graphite: a green route for large-scale production of porous graphene and graphene quantum dots. Nanoscale **6**, 2381–2389 (2014)
151. P. Russo, A. Hu, G. Compagnini, Synthesis, properties and potential applications of porous graphene: a review. Nano-Micro Lett. **5**, 260–273 (2013)
152. Q. Su, S. Bai, J. Han, Y. Ma, Y. Yu, Y. Deng, M. Wu, C. Zheng, A. Hu, Precise laser trimming of alloy strip resistor: a comparative study with femtosecond laser and nanosecond laser. J. Laser Appl. **32**, 022013 (2020)
153. C. Zheng, A. Hu, R. Li, D. Bridges, T. Chen, Fabrication of embedded microball lens in PMMA with high repetition rate femtosecond fiber laser. Opt. Express **23**, 17584–17598 (2015)
154. D.C. Cox, R.D. Forrest, P.R. Smith, V. Stolojan, S.R.P. Silva, Study of the current stressing in nanomanipulated three-dimensional carbon nanotube structures. Appl. Phys. Lett. **87**, 033102 (2005)
155. K. Keshoju, H. Xing, L. Sun, Magnetic field driven nanowire rotation in suspension. Appl. Phys. Lett. **91**, 123114 (2007)
156. E.R. Dufresne, D.G. Grier, Optical tweezer arrays and optical substrates created with diffractive optics. Rev. Sci. Instrum. **69**, 1974–1977 (1998)
157. B.J. Roxworthy, K.C. Toussaint, Femtosecond-pulsed plasmonic nanotweezers. Sci. Rep. **2**, 660 (2012)
158. C. Cheng, S. Wang, J. Wu, Y. Yu, R. Li, S. Eda, J. Chen, G. Feng, B. Lawrie, A. Hu, Bisphenol a sensors on polyimide fabricated by laser direct writing for onsite river water monitoring at attomolar concentration. ACS Appl. Mater. Interfaces. **8**, 17784–17792 (2016)

159. W. Jie, Biased AC electro-osmosis for on-chip bioparticle processing. IEEE Trans. Nanotechnol. **5**, 84–89 (2006)
160. J. Wu, Y. Ben, D. Battigelli, H.-C. Chang, Long-range AC electroosmotic trapping and detection of bioparticles. Ind. Eng. Chem. Res. **44**, 2815–2822 (2005)
161. M. Lian, N. Islam, J. Wu, AC electrothermal manipulation of conductive fluids and particles for lab-chip applications. IET Nanobiotechnol. **1**, 36–43 (2007)
162. A. GonzÁLez, A. Ramos, H. Morgan, N.G. Green, A. Castellanos, Electrothermal flows generated by alternating and rotating electric fields in microsystems. J. Fluid Mech. **564**, 415–433 (2006)
163. M. Stubbe, J. Gimsa, A short review on AC electro-thermal micropumps based on smeared structural polarizations in the presence of a temperature gradient. Colloids Surfaces A: Physicochem. Eng. Aspects **376**, 97–101 (2011)
164. G. Baysinger, L.I. Berger, R.N. Goldberg, H.V. Kehiaian, K. Kuchitsu, *CRC Handbook of Chemistry and Physics* (National Institute of Standards and Technology, 2015)
165. J. Wu, Interactions of electrical fields with fluids: laboratory-on-a-chip applications. IET Nanobiotechnol. **2**, 14–27 (2008)
166. A. Salari, M. Navi, T. Lijnse, C. Dalton, AC electrothermal effect in microfluidics: a review. Micromachines **10**, 762 (2019)
167. A. Jamshidi, Optoelectronic manipulation, assembly, and patterning of nanoparticles (2009)
168. X. Xing, J. Zheng, C. Sun, F. Li, D. Zhu, L. Lei, X. Cai, T. Wu, Graphene oxide-deposited microfiber: a new photothermal device for various microbubble generation. Opt. Express **21**, 31862–31871 (2013)
169. L. Dai, Jiao, L. Liu, in *Presented at 2016 IEEE 16th International Conference on Nanotechnology (IEEE-NANO), 22–25 Aug. 2016* (2016)
170. L. Dai, Z. Ge, N. Jiao, L. Liu, 2D to 3D manipulation and assembly of microstructures using optothermally generated surface bubble microrobots. Small **15**, 1902815 (2019)
171. E.C.H. Ng, K.M. Chin, C.C. Wong, Controlling inplane orientation of a monolayer colloidal crystal by meniscus pinning. Langmuir **27**, 2244–2249 (2011)
172. W. Lu, C.M. Lieber, in *Nanoscience and Technology: A Collection of Reviews from Nature Journals* (World Scientific 2010), pp. 137–146
173. H. Yan, H.S. Choe, S. Nam, Y. Hu, S. Das, J.F. Klemic, J.C. Ellenbogen, C.M. Lieber, Programmable nanowire circuits for nanoprocessors. Nature **470**, 240–244 (2011)
174. J. Kim, H.-C. Lee, K.-H. Kim, M.-S. Hwang, J.-S. Park, J.M. Lee, J.-P. So, J.-H. Choi, S.-H. Kwon, C.J. Barrelet, H.-G. Park, Photon-triggered nanowire transistors. Nat. Nanotechnol. **12**, 963–968 (2017)
175. C. Rewitz, G. Razinskas, P. Geisler, E. Krauss, S. Goetz, M. Pawłowska, B. Hecht, T. Brixner, Coherent control of plasmon propagation in a nanocircuit. Phys. Rev. Appl. **1**, 014007 (2014)
176. T. Gong, Y. Zhang, W. Liu, J. Wei, C. Li, K. Wang, D. Wu, M. Zhong, Connection of macro-sized double-walled carbon nanotube strands by bandaging with double-walled carbon nanotube films. Carbon **45**, 2235–2240 (2007)
177. K.P. Yung, J. Wei, B.K. Tay, Formation and assembly of carbon nanotube bumps for interconnection applications. Diamond Related Mater. **18**, 1109–1113 (2009)
178. T. Tokuno, M. Nogi, M. Karakawa, J. Jiu, T.T. Nge, Y. Aso, K. Suganuma, Fabrication of silver nanowire transparent electrodes at room temperature. Nano Res. **4**, 1215–1222 (2011)
179. P. Peng, W. Guo, Y. Zhu, L. Liu, G. Zou, Y.N. Zhou, Nanoscale wire bonding of individual ag nanowires on au substrate at room temperature. Nano-Micro Lett. **9**, 26 (2017)
180. Z. Gu, Y. Chen, D.H. Gracias, Surface tension driven self-assembly of bundles and networks of 200 nm diameter rods using a polymerizable adhesive. Langmuir **20**, 11308–11311 (2004)
181. T. Gong, Y. Zhang, W. Liu, J. Wei, Y. Jia, K. Wang, D. Wu, M. Zhong, Reinforcing the bandaged joint of double-walled carbon nanotube strands by intercalation of epoxy resin. Mater. Lett. **62**, 4431–4433 (2008)
182. H. Tohmyoh, S. Fukui, Self-completed Joule heat welding of ultrathin Pt wires. Phys. Rev. B **80**, 155403 (2009)

183. T.-B. Song, Y. Chen, C.-H. Chung, Y. Yang, B. Bob, H.-S. Duan, G. Li, K.-N. Tu, Y. Huang, Y. Yang, Nanoscale joule heating and electromigration enhanced ripening of silver nanowire contacts. ACS Nano **8**, 2804–2811 (2014)
184. A.T. Bellew, H.G. Manning, C. Gomes da Rocha, M.S. Ferreira, J.J. Boland, Resistance of single Ag nanowire junctions and their role in the conductivity of nanowire networks. ACS Nano **9**, 11422–11429 (2015)
185. A. Vafaei, A. Hu, I.A. Goldthorpe, Joining of individual silver nanowires via electrical current. Nano-Micro Lett. **6**, 293–300 (2014)
186. Y. Akada, H. Tatsumi, T. Yamaguchi, A. Hirose, T. Morita, E. Ide, Interfacial bonding mechanism using silver metallo-organic nanoparticles to bulk metals and observation of sintering behavior. Mater. Trans. **49**, 1537–1545 (2008)
187. H. Alarifi, A. Hu, M. Yavuz, Y.N. Zhou, Silver nanoparticle paste for low-temperature bonding of copper. J. Electron. Mater. **40**, 1394–1402 (2011)
188. J.S. Oh, J.S. Oh, J.H. Shin, G.Y. Yeom, K.N. Kim, Nano-welding of Ag nanowires using rapid thermal annealing for transparent conductive films. J. Nanosci. Nanotechnol. **15**, 8647–8651 (2015)
189. Ç.Ö. Girit, A. Zettl, Soldering to a single atomic layer. Appl. Phys. Lett. **91**, 193512 (2007)
190. Y. Peng, T. Cullis, B. Inkson, Bottom-up nanoconstruction by the welding of individual metallic nanoobjects using nanoscale solder. Nano Lett. **9**, 91–96 (2009)
191. Q. Cui, F. Gao, S. Mukherjee, Z. Gu, Joining and interconnect formation of nanowires and carbon nanotubes for nanoelectronics and nanosystems. Small **5**, 1246–1257 (2009)
192. Y. Ma, H. Li, L. Yang, A. Hu, Reaction-assisted diffusion bonding of $Ti_6A_{l4}V$ alloys with Ti/Ni nanostructured multilayers. J. Mater. Process. Technol. **262**, 204–209 (2018)
193. Mafune, J. Am. Chem. Soc. **125**, 1636 (2003)
194. C. Ma, S. Xue, D. Bridges, Z. Palmer, Z. Feng, A. Hu, Low temperature brazing nickel with Ag nanoparticle and Cu-Ag core-shell nanowire nanopastes. J. Alloys Compd. **721**, 431–439 (2017)
195. D. Bridges, R. Xu, A. Hu, Microstructure and mechanical properties of Ni nanoparticle-bonded Inconel 718. Mater. Des. **174**, 107784 (2019)
196. S. Dai, Q. Li, G. Liu, H. Yang, Y. Yang, D. Zhao, W. Wang, M. Qiu, Laser-induced single point nanowelding of silver nanowires. Appl. Phys. Lett. **108**, 121103 (2016)
197. L. Lin, G. Zou, L. Liu, W.W. Duley, Y.N. Zhou, Plasmonic engineering of metal-oxide nanowire heterojunctions in integrated nanowire rectification units. Appl. Phys. Lett. **108**, 203107 (2016)
198. Y. Deng, Y. Bai, Y. Yu, S. Deng, Y. Tian, G. Zhang, C. Zheng, J. Wu, A. Hu, Laser nanojoining of copper nanowires. J. Laser Appl. **31**, 022414 (2019)
199. M. Terrones, F. Banhart, N. Grobert, J.C. Charlier, H. Terrones, P.M. Ajayan, Molecular junctions by joining single-walled carbon nanotubes. Phys. Rev. Lett. **89**, 075505 (2002)
200. H. Shehla, A. Ishaq, Y. Khan, I. Javed, R. Saira, N. Shahzad, M. Maaza, Ion beam irradiation-induced nano-welding of Ag nanowires. Micro Nano Lett. **11**, 34–37 (2016)
201. C. Chen, L. Yan, E.S.-W. Kong, Y. Zhang, Ultrasonic nanowelding of carbon nanotubes to metal electrodes. Nanotechnology **17**, 2192–2197 (2006)
202. S. Hausner, S. Weis, B. Wielage, G. Wagner, Low temperature joining of copper by Ag nanopaste: correlation of mechanical properties and process parameters. Welding World **60**, 1277–1286 (2016)
203. G. Satoh, C. Qiu, S. Naveed, Y. Lawrence Yao, Strength and phase identification of autogenous laser brazed dissimilar metal microjoints. J. Manuf. Sci. Eng. **137** (2015)
204. S.J. Henley, M. Cann, I. Jurewicz, A. Dalton, D. Milne, Laser patterning of transparent conductive metal nanowire coatings: simulation and experiment. Nanoscale **6**, 946–952 (2014)
205. H. Yang, J. Lu, P. Ghosh, Z. Chen, W. Wang, H. Ye, Q. Yu, M. Qiu, Q. Li, Plasmonic-enhanced targeted nanohealing of metallic nanostructures. Appl. Phys. Lett. **112**, 071108 (2018)
206. Y. Li, Y. Li, L. Feng, G. Lu, Metal alloy nanowire joining induced by femtosecond laser heating: A hybrid atomistic-continuum interpretation. Int. J. Heat Mass Transfer **150**, 119287 (2020)

207. A.W. Ghosh, T. Rakshit, S. Datta, Gating of a molecular transistor: electrostatic and conformational. Nano Lett. **4**, 565–568 (2004)
208. C.H. Ahn, A. Bhattacharya, M. Di Ventra, J.N. Eckstein, C.D. Frisbie, M.E. Gershenson, A.M. Goldman, I.H. Inoue, J. Mannhart, A.J. Millis, A.F. Morpurgo, D. Natelson, J.-M. Triscone, Electrostatic modification of novel materials. Rev. Modern Phys. **78**, 1185–1212 (2006)
209. H. Song, Y. Kim, Y.H. Jang, H. Jeong, M.A. Reed, T. Lee, Observation of molecular orbital gating. Nature **462**, 1039–1043 (2009)
210. A. Aviram, M.A. Ratner, Molecular rectifiers. Chem. Phys. Lett. **29**, 277–283 (1974)
211. A.R.I. Aviram, P. Roland, The effect of electric fields on double-well-potential molecules. Ann. N.Y Acad. Sci. **852**, 339–348 (1998)
212. E.R. Brown, J.R. Söderström, C.D. Parker, L.J. Mahoney, K.M. Molvar, T.C. McGill, Oscillations up to 712 GHz in InAs/AlSb resonant-tunneling diodes. Appl. Phys. Letters **58**, 2291–2293 (1991)
213. J.C. Ellenbogen, J.C. Love, Architectures for molecular electronic computers. I. Logic structures and an adder designed from molecular electronic diodes. Proc. IEEE **88**, 386–426 (2000)
214. M. Jurow, A.E. Schuckman, J.D. Batteas, C.M. Drain, Porphyrins as molecular electronic components of functional devices. Coord. Chem. Rev. **254**, 2297–2310 (2010)
215. Z. Chen, B. Lee, S. Sarkar, S. Gowda, V. Misra, A molecular memory device formed by HfO_2 encapsulation of redox-active molecules. Appl. Phys. Lett. **91**, 173111 (2007)
216. M.J. Kumar, Molecular diodes and applications. Recent Patents Nanotechnol **1**, 51–57 (2007)
217. N.J. Tao, in *Nanoscience and Technology: A Collection of Reviews from Nature Journals* (World Scientific 2010), pp. 185–193
218. A. Hu, Q.B. Lu, W.W. Duley, M. Rybachuk, Spectroscopic characterization of carbon chains in nanostructured tetrahedral carbon films synthesized by femtosecond pulsed laser deposition. J. Chem. Phys. **126**, 154705 (2007)
219. S.J. Tans, M.H. Devoret, H. Dai, A. Thess, R.E. Smalley, L.J. Geerligs, C. Dekker, Individual single-wall carbon nanotubes as quantum wires. Nature **386**, 474–477 (1997)
220. P. Avouris, Molecular electronics with carbon nanotubes. Acc. Chem. Res. **35**, 1026–1034 (2002)
221. R. Martel, T. Schmidt, H.R. Shea, T. Hertel, P. Avouris, Single- and multi-wall carbon nanotube field-effect transistors. Appl. Phys. Lett. **73**, 2447–2449 (1998)
222. K. Sotthewes, V. Geskin, R. Heimbuch, A. Kumar, H.J.W. Zandvliet, Research update: molecular electronics: the single-molecule switch and transistor. APL Mater. **2**, 010701 (2014)
223. C. Joachim, J.K. Gimzewski, R.R. Schlittler, C. Chavy, Electronic transparence of a single C_{60} molecule. Phys. Rev. Lett. **74**, 2102–2105 (1995)
224. S. Heinze, J. Tersoff, R. Martel, V. Derycke, J. Appenzeller, P. Avouris, Carbon nanotubes as Schottky barrier transistors. Phys. Rev. Lett. **89**, 106801 (2002)
225. A. Javey, J. Guo, Q. Wang, M. Lundstrom, H. Dai, Ballistic carbon nanotube field-effect transistors. Nature **424**, 654–657 (2003)
226. M.M.J. Treacy, T.W. Ebbesen, J.M. Gibson, Exceptionally high Young's modulus observed for individual carbon nanotubes. Nature **381**, 678–680 (1996)
227. D. Dragoman, M. Dragoman, Terahertz oscillations in semiconducting carbon nanotube resonant-tunneling diodes. Physica E: Low-Dimens. Syst. Nanostruct. **24**, 282–289 (2004)
228. R.R. Pandey, N. Bruque, K. Alam, R.K. Lake. Carbon nanotube—molecular resonant tunneling diode. Phys. Status Solidi (a), **203**, R5–R7 (2006)
229. S. Venkataramani, U. Jana, M. Dommaschk, F.D. Sönnichsen, F. Tuczek, R. Herges, Magnetic bistability of molecules in homogeneous solution at room temperature. Science **331**, 445–448 (2011)
230. S. Di Motta, E. Di Donato, F. Negri, G. Orlandi, D. Fazzi, C. Castiglioni, Resistive molecular memories: influence of molecular parameters on the electrical bistability. J. Am. Chem. Soc. **131**, 6591–6598 (2009)
231. Y. Li, H. Li, Y. Li, H. Liu, S. Wang, X. He, N. Wang, D. Zhu, Energy transfer switching in a bistable molecular machine. Org. Lett. **7**, 4835–4838 (2005)

232. M.S. Madani, M. Monajjemi, H. Aghaei, M. Giahi, Thin double wall boron nitride nanotube: nano-cylindrical capacitor. Orient. J. Chem. **33**, 1213–1222 (2017)
233. J.E. Green, J. Wook Choi, A. Boukai, Y. Bunimovich, E. Johnston-Halperin, E. DeIonno, Y. Luo, B.A. Sheriff, K. Xu, Y. Shik Shin, H.-R. Tseng, J.F. Stoddart, J.R. Heath, A 160-kilobit molecular electronic memory patterned at 1011 bits per square centimetre. Nature **445**, 414–417 (2007)
234. J.R. Pinzon, A. Villalta-Cerdas, L. Echegoyen, in *Unimolecular and Supramolecular Electronics I* (Springer 2011), pp. 127–174
235. G. Wang, Y. Kim, M. Choe, T.-W. Kim, T. Lee, A new approach for molecular electronic junctions with a multilayer graphene electrode. Adv. Mater. **23**, 755–760 (2011)
236. J. Liu, Z. Yin, X. Cao, F. Zhao, A. Lin, L. Xie, Q. Fan, F. Boey, H. Zhang, W. Huang, Bulk heterojunction polymer memory devices with reduced graphene oxide as electrodes. ACS Nano **4**, 3987–3992 (2010)
237. X. Wang, L. Zhi, K. Müllen, Transparent, conductive graphene electrodes for dye-sensitized solar cells. Nano Lett. **8**, 323–327 (2008)
238. M. Freitag, M. Radosavljevic, Y. Zhou, A.T. Johnson, W.F. Smith, Controlled creation of a carbon nanotube diode by a scanned gate. Appl. Phys. Lett. **79**, 3326–3328 (2001)
239. M.A. Hughes, K.P. Homewood, R.J. Curry, Y. Ohno, T. Mizutani, An ultra-low leakage current single carbon nanotube diode with split-gate and asymmetric contact geometry. Appl. Phys. Lett. **103**, 133508 (2013)
240. T. Tsuji, T. Kakita, M. Tsuji, Preparation of nano-size particles of silver with femtosecond laser ablation in water. Appl. Surf. Sci. **206**, 314–320 (2003)
241. M. Hörstmann-Jungemann, J. Gottmann, D. Wortmann, Nano-and microstructuring of SiO_2 and sapphire with fs-laser induced selective etching. J. Laser Micro/Nanoeng. **4**, 135–140 (2009)
242. A. Maurice, L. Bodelot, B.K. Tay, B. Lebental, Controlled, low-temperature nanogap propagation in graphene using femtosecond laser patterning. Small **14**, 1801348 (2018)
243. F. Prins, A. Barreiro, J.W. Ruitenberg, J.S. Seldenthuis, N. Aliaga-Alcalde, L.M.K. Vandersypen, H.S.J. van der Zant, Room-temperature gating of molecular junctions using few-layer graphene nanogap electrodes. Nano Lett. **11**, 4607–4611 (2011)
244. Q. Xu, G. Scuri, C. Mathewson, P. Kim, C. Nuckolls, D. Bouilly, Single electron transistor with single aromatic ring molecule covalently connected to graphene nanogaps. Nano Lett. **17**, 5335–5341 (2017)
245. H.W.C. Postma, Rapid sequencing of individual DNA molecules in graphene nanogaps. Nano Lett. **10**, 420–425 (2010)
246. J. Prasongkit, A. Grigoriev, B. Pathak, R. Ahuja, R.H. Scheicher, Transverse conductance of DNA nucleotides in a graphene nanogap from first principles. Nano Lett. **11**, 1941–1945 (2011)
247. W. Kubo, S. Fujikawa, Au double nanopillars with nanogap for plasmonic sensor. Nano Lett. **11**, 8–15 (2011)
248. E. Braun*, K. Keren, From DNA to transistors. Adv. Phys. **53**, 441–496 (2004)
249. E. Braun, Y. Eichen, U. Sivan, G. Ben-Yoseph, DNA-templated assembly and electrode attachment of a conducting silver wire. Nature **391**, 775–778 (1998)
250. J. Richter, M. Mertig, W. Pompe, I. Mönch, H.K. Schackert, Construction of highly conductive nanowires on a DNA template. Appl. Phys. Lett. **78**, 536–538 (2001)
251. R. Seidel, M. Mertig, W. Pompe, Scanning force microscopy of DNA metallization. Surface Interface Anal. **33**, 151–154 (2002)
252. K. Keren, R.S. Berman, E. Braun, Patterned DNA metallization by sequence-specific localization of a reducing agent. Nano Lett. **4**, 323–326 (2004)
253. K. Keren, M. Krueger, R. Gilad, G. Ben-Yoseph, U. Sivan, E. Braun, Sequence-specific molecular lithography on single DNA molecules. Science **297**, 72–75 (2002)
254. K. Keren, R.S. Berman, E. Buchstab, U. Sivan, E. Braun, DNA-templated carbon nanotube field-effect transistor. Science **302**, 1380–1382 (2003)

255. Y. Ye, L. Chen, X. Liu, U.J. Krull, DNA and microfluidics: building molecular electronics systems. Anal. Chim. Acta **568**, 138–145 (2006)
256. L. Li, M. Hong, M. Schmidt, M. Zhong, A. Malshe, B. Huis in't Veld, V. Kovalenko, Laser nano-manufacturing—State of the art and challenges. CIRP Ann. **60** 735–755 (2011)
257. C. Barner-Kowollik, M. Bastmeyer, E. Blasco, G. Delaittre, P. Müller, B. Richter, M. Wegener, 3D laser micro- and nanoprinting: challenges for chemistry. Angewandte Chemie Int. Edn. **56**, 15828–15845 (2017)
258. T. Gissibl, S. Thiele, A. Herkommer, H. Giessen, Two-photon direct laser writing of ultracompact multi-lens objectives. Nat. Photon. **10**, 554–560 (2016)
259. C. Liao, W. Anderson, F. Antaw, M. Trau, Two-photon nanolithography of tailored hollow three-dimensional microdevices for biosystems. ACS Omega **4**, 1401–1409 (2019)
260. K.S. Worthington, A.-V. Do, R. Smith, B.A. Tucker, A.K. Salem, Two-photon polymerization as a tool for studying 3D printed topography-induced stem cell fate. Macromol. Biosci. **19**, 1800370 (2019)
261. Z.B. Wang, N. Joseph, L. Li, B.S. Luk'Yanchuk, A review of optical near-fields in particle/tip-assisted laser nanofabrication. Proc. Inst. Mech. Eng. Part C: J. Mech. Eng. Sci. **224**, 1113–1127 (2010)
262. W. Guo, Z.B. Wang, L. Li, D.J. Whitehead, B.S. Luk'yanchuk, Z. Liu, Near-field laser parallel nanofabrication of arbitrary-shaped patterns. Appl. Phys. Lett. **90**, 243101 (2007)
263. S.M. Huang, M.H. Hong, B.S. Luk'yanchuk, Y.W. Zheng, W.D. Song, Y.F. Lu, T.C. Chong, Pulsed laser-assisted surface structuring with optical near-field enhanced effects. J. Appl. Phys. **92**, 2495–2500 (2002)
264. J.W. Kingsley, S.K. Ray, A.M. Adawi, G.J. Leggett, D.G. Lidzey, Optical nanolithography using a scanning near-field probe with an integrated light source. Appl. Phys. Lett. **93**, 213103 (2008)
265. W. Srituravanich, N. Fang, C. Sun, Q. Luo, X. Zhang, Plasmonic nanolithography. Nano Lett. **4**, 1085–1088 (2004)
266. W. Srituravanich, S. Durant, H. Lee, C. Sun, X. Zhang, Deep subwavelength nanolithography using localized surface plasmon modes on planar silver mask. J. Vacuum Sci. Technol. B: Microelectron. Nanometer Struct. Process. Measure. Phenomena **23**, 2636–2639 (2005)
267. Z.-W. Liu, Q.-H. Wei, X. Zhang, Surface plasmon interference nanolithography. Nano Lett. **5**, 957–961 (2005)
268. J. Dong, J. Liu, G. Kang, J. Xie, Y. Wang, Pushing the resolution of photolithography down to 15 nm by surface plasmon interference. Sci. Rep. **4**, 5618 (2014)
269. S.W. Hell, J. Wichmann, Breaking the diffraction resolution limit by stimulated emission: stimulated-emission-depletion fluorescence microscopy. Opt. Lett. **19**, 780–782 (1994)
270. E. Rittweger, K.Y. Han, S.E. Irvine, C. Eggeling, S.W. Hell, STED microscopy reveals crystal colour centres with nanometric resolution. Nature Photon. **3**, 144–147 (2009)
271. B. Harke, P. Bianchini, F. Brandi, A. Diaspro, Photopolymerization inhibition dynamics for sub-diffraction direct laser writing lithography. Chem. Phys. Chem. **13**, 1429–1434 (2012)
272. B. Harke, J. Keller, C.K. Ullal, V. Westphal, A. Schönle, S.W. Hell, Resolution scaling in STED microscopy. Opt. Express **16**, 4154–4162 (2008)
273. R. Wollhofen, J. Katzmann, C. Hrelescu, J. Jacak, T.A. Klar, 120 nm resolution and 55 nm structure size in STED-lithography. Opt. Express **21**, 10831–10840 (2013)
274. A.G. Vitukhnovsky, D.A. Chubich, S.P. Eliseev, V.V. Sychev, D.A. Kolymagin, A.S. Selyukov, Advantages of STED-inspired 3D direct laser writing for fabrication of hybrid nanostructures. J. Russian Laser Res. **38**, 375–382 (2017)
275. M. Wiesbauer, R. Wollhofen, B. Vasic, K. Schilcher, J. Jacak, T.A. Klar, Nano-anchors with single protein capacity produced with STED lithography. Nano Lett. **13**, 5672–5678 (2013)
276. X. He, T. Li, J. Zhang, Z. Wang, STED direct laser writing of 45 nm width nanowire. Micromachines **10**, 726 (2019)
277. Z. Gan, Y. Cao, R.A. Evans, M. Gu, Three-dimensional deep sub-diffraction optical beam lithography with 9 nm feature size. Nat. Commun. **4**, 2061 (2013)